

© Copyright by Wenli Yang 2019

All Rights Reserved

LOW TEMPERATURE SYNTHESIS OF SAPPHIRE OR RUBY AND THEIR APPLICATIONS

A Dissertation

Presented to

The faculty of the Materials Science and Engineering Program

University of Houston

In Partial Fulfillment

of the Requirements for the Degree

Doctor of Philosophy

in Material Engineering

by

Wenli Yang

May 2019

LOW TEMPERATURE SYNTHESIS OF SAPPHIRE OR RUBY AND THEIR APPLICATIONS

Wenli Yang

Approved:

Chairman of the Committee

Dr. Stanko R. Brankovic, Professor

Electrical and Computer Engineering

Dr. Francisco C. Robles, Associate Professor

Mechanical Engineering Technology

Committee Members:

Dr. Yan Yao, Associate Professor

Electrical and Computer Engineering

Dr. Jiming Bao, Associate Professor

Electrical and Computer Engineering

Dr. Debora Rodrigues, Associate Professor

Civil and Environmental Engineering

Dr. Suresh Khator, Associate Dean,
Cullen College of Engineering

Dr. Alamgir Karim, Program Director
Materials Science and Engineering Program

ACKNOWLEDGEMENT

I would like to take this opportunity to express my sincere gratitude to my advisors, Dr. Stanko R. Brankovic and Dr. Francisco C. Robles, for their kindness, motivation and immense knowledge. Their guidance helped me in this project and writing of this thesis. Through this training process, I become more professional in my career.

Besides my advisors, I would also like to thank my committee members Dr. Debora Rodrigues, Dr. Yan Yao, and Dr. Jiming Bao for their serving on my committee and encouragements, but also for hard questions which direct me to widen my research in various perspectives. There are some other professors in the University, Dr. Viktor G Hadjiev for helping me to analyzing the Raman spectrum to improve my knowledge in this area. I would like to thank Dr. Karoline Müller for training me on XRD instruments and teaching me how to calculate the grain size accurately. I would like to thank Dr. Chrisdelyn Dawson for supporting me about the graduation documents.

I would like to acknowledge College of Technology for funding me as a Teaching Assistant in the material technology lab, I had an experience of giving lectures and improved my communication skills. I am also thankful for Lam Research to support me financially to finish this project. Without their financial support it would not be possible to conduct this project.

In addition, I thank my fellow labmates Dongjun Wu, Kamyar Ahmadi, Dhaivat Solanki, Nikhil Chaudhari, Mehrnaz Shirazi, Miad Yarali and ÖmerFaruk Karadavut for helping me in the experiments and fixing some problems in this project. In particular, I am grateful to Kamyar for stimulating discussions, and for the time we were working together.

Last but not least, I would like to thank my family: my parents, my mentor, my brothers and sisters for supporting me spiritually throughout this Ph.D. degree pursuing and my life in general.

LOW TEMPERATURE SYNTHESIS OF SAPPHIRE OR RUBY AND THEIR APPLICATIONS

An abstract

of

A Dissertation

Presented to

The faculty of the Materials Science and Engineering Program

University of Houston

In Partial Fulfillment

of the Requirements for the Degree

Doctor of Philosophy

in Material Engineering

by

Wenli Yang

May 2019

ABSTRACT

Sapphire or ruby as a single crystal α - Al_2O_3 phase is gaining a lot of attention in recent years due to its thermal, mechanical and optical properties. The current study presents a unique method to synthesize sapphire or ruby, which optimize the traditional synthesis process, and explores some of their applications such as high refractive index thin film coating and stress transferring material. In the synthesis process, pseudoboehmite (PB) is used as a precursor and mechanical milling is employed to reduce the phase transformation temperature of pseudoboehmite to sapphire or ruby. The phase transformation of the milled PB samples was investigated by various characterization techniques. XRD data showed that PB structure is first synthesized as raw material, followed by its room temperature transformation to χ - Al_2O_3 . Raman spectrum and HRTEM confirmed the presence of α - Al_2O_3 and χ - Al_2O_3 phase in the 30hr milled PB sample. Through the proposed synthesis method, there is a significant temperature reduction (approximately 200°C) for the complete transformation to sapphire or ruby during annealing, which is confirmed from thermal analysis. This is due to sapphire or ruby seeds are synthesized at room temperature in the milled sample and serve as hetero sites for nucleation in the annealing process.

In addition, XPS and EELS analysis shows unique band gap effects, both of them are consistent with theoretical value for two random choosing samples (PB milled 10hr and 30hr samples). This indicates the reliability of XPS band gap results. It is found it is possible to tune the band gap of alumina during mechanical milling through quantum confinement. FTIR result shows that PB lose water content from its structure, which can releases its surface strain during the milling process, therefore cold welding induces the increase of PB grain size. The current study also involved the application of sapphire or ruby thin films, which are deposited on

substrates through ion beam sputtering from the low temperature synthesized sapphire or ruby target.

TABLE OF CONTENTS

ACKNOWLEDGEMENT	v
ABSTRACT.....	viii
TABLE OF CONTENTS.....	x
LIST OF FIGURES	xv
LIST OF TABLES.....	xviii
CHAPTER 1	1
INTRODUCTION	1
1.1 Signification of the Alumina	1
1.2 Alumina: Different Phases, Phase Transformation and Application.....	2
1.2.1 Gamma-alumina (γ -Al ₂ O ₃): Structure, Phase Transformation and Application	4
1.2.2 Theta-alumina (θ -Al ₂ O ₃): Structure, Phase Transformation and Application	6
1.2.3 Alpha-alumina (α -Al ₂ O ₃): Structure, Phase Transformation and Application.....	7
1.4 This Ph.D. Work.....	10
1.5 Outline of This Ph.D. Report.....	11
CHAPTER 2	13
EXPERIMENTAL TECHNIQUES.....	13
2.1 Mechanical Milling	13
2.1.1 Phase Transformation in the Mechanical Milling Process.....	13
2.1.2 Grain Size Change in the Mechanical Milling Process.....	15

2.1.2.1 Cold Welding.....	16
2.1.2.2 Quantum Confinement.....	17
2.1.3 Mechanical Milling Applications.....	19
2.2 Material Characterization Methods.....	19
2.2.1 X-ray Powder Diffraction (XRD).....	19
2.2.1.1 Grain Size Measured by XRD.....	20
2.2.2 Raman Spectroscopy.....	21
2.2.3 Differential Scanning Calorimetry (DSC).....	23
2.2.3.1 Typical DSC Graph.....	24
2.2.4 X-ray Photoelectron Spectroscopy (XPS).....	25
2.2.4.1 XPS Spectrum.....	26
2.2.4.2 Band Gap Measured by XPS.....	27
2.2.5 Electron Energy-Loss Spectroscopy (EELS).....	28
2.3 Deposition Techniques of Thin Films.....	30
2.3.1 Ion Beam Sputtering.....	32
2.3.1.1 Mechanism of the Ion Beam Sputtering.....	32
2.3.1.2 The Application of Ion Beam Sputtered Thin Films.....	34
2.4 Sapphire or Ruby Thin Film Application I – Modifying the Refractive Index of Substrate.....	34
2.4.1 Refractive Index.....	34

2.4.2 Methods for Determining the Refractive Index of Thin Films	37
2.5 Sapphire or Ruby Thin Film Application II – Measuring the Residual Stress of Superconductor YBCO Thin Film.....	41
2.5.1 Residual Stress in YBCO Thin Film.....	41
2.5.2 Residual Stress Measured by Raman Spectrum.....	42
CHAPTER 3	43
EXPERIMENTAL SET-UP AND TECHNOLOGY	43
3.1 Synthesis Process.....	44
3.2 Mechanical Milling	45
3.3 Characterization Methods.....	46
3.3.1 Thermal Analysis	46
3.3.2 X-ray photoelectron spectroscopy (XPS).....	47
3.3.3 X-Ray Diffraction (XRD)	47
3.3.4 Fourier Transform Infrared Spectroscopy (FTIR)	48
3.3.5 Raman Spectroscopy.....	49
3.3.5 High resolution transmission electron microscopy (HRTEM)	49
3.4 Preparation of Sapphire or Ruby Pellet as the Target for Ion Beam Sputtering	49
3.5 Ion Beam Sputtering Process.....	50
3.7 The Ellipsometry Measurement for the Refractive Index of the Ruby Thin Film	52
3.8 The Stress Measurement for the Superconductor YBCO Thin Film	53

CHAPTER 4	54
RESULTS AND DISCUSSION.....	54
4.1 Mechanical Milling	54
4.1.1 Phase Transformation.....	54
4.1.1.1 PB Phase Disappearance and α -Al ₂ O ₃ Phase Appearance	54
4.1.1.2 Mechanism of the Phase Transformation	57
4.1.1.3 Novelty of Mechanical Milling on the Phase Transformation	59
4.1.2 Grain Size Change.....	60
4.1.3 Band Gap Change	63
4.1.3.1 Quantum Confinement.....	65
4.1.4 Mechanical Milling Application	68
4.1.4.1 Preparing Sapphire Phase	68
4.1.4.2 Preparing Ruby Phase	68
4.2 Thin Film Deposition	70
4.2.1 Preparation of Sapphire and Ruby Target Pellet.....	70
4.2.2 Ion Beam Sputtering	71
4.3 Prepared Thin Films Application	75
4.3.1 The Sapphire Thin Film Application- High Refractive Index	75
4.3.2 The Ruby Thin Film Application-Pressure Sensing	76
CHAPTER 5	78

SUMMARY AND CONCLUSIONS	78
CHAPTER 6	81
FUTURE WORK.....	81
REFERENCES	83

LIST OF FIGURES

Figure 1 Schematics of the main solid states transformations of alumina [14, 17]	3
Figure 2 Boehmite crystal structure [20]	4
Figure 3 γ -alumina crystal structure [25]	5
Figure 4 θ -alumina crystal structure [33]	6
Figure 5 α -alumina crystal structure [42]	7
Figure 6 Gibbs free energy change of the phase during milling process	14
Figure 7 (a) mechanical milling process (b) mechanism of cold welding	16
Figure 8 Electron states of (a) bulk materials and (b) nano materials (c) band gap of bulk and nano materials	18
Figure 9 XRD scheme	20
Figure 10 Bragg law scheme	21
Figure 11 Light scattering by molecular	22
Figure 12 DSC scheme	24
Figure 13 DSC data graph	25
Figure 14 Electron excitement in XPS (a) and photoemission of O1s (b)	26
Figure 15 XPS spectra for the O 1s peak in Al_2O_3	27
Figure 16 Energy bands in metals, semiconductors, and insulators	28
Figure 17 Configuration of EELS	29
Figure 18 EELS spectrum	30
Figure 19 Ion beam sputtering process	32
Figure 20 Schematic diagram of gridded ion source	33
Figure 21 Snell's law	35
Figure 22 Refraction of a light through a prism	37

Figure 23 The angle of deviation changing with the incident angle.....	38
Figure 24 Brewster's angle	39
Figure 25 The principle of the ellipsometry [90].....	40
Figure 26 The synthesis procedure	43
Figure 27 Synthesis process from PB to sapphire or ruby.....	44
Figure 28 PB powder synthesis and drying	45
Figure 29 Spex milling machine.....	46
Figure 30 DSC	47
Figure 31 The characterization instruments (a) XRD (b) FTIR (c) Raman (d) XPS.....	48
Figure 32 Instruments for producing target (a) the French press (b) the cell (c) the furnace..	50
Figure 33 (a) Synthesized pseudoboehmite (b) sapphire pellet (c) ruby pellet	50
Figure 34 Ion beam milling instrument	51
Figure 35 Gaertner Ellipsometer.....	52
Figure 36 (a) Ni tape surface looking before ion beam sputtering ruby (b) Ni tape surface looking after ion beam sputtering ruby (c) structure of the Ni tape.....	53
Figure 37 Diffraction patterns of the raw and milled PB. PB and χ -Al ₂ O ₃ stand for pseudoboehmite and chi-alumina respectively.	55
Figure38 Raman spectra of raw and milled PB with an excitation line of 785 nm.	56
Figure 39 (a, b) HRTEM images and interplanar measurements for the PB 20hr and 30hr samples.....	56
Figure 40 FTIR spectrum of pure pseudoboehmite with different milling time (a) OH stretching vibrations; (b) Al-O-H bending vibration; (c) the lack of bending vibration of the hydroxyl bands	58
Figure 41 (a) PB crystalline structure and (b) mechanism of phase transformation	59

Figure 42 DSC analysis of raw and milled 30hr PB.....	60
Figure 43 (a) XRD of PB at different milling time (b) variations in grain size of PB with increasing milling time (0-50hr).....	61
Figure 44 SEM microstructures of the raw and milled samples for up to 50h.....	62
Figure 45 (a) High resolution scans of the O 1s peak the PB 0hr. (b) Band gap trend with the milling times	63
Figure 46 (a) EELS data of PB 10hr (b) EELS data of PB 30hr	64
Figure 47 (a) Variation in grain size and the corresponding band gap with respect to different milling time. (b) The relationship between the band gap and $1/D^2$	65
Figure 48 (a) XRD data for the samples milled 0-10hr (b) Grain size trend with the milling time	66
Figure 49 The relationship between the band gap and $1/D^2$	67
Figure 50 Raman spectra of raw and milled PBCr with an excitation line of 532 nm.	69
Figure 51 HRTEM images and interplanar measurements for α -Cr:Al ₂ O ₃ showing the presence of ruby phase.....	69
Figure 52 Diffraction patterns of the target pellet: (a) the sapphire (b) the ruby.....	71
Figure 53 Original chamber: (a) photo of the chamber (b) configure of the chamber (c) sputtering ruby on Au/Mica substrate (d) sputtering ruby on Silicon wafer	72
Figure 54 Designed new chamber: (a) photo of the chamber (b) configure of the chamber (c) XRD of raw and 30min sputtered Au/Mica sample (d) Raman spectra of raw and 30min sample.	74
Figure 55 XRD of the 150nm sapphire thin film.....	75
Figure 56 (a) XRD of raw Ni tape and Ni tape after 120min sputtering (b) Raman spectra of ruby thin film before and after sputtering the YBCO	77

LIST OF TABLES

Table 1 Chemicals for the experiment	45
Table 2 Ellipsometry results	76

CHAPTER 1

INTRODUCTION

1.1 Signification of the Alumina

Aluminum with its oxides, hydroxides and alumina silicates ubiquitously is the most abundant metallic element in the earth's crust [1]. There exists a large diversity of aluminum oxides phases. Alumina (Al_2O_3) is the dominating form of the aluminum oxide. It is reported that Al_2O and AlO phases exist at the interface between the surface oxide films and the metal bulk part [2]. Bayer process provides the most economic ways to obtain high purity alumina [3]. During Bayer process, Bauxite ore deposits are mined and refined to alumina [4]. The bauxite reserves are about 55-75 billion tons, 33% in Africa, 24% in Oceania, 22% in South America and Caribbean, 15% in Asian, and 6% in other places [5]. It is known that over 90% of the bauxite ore was consumed to produce alumina, the remaining materials are applied as refractories, abrasives and chemicals [4]. The main process includes: 1) dissolve the aluminum bearing minerals by caustic liquor at high pressure and temperature; 2) remove the solid residue; 3) precipitate the pure alumina hydroxide [$\text{Al}(\text{OH})_3$] under cooling conditions; 4) calcine the alumina hydroxide to remove the water crystallization. But this process is an expensive and it is hard to produce consistent alumina particle size distribution, too fine or too coarse will cause dusting or disrupting the electrolytic smelting process [6]. On the other hand, there are so many risks in the Bayer process: physical, chemical, biological and ergonomic risk. In the bauxite mining process, noise is commonly encountered and can be very loud during the descaling of tanks. Noise-induced hearing loss cause a big issue. Bauxite contains trace quantities of mercury, which give rise of the mercury element vapor especially in the refining process of the

upstream part. Also bauxite mining and alumina refining increase the risks of tropical diseases such dengue fever and malaria caused by the water contamination. Ergonomic risks include stair climbing, sledgehammers, awkward postures, forceful and repetitive manual tasks [7]. Instead of the industrial Bayer process, people choose the chemical synthesis method to get alumina.

Alumina, as one of the most interesting ceramic materials, is widely employed as structural parts in medical field [8-10]. The advanced ceramics started to be used in the biomedical area around 1970s, and since then have been found that due to alumina's high hardness, wear resistance and excellent biocompatibility it is currently widely used in the medical field [11]. Meanwhile, alumina is an insulator with a high melting point around 2000°C, chemical resistance, high mechanic strength and low conductivity [12]. These characteristics make alumina attractive for tremendous application in the electronic area. It can be applied as a catalyst support, a protective barrier against corrosion. During past decades, there is a large number of papers studying the alumina's structures, properties and transition sequence [10].

1.2 Alumina: Different Phases, Phase Transformation and Application

Alumina exists in a variety of metastable structures including the α -alumina (hexagonal), β -alumina (hexagonal), γ -alumina (cubic spinel), δ -alumina (tetragonal), η -alumina (cubic spinel), θ -alumina (monoclinic), κ -alumina (orthorhombic) and χ -alumina (cubic) [13]. Compared with α -alumina's hexagonal crystal structure, other alumina phases are all based on cubic close packing array of oxide anions [14]. α -alumina is the only thermally stable phase, other phases belong to metastable phases [15]. Because the crystallographic d spacing is similar among these phases, it is hard to identify the alumina crystal structure during phase transformations. It means that most of these phases may coexist in the transformation

process [16]. For instance, η -, δ -, θ -, κ -, and χ -alumina are identified during the calcination of thermal decomposition of the oxy-hydroxide boehmite (γ -AlOOH) or gibbsite (γ -Al(OH)₃) to α -alumina (α -Al₂O₃). By thermal decomposition, the well crystallized boehmite passes through the following alumina polymorphic transformation to the thermodynamically stable phase, α -alumina polymorph (shown in Figure 1) [14]. The polymorphic alumina also can be produced through the calcination of any other alumina phases or hydroxide at a sufficient temperature [14].

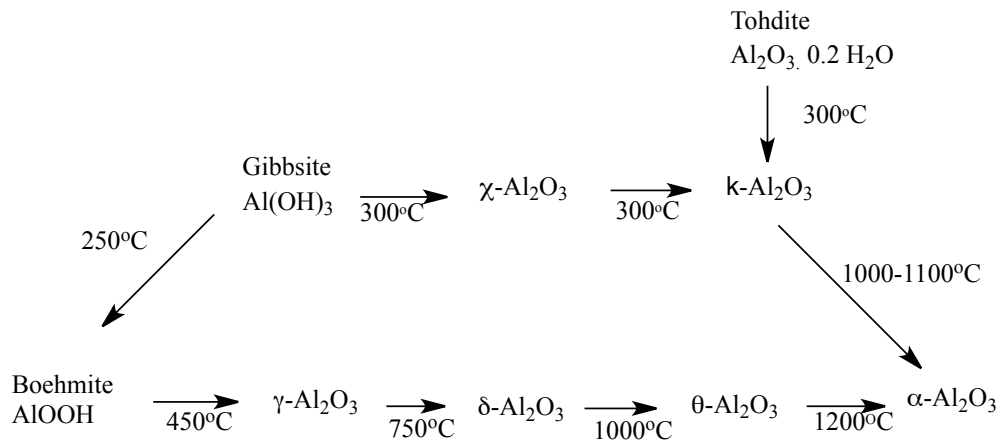


Figure 1 Schematics of the main solid states transformations of alumina [14, 17]

Boehmite (γ -AlOOH) (shown in Figure 2) and gibbsite (Al(OH)_3) are the most often used precursors for the transformation process [18]. They can be produced by controlling the temperature and pH in the aluminum hydroxide gel's aging process, which can form four different phases: pseudoboehmite (AlOOH)₂, gelatinous boehmite, poorly crystallized boehmite and well crystallized boehmite. Pseudoboehmite (AlOOH)₂, as a poorly crystallized boehmite has broader X-ray diffraction peaks which coincide with the major peak of well-crystallized boehmite. Pseudoboehmite is a transitional stage to produce boehmite and gibbsite. Pseudoboehmite has chains of boehmite structure (octahedral layers), those boehmite layers are

linked by hydrogen bonds. Therefore pseudoboehmite was considered to be an incomplete boehmite. Due to the presence of weaker hydrogen bond, it is rather a soft material when compared to alumina. Even though the boehmite consists of very small particles, its sintering process is very slow. During sintering, some of the methods for consolidation may need temperature up to 1600°C [19].

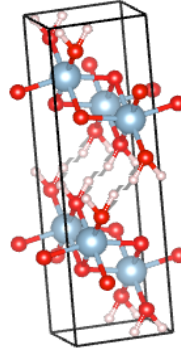


Figure 2 Boehmite crystal structure [20]

Gibbsite is also a widely accepted precursor for α -alumina through two transformation sequences. The first sequence is gibbsite transforming to κ -alumina, χ -alumina and then α -alumina. The second sequence involves the gibbsite transforming to boehmite, γ -alumina, θ -alumina and then α -alumina [21]. Every year gibbsite is produced in more than 30 billion tones in the world through the Bayer process. In industry most of the gibbsite is applied as an intermediate to produce aluminium. The rest of it is applied as filler for fireproof and paper, and precursors for the preparation of aluminium compound [22].

1.2.1 Gamma-alumina (γ -Al₂O₃): Structure, Phase Transformation and Application

Among the metastable alumina phases, γ -alumina (γ -Al₂O₃) is especially interesting as one of the most important and widely used catalyst support in the automotive and petroleum industries. The structure for the γ -Al₂O₃ is a defect spinel Al_{8/3}O₄, the unit cell contains 32

oxygen ions on the FCC positions with a ABCABC stacking sequence, 64/3 Al cations occupy the tetrahedral and octahedral positions (shown in Figure 3) [23]. γ -alumina is a metastable phase, and can transform to θ -alumina at 700–800°C. It cannot be used in the high temperature because this phase can transform to the stable phase (α -alumina) at high temperature [24].

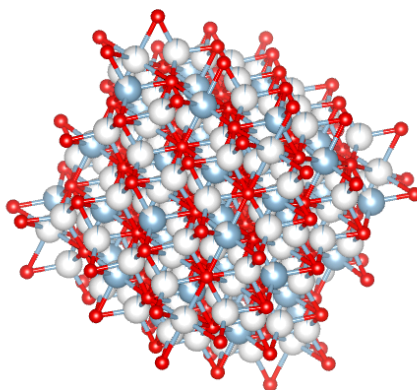


Figure 3 γ -alumina crystal structure [25]

Gamma-alumina is the product of decomposition of boehmite (γ -AlOOH) with the structure of a cubic defective (or non-stoichiometric) spinel under the temperature range of 500-550°C [26-28]. It does not exist in the pure single-crystal form and usually is porous with large surface areas [29]. The application of γ -alumina is contributed to a combination of its textural properties, such as pore size distribution, pore volume, surface area, and its acid/base characteristics, which are mainly related to local microstructure, phase composition and surface chemical composition. Among its properties the chemical and hydrothermal stability of γ -alumina still play a key role in deciding its applications in catalytic field [30]. Also it is applied at the ceramic interfaces or as a minor component in multiphase such as in the Al-Si-O systems [31]. However γ -alumina is an intermediate product in the transformation process, it transforms rapidly to more stable α -alumina phase at higher temperatures (1000-1100°C). The transformation of γ -alumina ($\rho = 3.56\text{g}\cdot\text{cm}^{-3}$) to α -alumina ($\rho = 3.98\text{g}\cdot\text{cm}^{-3}$) is accompanied by

a loss of porosity and it has a negative effect on the γ -alumina's application in catalytic area [28].

1.2.2 Theta-alumina (θ - Al_2O_3): Structure, Phase Transformation and Application

It is so important to mention the transformation process (from θ -alumina to α -alumina) to sinter and control the microstructure of α -alumina [28]. The transformation from θ -alumina (shown in Figure 4) to α -alumina forms around the temperature (1050-1200°C). Compared with the volume reduction in the transformation (γ -alumina to α -alumina), this transformation takes place through a nucleation and grain growth mechanism [28]. It has been approved by many reports, α -alumina nuclei occurs at certain sites in the θ -alumina crystalline matrix firstly [32]. Then it is followed by the growth of the nuclei to the surrounding matrix. There are a lot of reports extensively discussing the θ -alumina to α -alumina phase transformation and size change during the process [32].

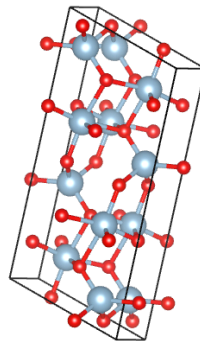


Figure 4 θ -alumina crystal structure [33]

Even though different alumina phases have been studied for many years, until now, there still exists a debate over the structures of some of the alumina phases. Therefore the application of these phases is limited by lacking adequate knowledge of the structures [28].

1.2.3 Alpha-alumina ($\alpha\text{-Al}_2\text{O}_3$): Structure, Phase Transformation and Application

Among all of the alumina phases, α -alumina ($\alpha\text{-Al}_2\text{O}_3$) is the most stable alumina with a hexagonal crystal system constructed of an aluminum atom, which is surrounded by six atoms of oxygen (shown in Figure 5). Meanwhile, the oxygen atoms are not bonded at the corners of a regular octahedron [34]. Because the electron between the aluminum and oxygen atoms are highly ionic, the bonds among them are so close. As a result, α -alumina ($\alpha\text{-Al}_2\text{O}_3$) is the second hardest naturally occurring material known by human kind [35]. Due to its thermal stability, high hardness and high resistance, α -alumina is widely used as refractory, ceramic, and chemical resistant materials [31]. The α -alumina's thin films have tremendous potential in microelectronic devices and optoelectronic devices [36-38]. It can be applied to many different fields, such as corrosion-resistant barriers, wear-resistant coatings and passivation layers [39]. As the aggressive scaling of the gate length and the gate oxide thickness demand a higher hardness of semiconductor material, α -alumina thin film, which is insulator with higher hardness, is widely used as wear-resistant coatings and a promising material to take place of standard SiO_2 semiconductor [40, 41].

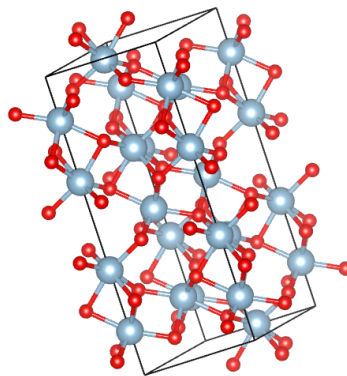


Figure 5 α -alumina crystal structure [42]

Sapphire, a single crystal structure of α -alumina, is an anisotropic material. The anisotropic atomic structure leads to anisotropic mechanical, physical and thermal properties. The melting point of sapphire is 2040°C, and it is known for its very high chemical stability even in high temperature. The dielectric strength is 480,000 V.cm⁻¹ [43]. White sapphire (α -Al₂O₃) is used for producing the scratch proof glasses for watches, while the blue sapphire (α -Al₂O₃ with a little Ti⁴⁺) is used in gemology field. In the latest trend sapphire is applied as substrate for high brightness Light Emitting Diode (LED) devices and an active luminescent medium. Also there is high demand for application in radio frequency devices, optical windows, tools for cutting edges and wear surface [44]. Lattice spacing is one of the most important characteristics of sapphire. The planes (0001), (10 $\bar{1}$ 0), (11 $\bar{2}$ 0) and (10 $\bar{1}$ 1) of sapphire are the most commonly used planes [45]. The sapphire's c-plane (0001) provides a good lattice match for growing GaN-based LED device layers in the metal-organic chemical vapor deposition process (MOCVD). Also sapphire is highly thermal stable, chemical resistant and mechanically strong, it meets the requirements for a good substrate that need to endure the high temperature and reactive atmosphere in MOCVD process. The high dielectric strength and lattice match between the silicon and γ -plane sapphire (1102) promote the silicon on sapphire technology development for high frequency radiofrequency switches. The sapphire's high optical transmission in the IR range combined with its high mechanical strength and temperature stability stimulate the sapphire in military and aerospace application [44]. For example sapphire optics can provide nearly 85% light transmission from the UV to IR range.

Ruby consists of sapphire (α -Al₂O₃) with a small percentage Al³⁺ ions replaced by Cr³⁺, and is the most widely used material among α -alumina based ceramics. Single crystal ruby can

be used as a working element of lasers, its laser intensity highly depends on the ruby's size and quantity of the optically active elements [46]. Meanwhile single crystal ruby is used for jewelry, tool product such as watch and bearing parts, and decoration parts because of its optical, thermal and mechanical properties. But ruby crystal has minimum light scattering when it is applied as solid-state laser, decoration part or jewelry. According to the light scattering model, the optical transmittance depends on the grain size, grain boundary and porosity [47]. In order to get highly transparent alumina, extremely low porosity (<0.05%) and small grain size (<1 μ m) should be satisfied. The Verneuil process use flame to sinter alumina and serves as a traditional way to synthesize gemstones like ruby and sapphire. Even though Verneuil method has made the artificial ruby production cheaper and easier, it is still expensive and difficult to produce the high quality crystals limiting its industrial application due to cost [48]. High technology links with the production of the high quality single crystal ruby, proposes to use the polycrystalline ruby for the laser [48, 49]. Polycrystalline alumina is a material hard to sinter and needs to be produced by reactors that require high temperature and vacuum or pressure assisted sintering process. In the past decades, the hot-pressing, hot-isostatic pressing, extrusion molding and cold isostatic pressing with high temperature (1800°C) vacuum sintering techniques have been applied to fabricate polycrystalline ruby [50].

The single crystal ruby can act as an optical high temperature thermometer and an ion-irradiation damage sensor. The ruby thin film has also been used as a probe to observe the local state density in complicated photonic systems. The α -alumina unique optical properties gained from its electronic structure and bonding between Al and O atoms make it widely applied as an optical component in thin-film devices [51]. The so called R lines of ruby are near red shifted weak bands in both the absorption and emission spectra. These bands are vibronic side band,

one-phonon transition. This makes ruby suitable for photon-spectroscopy application. The R1 and R2 line's intensity, wavelength and the fluorescence lifetime depends on temperature and pressure [52, 53]. So ruby is especially a good candidate for application as a sensor due to its resonant luminescence bands shift with temperature and pressure [54, 55]. In order to exploit the ruby's application in the photonics and electro-optic area, it is necessary to form high quality ruby thin film [56].

1.4 This Ph.D. Work

This Ph.D. thesis investigates a new cost effective way to produce transparent sapphire and red ruby thin films as well as exploring their optical applications. In order to get dense ruby products, it is necessary to design a perfect process from powder synthesis to sintering process. In the powder synthesis process, mechanical milling was chosen to help the phase transformation from pseudoboehmite to metastable alumina. Because pseudoboehmite's structure contains water molecule and is softer than the boehmite's, pseudoboehmite is an ideal precursor for milling. Here are presented the various material characterization methods (X-ray diffraction (XRD), Scanning electron microscope (SEM), high resolution transmission electron microscopy (HRTEM), a SETARAM differential scanning calorimeter (DSC), X-ray photoelectron spectroscopy (XPS), and a Thermo Scientific Nicolet iS50 FT-IR spectrometer, Raman Spectroscopy) were employed to observe and quantify the transformation behavior. The traditional spark plasma sintering (SPS) is the most popular sintering techniques, because it takes short time to fabricate bulk materials from powder [57]. However it is expensive and complex to operate it, since it requires a fast heating rate (up to $1000^{\circ}\text{C}\cdot\text{min}^{-1}$) and high pressure (up to 1GPa) [58]. A new sintering process for fabricating sapphire or ruby thin film was designed; the milled powders are pressed by the French press machine and heat at the

temperature (1000°C) for 3hr to get a white or pink α -alumina pellet, which can be applied as a target in ion beam sputtering. By ion beam sputtering, transparent sapphire or red ruby thin film is deposited on the substrate, and their applications as high refractive index coating and stress sensor were studied.

Aims of the project:

- To find and observe the phase transformation during the mechanical milling process.
- To observe mechanical milling effects on the phase change and particle size.
- To understand the phase transformation mechanism, in terms of the chemical bond changing and transforming energy changing.
- To verify whether the ion beam milling produces the sapphire and ruby thin film successfully, then explore sapphire and ruby thin film application by improving the refractive index of the material and measuring the stress of superconductor YBCO thin film.

1.5 Outline of This Ph.D. Report

This Ph.D. dissertation consists of six chapters. In the first chapter, introduction, alumina and its different phases (especially γ -alumina, θ -alumina and α -alumina) were briefly introduced. Also this chapter reviews literatures on phase transformation process from metastable alumina (γ -alumina, θ -alumina) to thermal stable α -alumina. Then the main thermal stable phase α -alumina (sapphire or ruby)'s structure, properties and its application were introduced.

The second chapter provides the background information of the experimental techniques such as mechanical milling, ion beam sputtering used in the experiment.

Additionally, it describes the theory behind the characterization methods, such as grain size calculation by XRD, band gap measurement by XPS and EELS, residual stress by Raman spectra etc.

The third chapter reveals experimental conditions and describes the set up in the system by explaining its components. In addition, it describes the sample experimental preparation and the whole procedure for getting sapphire or ruby thin film.

The fourth chapter divides into two parts to show the experiment results and analyses. The first part shows the effects of mechanical milling on the phase transformation, particle size, and band gap of the milled powder. The second part of the chapter shows the sapphire or ruby thin film's synthesis process and its application (optical application and stress measurement).

The fifth chapter gives a brief conclusion for the project.

The sixth and final chapter briefly summarizes future work and some recommendations for improvements in the synthesis process.

CHAPTER 2

EXPERIMENTAL TECHNIQUES

This chapter describes the experimental techniques applied in this work. It divides into four sections: section 2.1 talks about the mechanical milling, section 2.2 describes the material characterization methods and mechanisms, section 2.3 introduces the process for the thin film growth, and section 2.4 presents the methods used for the thin film optical property analysis.

2.1 Mechanical Milling

Mechanical milling (MM) is a solid state, high-energy ball-milling process to produce powders with controlled microstructure [59]. There are two different milling styles, direct and indirect, SPEX milling belongs to the indirect one. In the direct milling process, the material got the kinetic energy by mechanical shaft or rollers. In the indirect milling process, the milling system consists of a rotating vessel filled with steel balls and the sample. The vessel rotates with its longitudinal axis, which is fixed by the shafts. As the vessel swings back and forth, the steel balls and samples get the centrifugal force. When the centrifugal force exceeds the gravity force, the balls and samples spin to the vessel wall, which creates consecutive collisions with the chamber walls. During the collision, the impact energy is generated which will be discussed in the bellow paragraph [60].

2.1.1 Phase Transformation in the Mechanical Milling Process

Through this process, high intensity plastic deformations occur, which lead to various stresses in the grounded particles, such as compression, attritions, impact and shear. All of these can lead to the material's Gibbs free energy change. When the material gains enough energy to overcome the activation energy for phase change from A to B, the phase transformation will

occur (shown in Figure 6). The Gibbs free energy for the phase transformation is attained by transferred energy from power supply. There are a number of non-equilibrium phases, the powder's morphology change highly depends on the powder's mechanical properties - ductile or brittle.

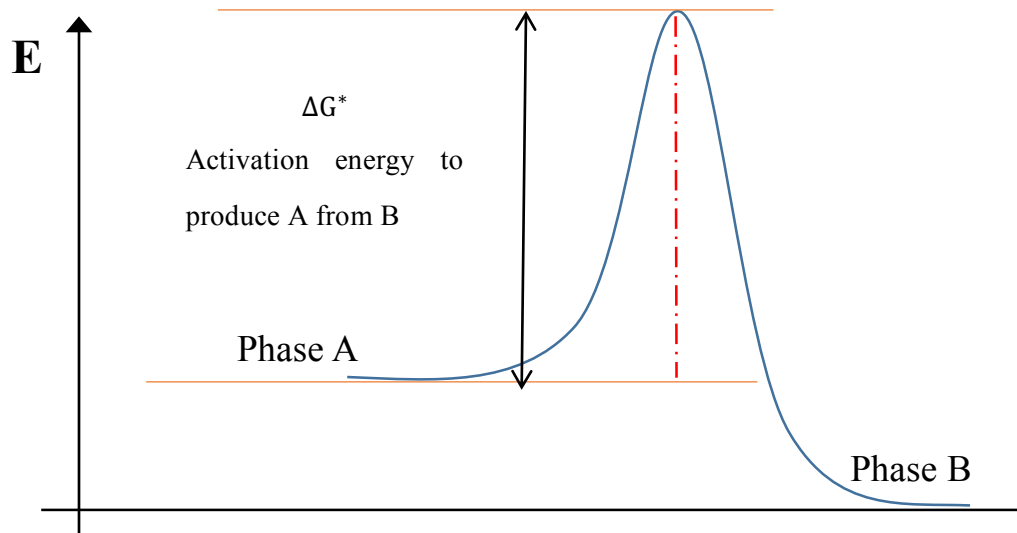


Figure 6 Gibbs free energy change of the phase during milling process

There are several theoretical models evaluating the power transferred to the vessel filling materials. The fundamental assumption is that mechanical energy is delivered through periodic and impulsive actions, not continuously supplied.

In the milling process, the power supplied (p) is transferred to the kinetic energy in a single collision (ΔE) and the total number of events per unit of time (N):

$$p = \varepsilon \cdot \Delta E \cdot N. \quad (1)$$

ε is an energy transfer coefficient, for perfect elastic collisions $\varepsilon = 0$; for perfect inelastic collisions $\varepsilon = 1$. ΔE is the kinetic energy involved in the collision. $\Delta E = \frac{1}{2} m_b v_b^2$. m_b and v_b

are the average mass and the velocity of the single impact event. Accordingly, specific energy (W_s) supplied to mill charge is given by

$$W_s = \frac{1}{M} \cdot \frac{dP}{dt} = \frac{\varepsilon \cdot m_b \cdot N \cdot v_b}{M} \quad (2)$$

Where M is the mass of the grounded materials.

2.1.2 Grain Size Change in the Mechanical Milling Process

During the ball milling process, the milling balls collide with each other and the particle powders are trapped in the colliding milling balls. The particles are continuously flattened, cold welded, fracture (shown in the Figure 7 (a)). In the Figure 7 (a), the blue line is the milling ball's boundary; the black line is the particle's boundary. In the ball's collision C process, some particles go through process A fracture, while some particles go through the process B cold welding. In the fracture process A, the colliding force deforms the powder particles that result in the crack (grey line), which can lead to reduction of particle size. Particles have new surface (green line) created in the collision process, in order to reduce the surface energy the particles is more likely to welding together (shown in process B), which leads to an increase of particle size.

Whether the cold welding or fracture plays a key role in the process is decided by the particles' hardness. If the powder particle is soft, they tend to weld together and form larger particles. But if the particle is harder, the fracture is predominant which leading to grain size decrease [61].

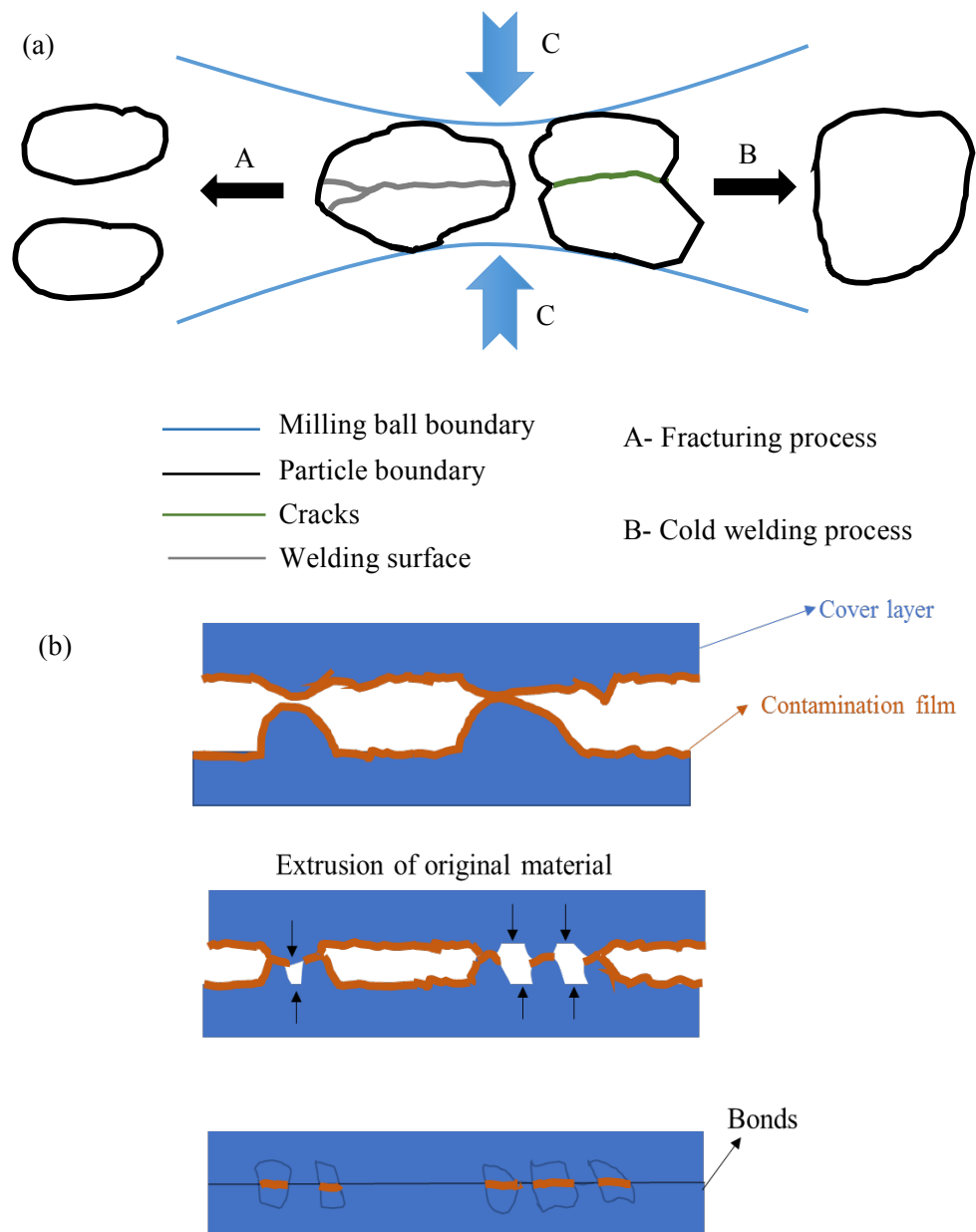


Figure 7 (a) mechanical milling process (b) mechanism of cold welding

2.1.2.1 Cold Welding

Welding is used for so many centuries, cold welding was firstly reported by Bartholomaeus Anglicus in the 12th century [62]. Cold welding is a solid state welding process in which pressure and plastic deformation of two materials make them jointed together in room

temperature without melting the materials [62, 63]. There are a number of theories trying to explain the bond formation in the cold welding. Among them, the film theory is the most acceptable one, which proposed that bond would form if two ultra clean surfaces are brought together and have an intimate contact [63, 64]. The mechanisms behind the cold welding are the cover layer of the material, which protects the original material surface from contamination, will fracture by plastic deformation. The virgin material exposed in the cracks and is increased because of surface expansion. Then virgin material will extrude through cracks of the cover layer and establish contact, bonding will formed between the virgin material surfaces [63]. Also previous investigation already observed this mechanism governing bonding [65] . This mechanism is schematically shown in Figure 7 (b).

The properties of material cover layers determine the weld formation [66]. Compared with hard material, it is easier to extrude virgin material layer through cracks in the cover layer in the soft material [66]. Therefore cold welding easily occurs in soft material.

2.1.2.2 Quantum Confinement

When the material is bulk material, the occupied and unoccupied electron states energy levels in the valence band and conductive band are overlaying to each other (shown in Figure 8 (a)). However if the material is nano material, the energy levels are separated (shown in Figure 8 (b)). Therefore the electron momentum of jumping from unoccupied states to the occupied states are confined. A band gap is the energy difference between the occupied electron states (valence band) and the unoccupied states (conduction band) (shown in the Figure 8 (c)). It is one of most important parameter to effect the material's optical properties. It represents the minimum required energy to excite an electron from the valence band to the conductive band.

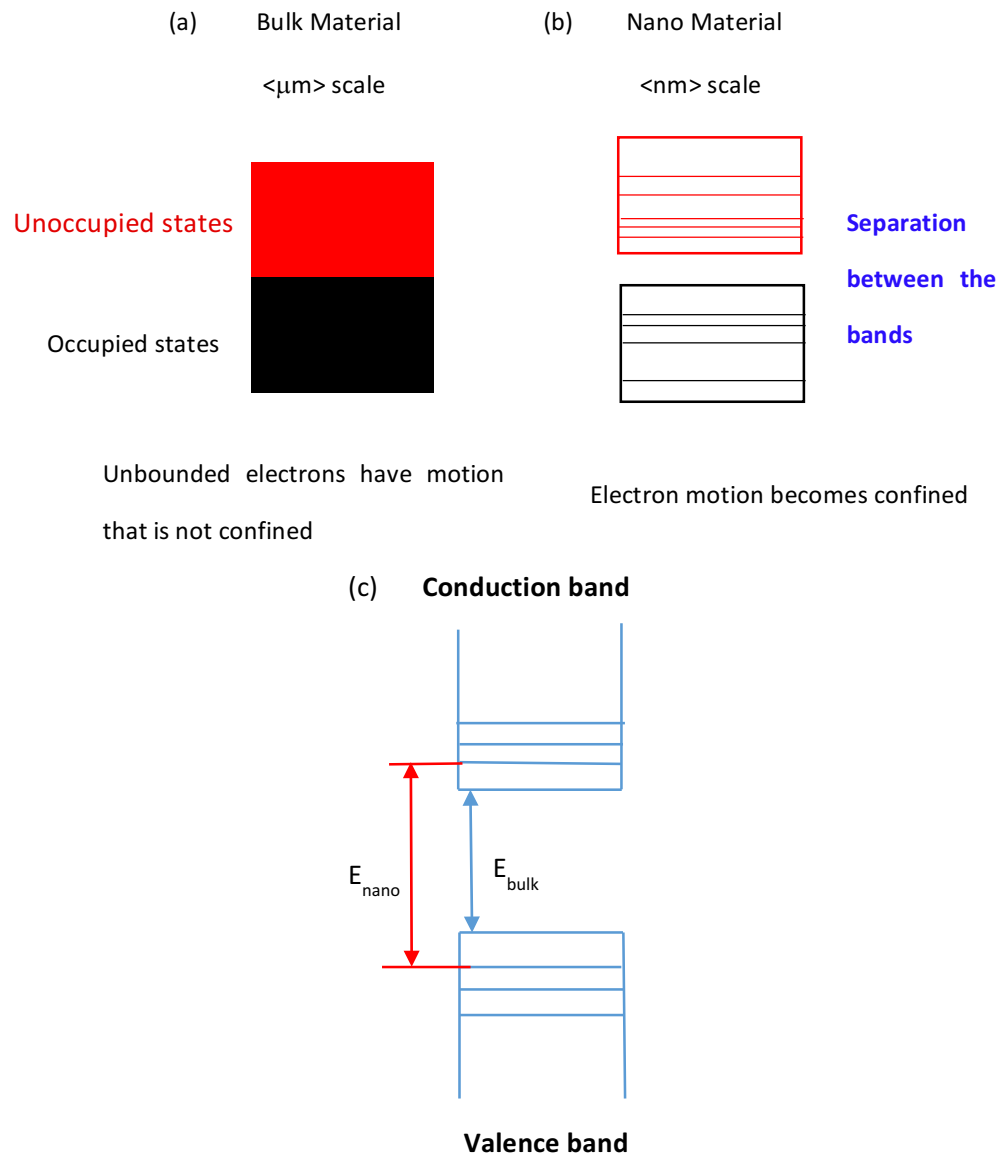


Figure 8 Electron states of (a) bulk materials and (b) nano materials (c) band gap of bulk and nano materials

Compared bulk and nano materials, the confined band gap have linear relationship with the reverse of size square, which is called quantum confinement, it can be expressed as

$$E = \frac{n^2 h^2}{8mL^2} \quad (3)$$

L is the particle diameter, h refers to Plank constant, n is quantum level and m is mass of the electron.

2.1.3 Mechanical Milling Applications

The mechanical milling process has been a major component in the ceramic processing and metallurgy industries [67]. The objective of mechanical milling is to reduce the particle size, mix the particle, generate intimated contact within constituents and change the particle shape. Mechanical alloying has been carried out in milling equipment capable of higher energy compressive impact forces such as attrition mills, ball mills, vibrating ball mills, SPEX and shaker mills [67].

Mechanical milling has been widely used to produce non-equilibrium phases including nano crystalline metallic, ceramic materials, and amorphous alloys. An importance of mechanical milling is that it can trigger phase transformations in the solid state at much lower temperatures than normal and even at room temperature. For example, mechanical milling of TiO₂ has been shown to result in the transformation of the anatase phase to the rutile phase [68]. It has been shown that materials processed mechanical milling have improved physical and mechanical characteristics, compared with conventional solidification processed materials [61].

2.2 Material Characterization Methods

2.2.1 X-ray Powder Diffraction (XRD)

X-ray powder diffraction (XRD) is a nondestructive analytical technique used for identification of crystal structures, phase and atomic space. In the XRD instrument, there are three basic components: X-ray tube, sample holder and X-ray detector. The X-ray tube can produce X-rays, the filament in the tube is heated to produce electrons, and the electrons are accelerating toward the target by applying the voltage. When the electrons bombard the target

material, the electrons with sufficient energy can dislodge inner shell electrons of the target, thus characteristic X-rays are generated. These X-rays consist of more than one spectrum, the most common X-ray spectra are K_{α} and K_{β} (different from the wavelength). The wavelength is depending on the target material, which produces X-rays spectra. Copper is a widely used target material for single-crystal diffraction, the radiation of Cu K_{α} is 1.5418\AA . These X-rays from the target material directed toward the sample, when the sample and the detector rotated, the reflected X-rays are recorded. The geometry of the XRD is that the sample rotates at the angle of θ , while the detector rotates at the angle of 2θ (showing in the Figure 9). When the reflected X-rays satisfied the Bragg's law, they will interfere with each other. The detector will record the X-ray's interference and shows the intensity peak.

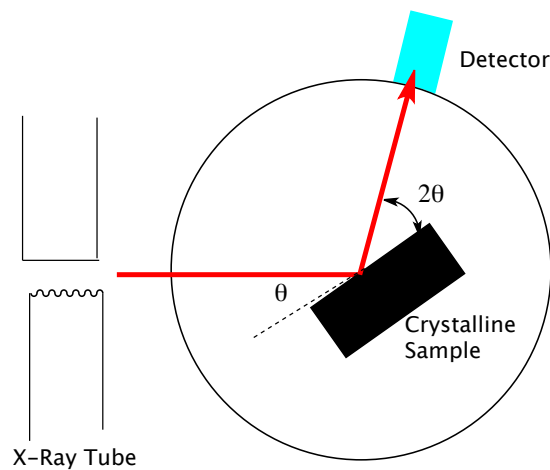


Figure 9 XRD scheme

2.2.1.1 Grain Size Measured by XRD

In the XRD analysis, the grain size is one of the most important parameter to be calculated. In order to get grain size, Scherrer equation can be used, which is gotten by the derivative of Bragg law (shown in Figure 10).

$$d = \frac{n\lambda}{2\sin\theta}. \quad (4)$$

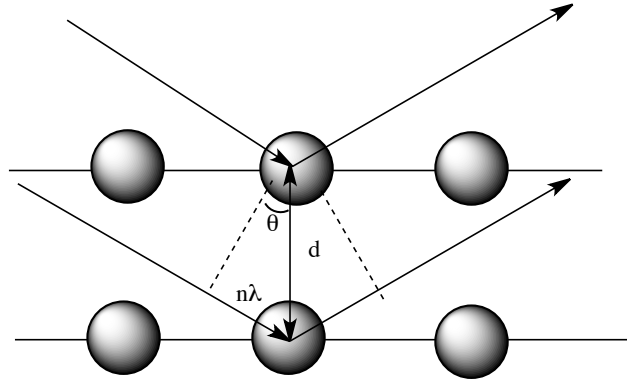


Figure 10 Bragg law scheme

Take Derivative in d and θ yields (holding the wavelength constant) get Scherrer equation as

$$2\Delta d \cdot \cos\theta \cdot \Delta\theta = \lambda. \quad (5)$$

The Scherrer equation predicts crystalline thickness if crystals are smaller than 1000\AA . Since small angular differences in angle are associated with large spatial distances (inverse space), Broadening of a diffraction peak is expected to reflect some large-scale feature in the crystal. Since $\Delta\theta$ can be positive or negative the absolute value and reflect the half-width of the peak (really half-width at half-height), so $2\Delta\theta$ is the peak full-width at half-maximum (β). Full-width at half-maximum (FWHM) is the width of a spectrum curve at half of the maximum amplitude. Δd reflects the crystalline thickness, which approximately equals to particle size:

$$\text{particle size} = t = \Delta d = \frac{K\lambda}{\beta \cdot \cos\theta_{\beta}}. \quad (6)$$

Take the shape factor $K=0.9$, then the Scherer equation is given by

$$\text{particle size} = \frac{0.9\lambda}{\beta \cdot \cos\theta_{\beta}}. \quad (7)$$

2.2.2 Raman Spectroscopy

Raman spectroscopy is a vibrational spectroscopic technique that measures the molecular vibration and crystal structures. In the instrument configuration, a laser source irradiates the

sample, produce Raman scattered light and a CCD camera is used to detect the amount of the scattered light.

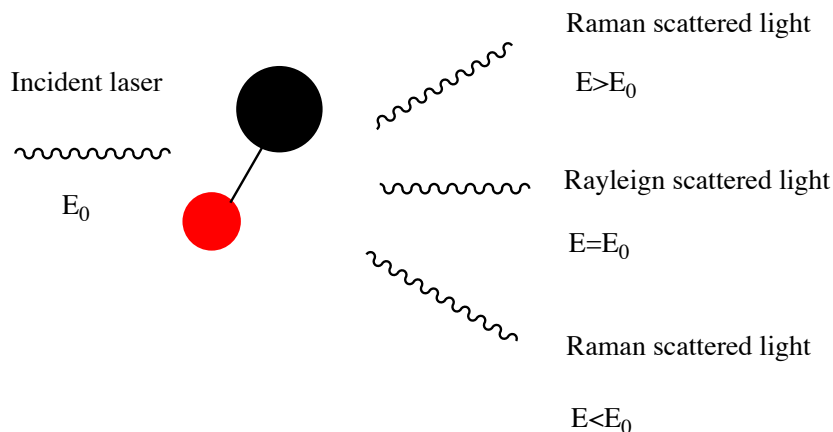


Figure 11 Light scattering by molecular

As shown in Figure 11, when the incident laser interacts with the molecular, it distorts the electron clouds to form a “virtual state” which is not stable then the photon will be radiated as scattered light. When the scattered light have the same energy as the incident laser light, it is Rayleigh scattering which means the electron in the ground level jumps to virtual level and falls to the original ground level. The frequency of the scattered light is the same as the incident light. Raman scattering (Stokes Raman scattering and anti-Stokes Raman scattering) is a process in which an electron is excited from vibration level or ground level to the ground level or vibration level.

In the Raman spectrum, the x axis is Raman shift which can be converted by Raman peak wavelength as

$$\text{Raman shift} = \frac{1}{\lambda_{\text{laser}}} - \frac{1}{\lambda_{\text{scatter}}} \quad (8)$$

Raman shift (wavenumber) is widely used because it is linearly related to energy. The peak position shows the specific vibration mold of each function group in the material molecular

“molecular fingerprint” of the material. The width of a peak shows the crystalline lattice, it can be used to measure the residual stress.

2.2.3 Differential Scanning Calorimetry (DSC)

Differential Scanning Calorimetry (DSC) is a thermal analytic method to detect the material’s heat capacity changing with the temperature, which is associated with the phase transition and chemical reaction. Because of its speed and availability, DSC is an easier way to detect the material’s phase transition such as glass transition, phase change and melt [69].

In a DSC instrument (Figure 12), only a few gram of the sample are required, the heat is introduced into the sample and the reference (normally an empty pan without the sample). When the sample has a phase transition, there will be more or less heat flowing to the sample than to the reference in order to keep the same temperature-changing rate. The absorbance or release of the heat depends on the exothermic or endothermic phase transition behavior of the material [70].

In the heat flux DSC, the total heat flow is dH/dt , it is the sum of the two terms (the heat capacity and the kinetic response of the sample) as

$$\frac{dH}{dt} = C_p \cdot \frac{dT}{dt} + f(T, t). \quad (9)$$

- H is the enthalpy (unit is Jmol^{-1})
- C_p is the specific heat capacity (unit is $\text{JK}^{-1}\text{mol}^{-1}$)
- $f(T,t)$ is the kinetic response of the sample (unit is $\text{J}\cdot\text{mol}^{-1}$)

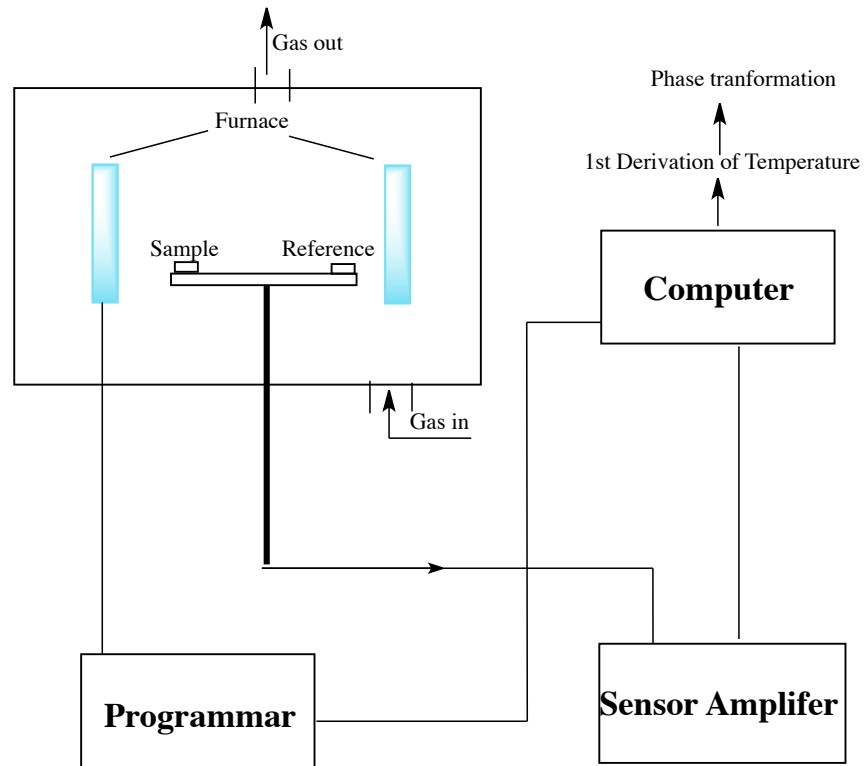


Figure 12 DSC scheme

2.2.3.1 Typical DSC Graph

The DSC graph (shown in Figure 13) is a curve of the heat flux vs. the temperature or the time. The enthalpy of the transition is calculated by integrating the peak. So the area under the peak is related to the heat absorbed or released from the transition. The height of the peak is proportional to the rate of the phase transition [70].

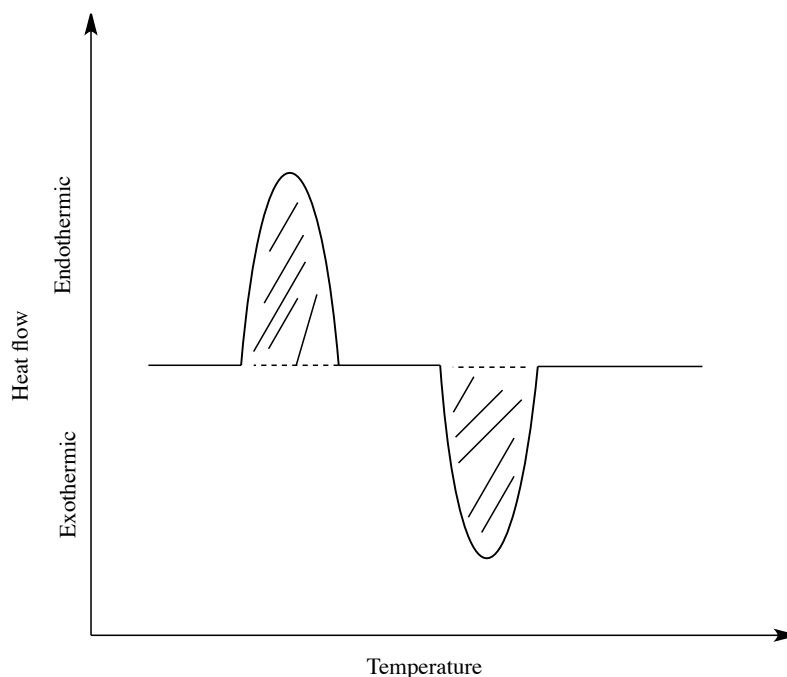


Figure 13 DSC data graph

2.2.4 X-ray Photoelectron Spectroscopy (XPS)

X-ray photoelectron spectroscopy (XPS) is a technique to measure the material chemical composition based on the photoelectric effect. As Figure 14 (a) shown the kinetic energy (K.E.) of the electron relates to the X-ray photon energy ($h\nu$), the binding energy (B.E.) of the electron and the energy (ϕ_{spec}) that is the spectrometer work function (the minimum energy required for the photoejected electron jump from the Valent band to the vacuum level). Then X-ray photoelectron spectroscopy (XPS) measures the kinetic energy and number of the photoejected electrons [71].

In general, the solid sample is introduced in the XPS chamber under ultra-high vacuum (below 10^{-8} mbar) and irradiated by the X-ray generated by Mg $K\alpha$ (1253.6 eV) or Al $K\alpha$ (1486.6 eV) [72]. When the sample atom absorbs the X-ray photons, the electron in the core level can be knocked out of the atoms (as shown in Figure 14 (b)). Ultra-high vacuum is necessary firstly because the gaseous contaminants absorbed on the sample surface may

contribute to the XPS spectra; secondly it enables the ejected electrons escape from the sample and reach the spectrometer analyzer.

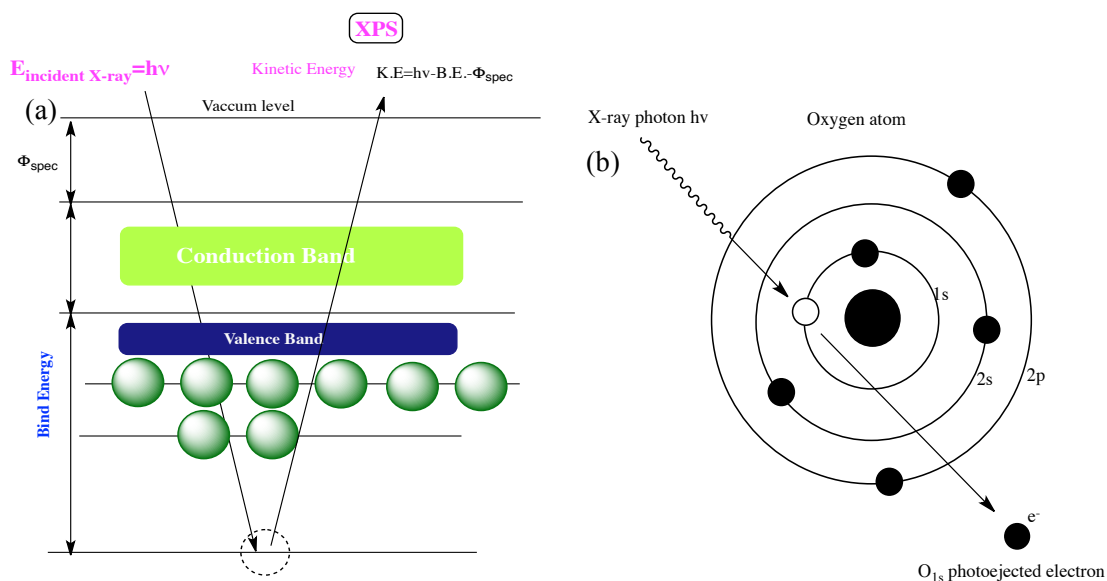


Figure 14 Electron excitement in XPS (a) and photoemission of O1s (b)

2.2.4.1 XPS Spectrum

XPS counts the electrons leaving from the sample surface when the X-ray irradiates the material. XPS spectrum shows the number of the electrons at a sequence of energies including both a contribution from the background signal and peaks of the bound states of the electrons in the surface atoms. In XPS, there are two kinds of spectra, survey and high-resolution spectrum. The survey spectrum is lower resolution spectrum on scale of binding energies between 1-1000eV. In this energy range, the characteristic peaks for each element are found. The peak intensities measure the amount of the element on the material surface, while the peak position decides the elemental composition of the material. The high resolution is measured in a narrow scale of the energy region, which related to the chemical bonds and electronic state of the element (shown in Figure 15).

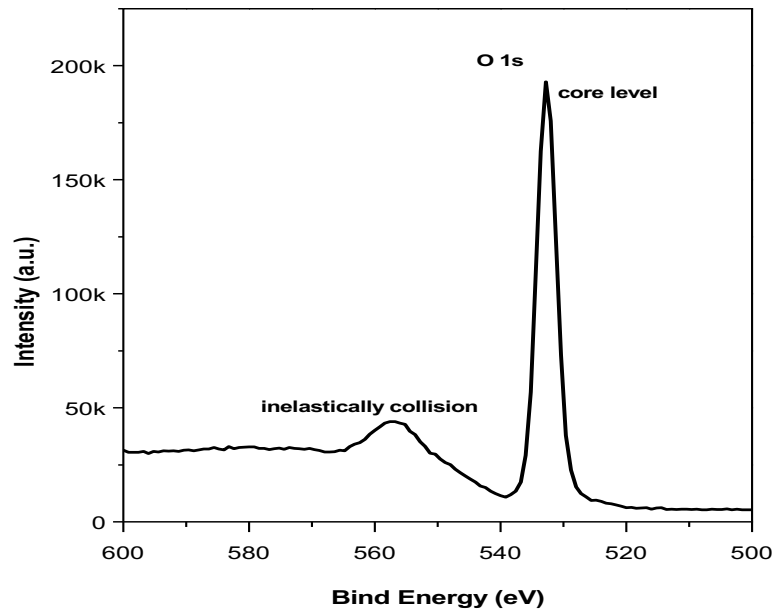


Figure 15 XPS spectra for the O 1s peak in Al_2O_3

2.2.4.2 Band Gap Measured by XPS

Normally the material band gap can be measured by UV-VIS spectrum, but for insulator the band gap from XPS is more accurate. The reason is listed on the below: The photo-emitted electron undergoes three different transitions before entering in the XPS spectrometer analyzer (1) the electron is excited by the X-ray photon (with energy $h\nu$); (2) the electron transport to the sample surface; (3) the electron escape from the sample surface into the vacuum. During the step 2, the electron may transfer energy to the high frequency plasma oscillations of the valence band electron, thus it will lose energy. Additionally in the step (3), the escaping electron inelastically scatters from the sample surface that causes the surface plasmon. However during step (2) and (3), the photoejected electron can excite another electron in balance band into the conduction band. It involves the excitation of an electron from a filled state to an empty state, which means that it excites an electron from below the Fermi energy level to above it.

For insulators that has wide-band gap (shown in Figure 16), this equivalents to an electron being excited from the valence band into the conduction band. Hence, the lower limit of inelastic loss is equal to the band gap of the insulator.

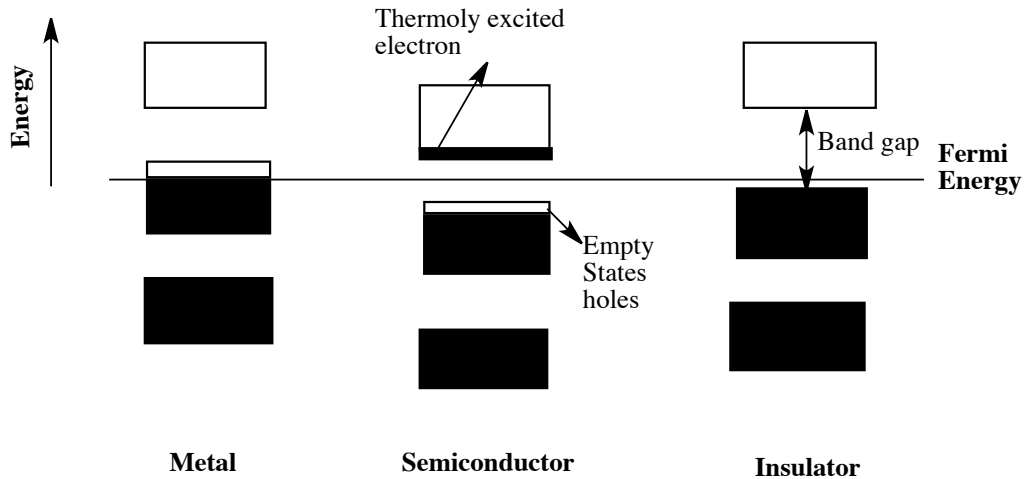


Figure 16 Energy bands in metals, semiconductors, and insulators

2.2.5 Electron Energy-Loss Spectroscopy (EELS)

EELS is an analytical technique measuring the kinetic energy loss of inelastically scattered electrons series after interaction with the target specimen. Based on the incident electrons' kinetic energy scale, it can divide to two type-high resolution EELS (a few hundred electron volts) and normal EELS (a few millielectron volts). EELS is achieved by connecting electron monochromators to transmission electron microscopes (TEM) [73]. EELS is based on a magnetic prism which generate a uniform magnetic field B (shown in the figure 17). In this field, electrons follow circular path with a bending radius of R , which depends on

$$R = \left(\frac{m}{e}\right) \cdot \left(\frac{1}{B}\right) \cdot v. \quad (10)$$

It means electrons with different kinetic energies will have different bending radius, in this way the electrons can be separated in the magnetic prism.

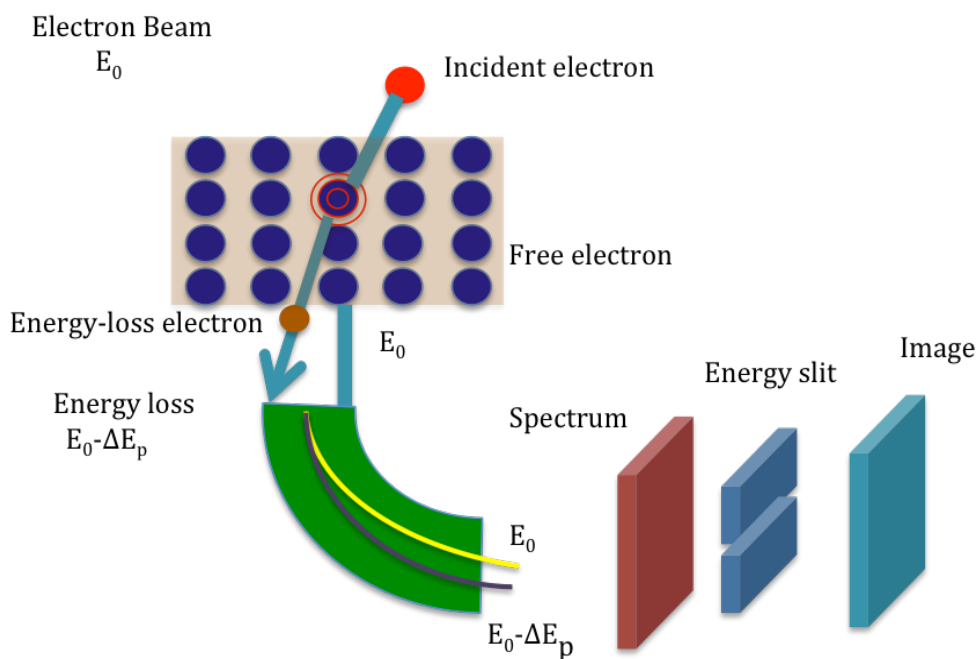


Figure 17 Configuration of EELS

The first peak (zero loss peak) appears at 0eV, represents electrons do not have inelastic energy loss, the electron scattered elastically. The FWHM of the zero peak is normally 0.2-2eV, represents mainly the energy distribution of the electron source. During the inelastic interaction of electron with the sample, the electrons can generate the plasmon oscillations frequently. This low loss region (<50eV) provides much information of the valence electron excitation. Through this, we can get the band gap of the material (shown in Figure 18).

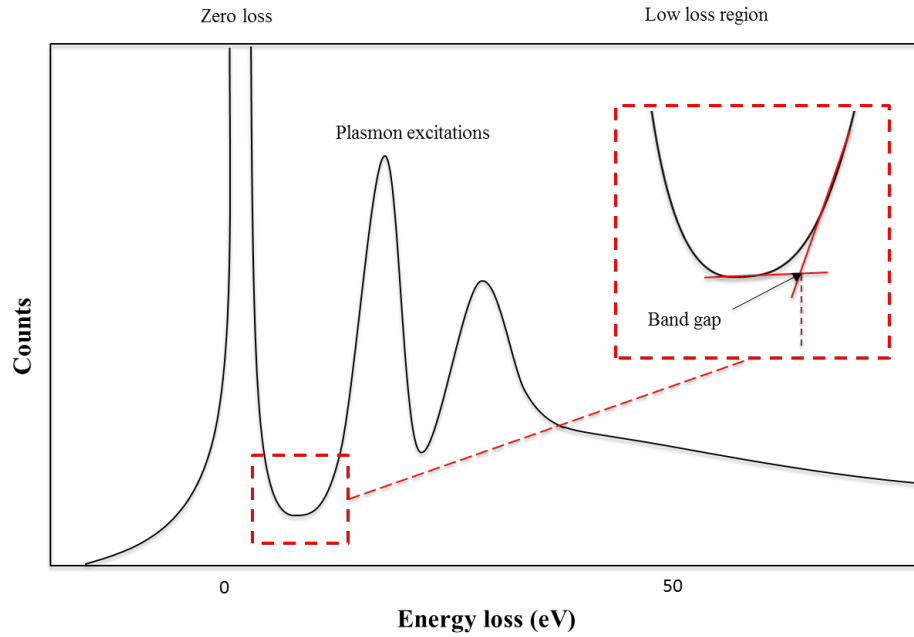


Figure 18 EELS spectrum

2.3 Deposition Techniques of Thin Films

In term of the deposition mechanism in vacuum system, thin film deposition can be divided into two categories: physical and chemical deposition process. The deposition goes through three main steps: firstly the atomic, molecular or ionic deposition species are created; secondly the species transport from the source to the substrate; then the depositing species condensed on the surface of the substrate directly or through the chemical reaction with an reactive molecule [74]. In the physical vapor deposition (PVD) process, the solid film is deposited via the condensation of the vapor phase atoms on a substrate and migration to the growth sites. The classic PVD included the evaporation, sputtering and ion plating [75]. In the chemical vapor deposition (CVD) process the film is formed by a vapor chemical reaction on the heated substrate surface.

There exists many ways to prepare corundum ($\alpha\text{-Al}_2\text{O}_3$) thin film including atomic layer deposition (ALD), chemical vapor deposition (CVD) and plasma enhanced chemical vapor

deposition (PECVD). The optical thin film can be prepared by physical methods such as evaporation and sputtering [38]. Among these, ALD is employed to adjust the film thickness and composition of the film [76]. In industry, crystallized Alumina coating is prepared by CVD process [77]. Unfortunately, the CVD have a higher requirement for the substrate temperature (above 1000°C) [39]. Even though physical vapor deposition can be operated at lower temperature, it is just for amorphous Al₂O₃ coatings [77].

Ion beam sputtering (milling) deposition (Figure 19) is a PVD process, which positive gas ions bombard the target to produce dislodging atoms that pass through the gas phase and deposit on the surface of the substrate. Compared with other vapor-phase deposition, in the sputtering deposition the sputtered atoms can have very high kinetic energies. This high kinetic energy can improve the films' properties and increase the film-substrate adhesion [75]. Based on the ion beam sources, there are two different categories: focused ion beam (FIB) and broad ion beam (BIB). They are different from the beam size, the current density of the beam, the incident angle and the beam scanning [78]. In FIB milling process, gallium ion was used and the accelerating voltage is 30kV [79]. Focused ion beam milling is commonly used in TEM sample preparation, the most important advantages of the FIB is that it can cut the sample at desired location and eliminated the damages. BIB milling is a process using lower-energy gas ion beam (such as argon Ar⁺ or helium He⁺). Compared with FIB, BIB milling process can mill a larger surface area of the target and it is widely used in the nano fabrication field [80].

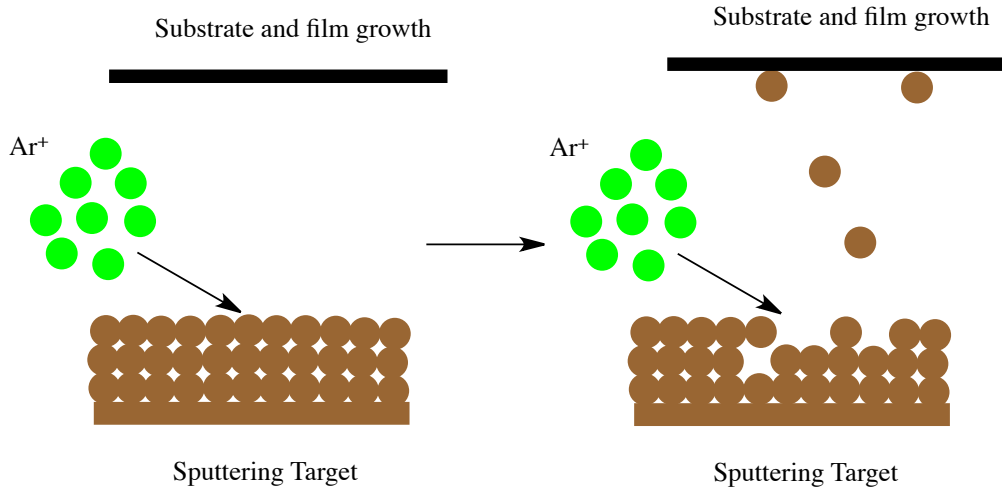


Figure 19 Ion beam sputtering process

2.3.1 Ion Beam Sputtering

2.3.1.1 Mechanism of the Ion Beam Sputtering

The broad ion beam sources were firstly used in electric space propulsion in some countries in the period of late 1950s and early 1960s. Later the application of ion beam greatly exceeded its initial application, at present it is widely used in thin film deposition [81].

The ion source in the BIB process applied in thin film preparation is gridded; it means there is an ion-optics grid in the system where ions are accelerated by the electric field (shown in Figure 20). The gas flows into the discharging chamber, the electrons from the cathode strike than ionize the gas atoms or molecule, then the gas ions reach the ion optics (the screen and accelerator grids) and are accelerated to form ion beam. The neutralizer's electron can charge and neutralize the ion beam.

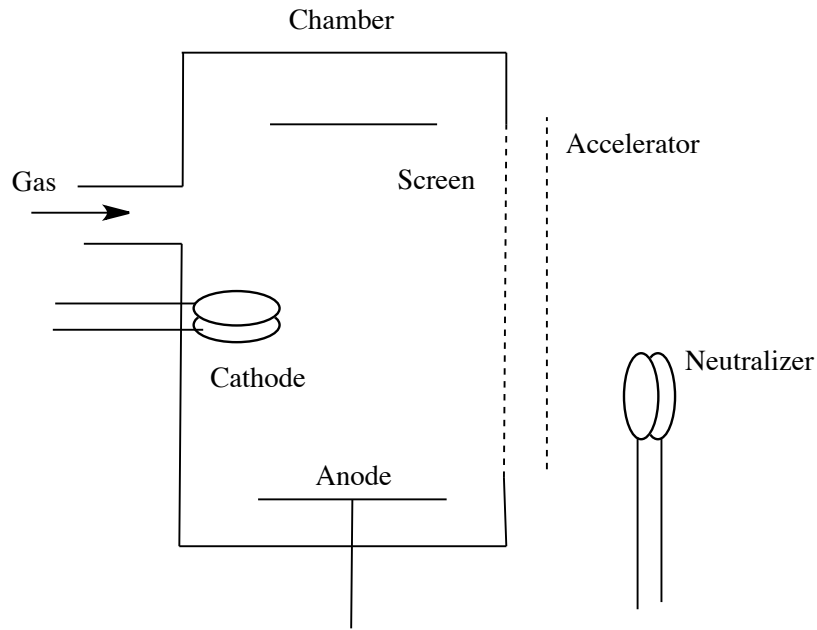


Figure 20 Schematic diagram of gridded ion source

The discharging chamber can produce ions efficiently; also it is easily controlled and maintained. Nearly all of discharging chamber configurations use a magnetic field to contain the cathode's emitting electrons, therefore improve the ion production efficiency at low operating pressures. This magnetic field is provided by the permanent magnets and electromagnets [81].

The ion beam accelerated by the ion optics, its maximum current can be given by

$$I \approx \frac{\left(\frac{\epsilon_0}{9}\right) \cdot A \cdot \left(\frac{e}{m}\right)^{\frac{1}{2}} \cdot V_t^{\frac{3}{2}}}{l_g^2} \quad (11)$$

- ϵ_0 is the permittivity of space.
- A is the beam area.
- $\frac{e}{m}$ is the charge to mass ratio of the accelerated ions.
- V_t is the total voltage ($V_b + V_a$).
- l_g is the gap between the screen and accelerator grids.

This equation is derived from the Child's law, this equation just give an approximate ion beam current, but the actual beam current is only 20%-50% of the equation.

2.3.1.2 The Application of Ion Beam Sputtered Thin Films

Broad ion beam applied in thin film deposition started in 1970s, and then is widely used in this area. The broad ion beam milling can be used as etching: the broad ion beam source accomplished by the physical sputtering can remove the target material. As with etching, deposition can be achieved by physical or reactive sputtering. Recently the application of broad-beam ion sources sputtering focused more on the thin film property-modification. The properties include adhesion, corrosion resistance, crystal orientation, magnetic anisotropy, refractive index and hardness [81]. Among them, the refractive index is one of the most important parameter to characterize the thin film's optical property [82, 83].

2.4 Sapphire or Ruby Thin Film Application I – Modifying the Refractive Index of Substrate

2.4.1 Refractive Index

When the incident light passed through the thin film, the possible phenomena are reflection, transmission, and absorption of the incident light. The intensity of the incident beam equals the sum of the intensities of the reflected, transmitted and absorbed beam:

$$I_O = I_R + I_T + I_A \quad \text{and} \quad (12)$$

$$R + T + A = 1. \quad (13)$$

Reflectivity $R = \frac{I_R}{I_O}$, Transmissivity $T = \frac{I_T}{I_O}$, Absorptivity $A = \frac{I_A}{I_O}$, these three represent the optical properties of the thin film.

Light is a propagating electromagnetic wave, which has both magnetic and electric field components oscillating perpendicular to each other. In the vacuum, light propagates at the speed of c . In different mediums, the light will propagate at different speed v . The refractive index n is the ratio of c to v that determine physicochemical properties of the optical medium. It is given in the following equation:

$$n = \frac{c}{v}. \quad (14)$$

c is the velocity of the light in vacuum, v is the light velocity in medium. The refractive index is one the most important parameters for the optical medium[84, 85]. When light propagates through different mediums, it obeys Snell's law (shown in Figure 21) that can be expressed as

$$n_1 \sin \theta_1 = n_2 \sin \theta_2. \quad (15)$$

- θ_1 and θ_2 are the angle of the incidence light and refraction light.
- n_1 and n_2 are two medium's refractive index

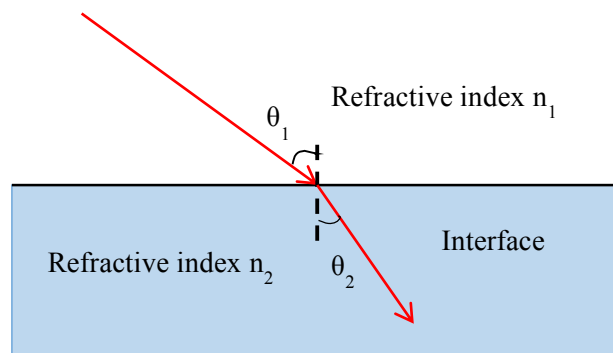


Figure 21 Snell's law

The refractive index decides how much the light is bent when light transfer from one medium to another. When light go through the high refractive index medium, the light rays will

be bent greater than the lower refractive index medium. Therefore less high refractive index material is needed for bend the same degree as a lower refractive index medium.

The refractive index can also determine the amount of reflected light, Brewster's angle and the critical angle for total internal reflection. At Brewster's angle (shown in Figure 24), p-polarized light will be totally transmitted. The Brewster's angle is given by

$$\theta_B = \arctan\left(\frac{n_2}{n_1}\right). \quad (16)$$

Brewster's angle is an angle at which the reflection losses are minimized. For example Brewster's Angle Laser Crystals are small Ti:Sapphire ($n=1.76$) crystals polished with Brewster's angle (around 60.4°) which can avoid laser modulation.

The critical angle for total internal reflection can be calculated by

$$\theta_c = \arcsin\left(\frac{n_1}{n_2}\right). \quad (17)$$

When the angle of incident light is higher than θ_c , the Snell's law cannot be applied. The light cannot be transmitted and will go through total internal reflection. For example light emitting diodes (LEDs) encapsulating resin prefer to use high refractive index material to increase the light extraction efficiency due to the internal reflection phenomena [86]. In addition, anti-reflective coating on the lens can eliminate the reflections in lenses and thus increase contrast and clarity of the lenses.

High refractive index thin film materials (typically $n > 1.65$) are used to improve the optical devices' optical behavior such as Bragg gratings and photonic crystals. The high refractive index thin film improves the materials' optical quality and transparency in the visible light range [82]. In optical devices, high refractive index thin films are widely used for producing the optical interference filters and mirrors [87].

2.4.2 Methods for Determining the Refractive Index of Thin Films

There exists various methods for determining the refractive index such as goniometric, refractometric and ellipsometric [85]. Goniometers are used for measuring angles, also it can be used for measuring the refractive index of the material by prism methods: least deviation, constant deviation and auto collimation [88]. The least-deviations method (LDM) is used to achieve highest accuracy. The method LDM contains getting the smallest angle of deviation for the rays transmitted the prism. Figure 22 shows a light path through the prism. The following equations can be written by using the refraction law and geometrical relationships

$$\sin\beta_1 = n \cdot \sin\theta_1, \quad (18)$$

$$\sin\beta_2 = n \cdot \sin\theta_2, \quad (19)$$

$$\theta_1 + \theta_2 = \alpha, \text{ and} \quad (20)$$

$$\beta_1 + \beta_2 = \varepsilon + \alpha. \quad (21)$$

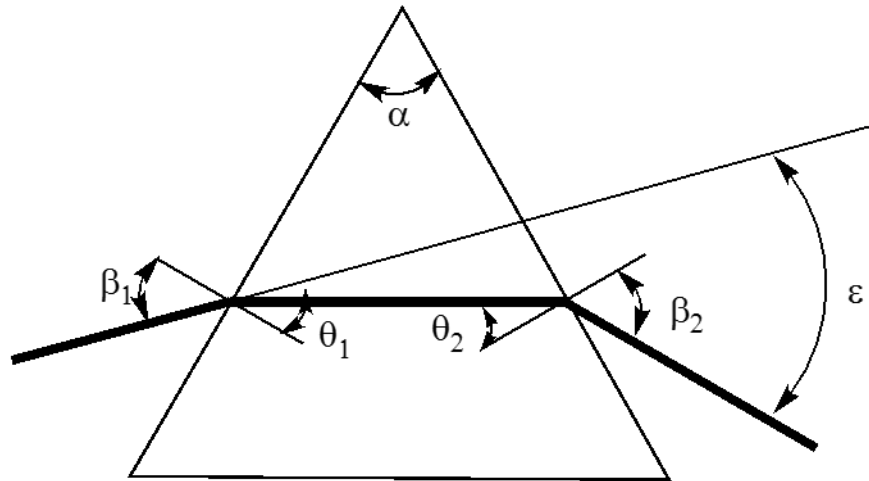


Figure 22 Refraction of a light through a prism

n is the relative refractive index of the prism, α is the prism's refractive angle, β_1 and θ_1 are the incidence and refraction angles at the first face of the prism. β_2 and θ_2 are the incidence and refraction angles at the second face of the prism, and ε is the desired deviation angle of the incident light from its initial direction. Eliminating the θ_1 and θ_2 from the equations, we get a formula as

$$\varepsilon(\beta_1) = \beta_1 - \alpha + \arcsin \left[n \sin \left(\alpha - \arcsin \left(\frac{\sin \beta_1}{n} \right) \right) \right]. \quad (22)$$

Deviate the above function to get the angle of least deviations with relationship to incidence β_1

$$\varepsilon_{\min} = 2 \arcsin \left(n \sin \left(\frac{\alpha}{2} \right) \right) - \alpha \quad \text{and} \quad (23)$$

$$n = \frac{\sin \left(\frac{\alpha + \varepsilon_{\min}}{2} \right)}{\sin \left(\frac{\alpha}{2} \right)}. \quad (24)$$

Figure 23 shows the relationship between the incident angle β and ε . It can be seen that as the incident angle increases, the angle of deviation ε decreases, but after passing the minimum ε_{\min} , it increases. Such phenomenon forms the basis of the LDM with visual goniometer [88].

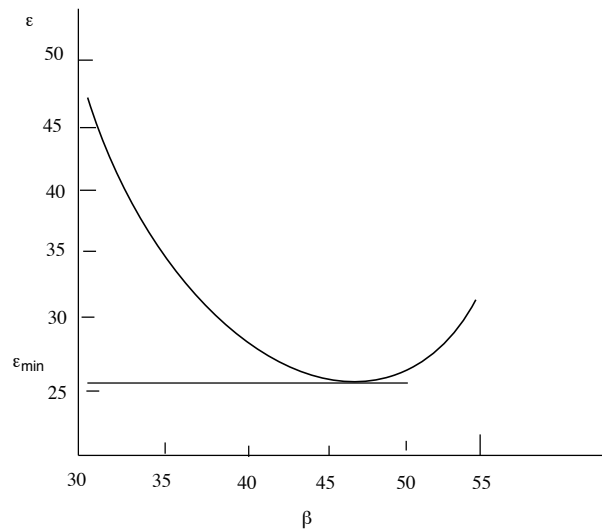


Figure 23 The angle of deviation changing with the incident angle

For the refractometry, the Brewster's angle was measured to get the refractive index. When the ray goes through the boundary between two transparent media, generally its optical power partially is reflected. However at Brewster's angle the reflection does not occur, it means the light is p-polarized. The magnitude of the Brewster's angle related to the refractive index of the optical media, it is given by

$$\theta_B = \arctan \frac{n_2}{n_1}. \quad (25)$$

n_1 and n_2 are the refractive indexes of the medium of the incident beam and the second medium. So if the refractive index of the medium of the incident beam is known, we can get the other medium's refractive index by the Brewster's angle (shown in Figure 24).

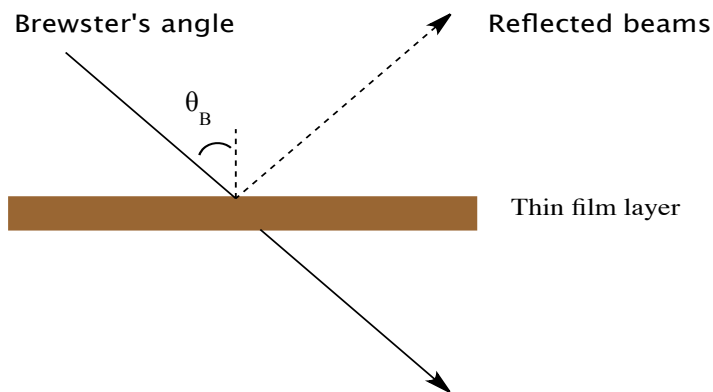


Figure 24 Brewster's angle

Among them, ellipsometry is a convenient and accurate way to measure the thickness and refractive index of the thin film on the substrate surface. The thickness limit measured by ellipsometry is one order of magnitude smaller than other means such as interferometry [89]. The mechanism of ellipsometry is to measure the changes in the state of polarization of light after reflection from the surface. A thin transparent film on the substrate leads to changes of the

light polarization states from which the refractive index and thickness of the film can be determined.

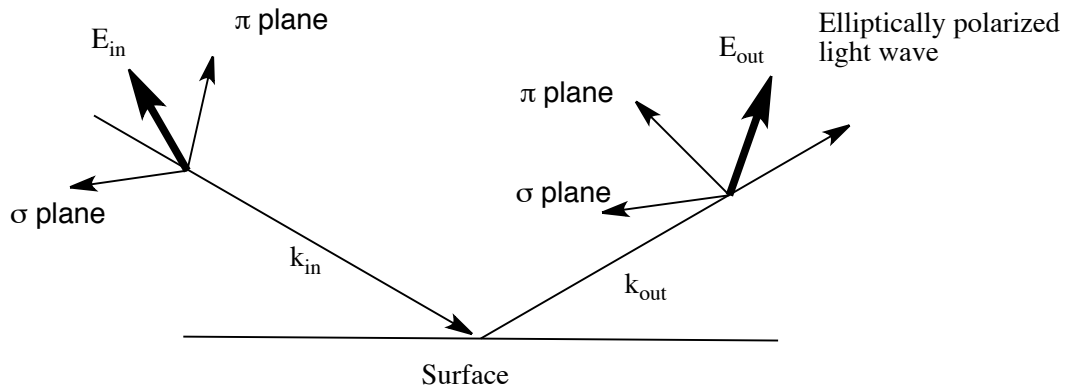


Figure 25 The principle of the ellipsometry [90]

When the plane light wave passes through the transparent surface, the incident plane is defined as a plane perpendicular to the surface. The propagating direction vector is the wave vector k_{in} . The vectors for the electric field E and the magnetic field B of the light wave are perpendicular to k_{in} . The chosen E -vector is defined the polarization of the light wave (shown in Figure 25). The two components of vector E (σ and π) are parallel and perpendicular to the incident plane.

The incident light is linearly polarized; it means the amplitude and mutual phase make the endpoint of E move in a straight line in the σ - and π - components. However when the light reflects from the surface, the amplitude mutual phases of the σ - and π - components cause the endpoint of E to move in an ellipse. The light wave changes to elliptical polarized.

In the ellipsometry, the detector and data processing can measure the ellipsometric parameters Ψ and Δ . Ψ is primarily a function of n (the refractive index of film) and ϕ (the angle

of the light refract through this film). Δ is a function of the film's thickness. The ellipsometric parameter is related to the reflection coefficients of the polarized light parallel and perpendicular to the incident light plane ρ_σ and ρ_π , respectively. The relation shown in the following equation

$$\rho = \frac{\rho_\pi}{\rho_\sigma} = \tan(\psi) \cdot e^{j\Delta} . \quad (26)$$

The two reflection coefficients (ρ_σ and ρ_π) are functions of the material's refractive index. Ellipsometry is used to measure the thickness or refractive index of the thin film on top of the substrate. If the refractive index of the film is known, ellipsometry can measure the thickness of the thin film; while if the thickness is known, ellipsometry can calculate the refractive index of the thin film.

2.5 Sapphire or Ruby Thin Film Application II – Measuring the Residual Stress of Superconductor YBCO Thin Film

2.5.1 Residual Stress in YBCO Thin Film

It is unavoidable for thin film to have residual stresses because of the thermal misfit and structural variation between the substrate and the actual deposit. The residual stress plays a key role on determining the film's service life [91]. The critical point in this technological process is that residual compressive stress can cause the delamination of the film. While residual tensile stress may induce micro cracks in the film. The residual stress cannot be eliminated by heat treat, therefore it is necessary to find a cost effective way to measure the residual stress in the thin film. It is well known that Ruby has two luminescence bands R1 and R2 in the range of 4300cm^{-1} to 4500cm^{-1} , which is highly sensitive to temperature and pressure [54]. Therefore, Raman shift of R1 and R2 bands is proposed herein to accomplish this degree measure the residual stress of superconductor thin film. In this case we used $\text{YBa}_2\text{Cu}_3\text{O}_{7-\delta}$ (YBCO) thin film

that is known for its superconducting properties as well as producing microwave and high power electrical devices application [92].

2.5.2 Residual Stress Measured by Raman Spectrum

If there is tensile stress in a crystalline structure, the crystalline lattice will increase and the number of layers are reduced. Because the surface atoms of the crystalline will bond to less neighbors, the interlayer Van der Waals will decrease which results in weaker restoring forces in the vibration. Thus there is red shift of Raman peak when there is tensile stress in the crystalline structure. By contrast, if there is a compressive stress exists in the crystalline the atom will pack closely, it will increase the Coulomb interaction and in turn the restore force in the vibration and lead to blue shift of Raman peak [93]. The value of the stress is given by [94-96]

$$\Delta\varepsilon = b\Delta\omega . \quad (27)$$

$\Delta\omega$ is the Raman frequency shift, $\Delta\varepsilon$ is the amount of stress in strained material, b is the coefficient of strained material.

CHAPTER 3

EXPERIMENTAL SET-UP AND TECHNOLOGY

An overview of the synthetic procedures (Figure 26) applied in the project is presented below. Firstly the mechanical milling process was used to generate core material powder for the next experimental step (French Press, heat treatment and ion beam sputtering process).

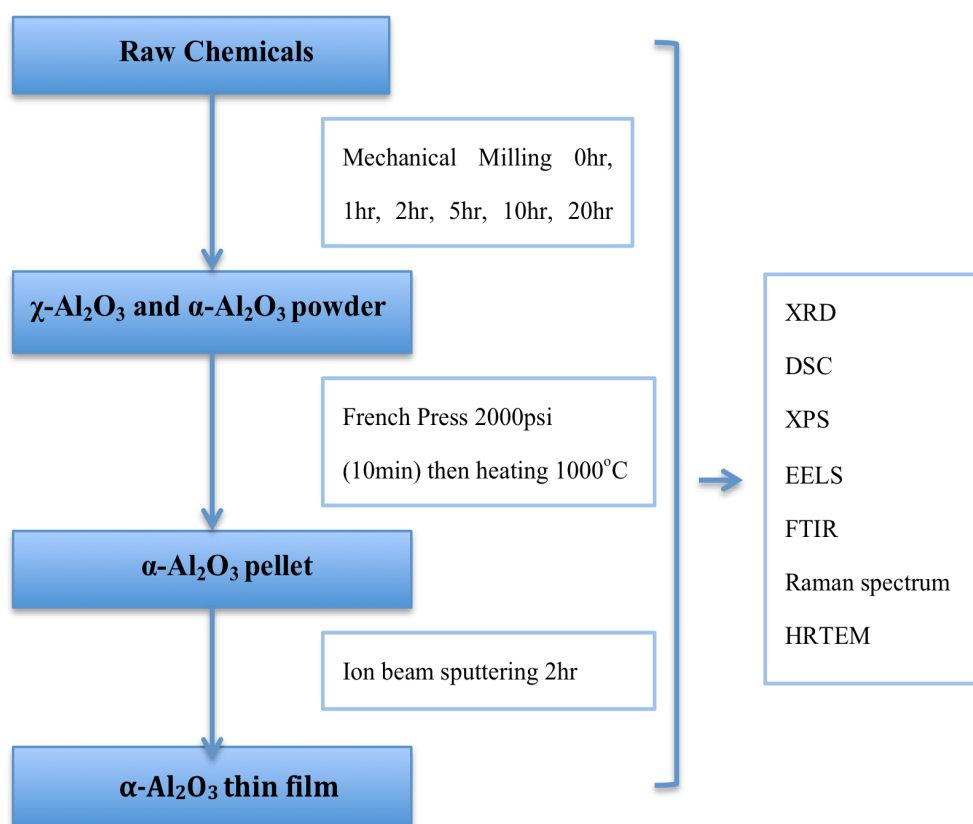


Figure 26 The synthesis procedure

It is important to show the mechanical milling effects on the alumina phase transformations, so various characterization methods are applied to evaluate results of the experiment. Also sapphire or ruby thin film was generated through the ion beam sputtering. Then Ellipsometry instrument was used to measure the optical property of the thin film.

3.1 Synthesis Process

In this work, we present a unique method to transform pseudoboehmite to other phase (shown in Figure 27). Table.1 shows all of the chemicals used in this synthesis process. Conventionally pseudoboehmite is transformed into χ or α -alumina phase by heat treatment. Here we explore mechanical milling as an alternative way to reduce the phase transformation temperature (around room temperature). The partially transformed phase is the key for a low temperature transformation into other phases.

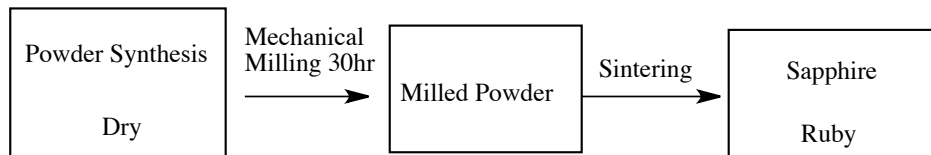


Figure 27 Synthesis process from PB to sapphire or ruby

The pseudoboehmite was synthesized from 0.2M water based aluminum sulfate. The solution was heated to 60°C with vigorous stirring. Once the temperature is reached commercial ammonia (NH₃) gas is pumped into the solution to reach a pH between 9-10 [97]. Temperature and pH were maintained constant during the synthesis. During the synthesis there are two reactions, equations (28) and (29) represent the two reactions in the precipitation process. At the end of the reaction, the products obtained are filtered and washed with distilled water for a number of times. The washing process is ended when the washing solution has a constant pH of 7. The resulting product is dried at 100°C for 24 hr. The product is our raw material known as pseudoboehmite (PB) (shown in the following Figure 28).

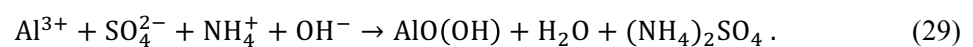
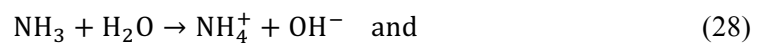


Table 1 Chemicals for the experiment

Names	Chemicals	Purity	Company
Aluminum Sulfate	$\text{Al}_2(\text{SO}_4)_3 \cdot \text{XH}_2\text{O}$	$\geq 98\%$	Sigma Aldrich
Chromiusulfate Hydrate	$\text{Cr}_2(\text{SO}_4)_3 \cdot \text{XH}_2\text{O}$	$\geq 98\%$	Sigma Aldrich
Ammonia	NH_3	99%	MATHESON

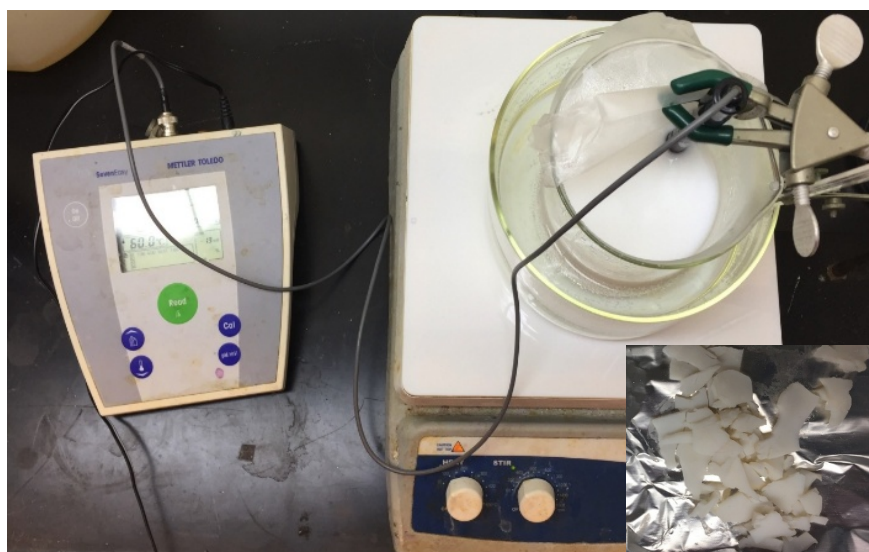


Figure 28 PB powder synthesis and drying

3.2 Mechanical Milling

There are two precursors: pseudoboehmite powder (PB) and chromium doped pseudoboehmite powders (PBCr). The milling is carried out from 0 to 50hr in a high energy

Spex mill (shown in Figure 29) with sets of five steels balls, two of 12.5mm and three of 6 mm. The milling load was of 10grams every batch.



Figure 29 Spex milling machine

3.3 Characterization Methods

3.3.1 Thermal Analysis

The thermal analysis was performed in a SETARAM Differential Scanning Calorimeter Analyzer (DSC) (shown in Figure 30) equipment. The raw and 30 h milled powders were analyzed at a heating rate of 15 °C/min up to a maximum temperature of 1200 °C in argon atmosphere.



Figure 30 DSC

3.3.2 X-ray photoelectron spectroscopy (XPS)

X-ray photoelectron spectroscopy (XPS) data were collected on a Physical Electronics Model 5700 instrument (Figure 31 (d)). Photoemission spectra were produced using a monochromatic Al K α X-ray source (1486.6 eV) operated at 350 W. The XPS samples for analysis were prepared by placing powder on the sample holder surface by carbon double tape.

3.3.3 X-Ray Diffraction (XRD)

X-Ray diffraction measurements of these samples were conducted in a Rigaku Smart Lab SE Multipurpose X-ray diffraction system (Figure 31 (a)) with a Bragg-Brentano geometry and Cu-K α radiation ($\lambda = 1.5418 \text{ \AA}$).



Figure 31 The characterization instruments (a) XRD (b) FTIR (c) Raman (d) XPS

3.3.4 Fourier Transform Infrared Spectroscopy (FTIR)

For measurement of sample powder, approximately 10mg of each sample was investigated on a Thermo Scientific Nicolet iS50 FT-IR Spectrometer (Thermo Fisher, USA) (Figure 31 (b)) using a diamond single reflection attenuated total reflectance (ATR) accessory equipped by a zinc selenide crystal. The software OMNIC version 8 was used for spectral acquisition. Infrared spectra were obtained in the range of $4000\text{--}600\text{cm}^{-1}$ with a spectral resolution of 4cm^{-1} . The averaged spectra were obtained using 32 scans including subtraction

of a background scan of the clean diamond crystal. The diamond was cleaned between samples using alcohol.

3.3.5 Raman Spectroscopy

The Raman spectroscopy was conducted on a confocal micro-Raman microscope Xplora™ Horiba JY (Figure 31 (c)). A 785 nm diode laser was used for excitation. Grating is 1800T, Filter is 100%, and acquisition time is 10s.

3.3.5 High resolution transmission electron microscopy (HRTEM)

High resolution transmission electron microscopy (HRTEM) was performed using a transmission electron microscope JEM-2200FS JEOL operated at 200kV. The image analysis for the HRTEM micrographs is conducted using Digital Micrograph that is capable of reproducing the Fast Fourier Transformations (FFT) and their Inverse (IFFT) images for a more in depth analysis.

3.4 Preparation of Sapphire or Ruby Pellet as the Target for Ion Beam

Sputtering

The sapphire or ruby target sample was prepared as a compacted pellet from the powder, by pouring approximately 10g of 30hr milled PB or PBCr (PB mixture with 2% Cr₂O₃) powder in a 2cm diameter cell. The cell is positioned in the French press instrument (shown in Figure 32 (a)), then the cell (Figure 32 (b)) is pressed using 13.8MPa for 30min. In order to get pure sapphire or ruby pellet, the PB 30hr or PBCr 30hr pellet were heated at 1000°C in the furnace for 3hr (shown in Figure 32 (c)). Through this process, we synthesized (Figure 33 (b)) or ruby (Figure 33 (c)) target that is 2cm radius with 1mm thickness. The samples were used for various characterization methods as well as sputtering.

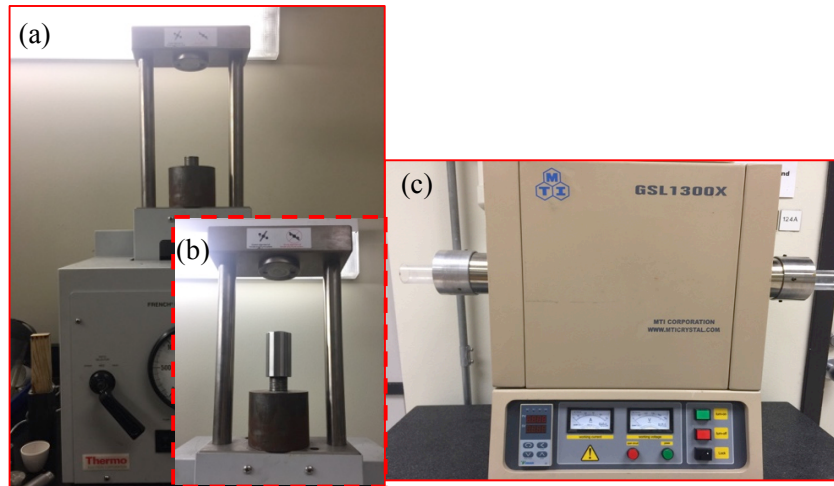


Figure 32 Instruments for producing target (a) the French press (b) the cell (c) the furnace



Figure 33 (a) Synthesized pseudoboehmite (b) sapphire pellet (c) ruby pellet

3.5 Ion Beam Sputtering Process

Figure 34 shows the ion beam-milling instrument, there are seven components: cryopump, roughing valve, ion source, cryo valve controller, ion source controller, Ar gas controller and pressure indicator. The procedure shows in the below:

Load a sample. Close the cryopump valve, vent the chamber and open the chamber lid. The sample is placed on the holder plate, then put it back into the chamber. Open the rough

pump, wait for the chamber pressure to reach below 5.0^{-2} Torre. Close the rough pump valve and open the cryopump valve. Wait for the cryopump LED turn to green, turn on the ion gauge. Wait for the IG pressure to reach below 5.0^{-6} Torre.

Running a preprogrammed process. Turn on the Ar gas controller, wait for the IG pressure to be stable. Press the Discharge Enable button and Beam Enable button to start milling. After a certain time milling, press the Discharge Enable button and Beam Enable button to stop milling. Wait for 15min for the source to cool down. Turn off the Ar gas controller and ion gauge.

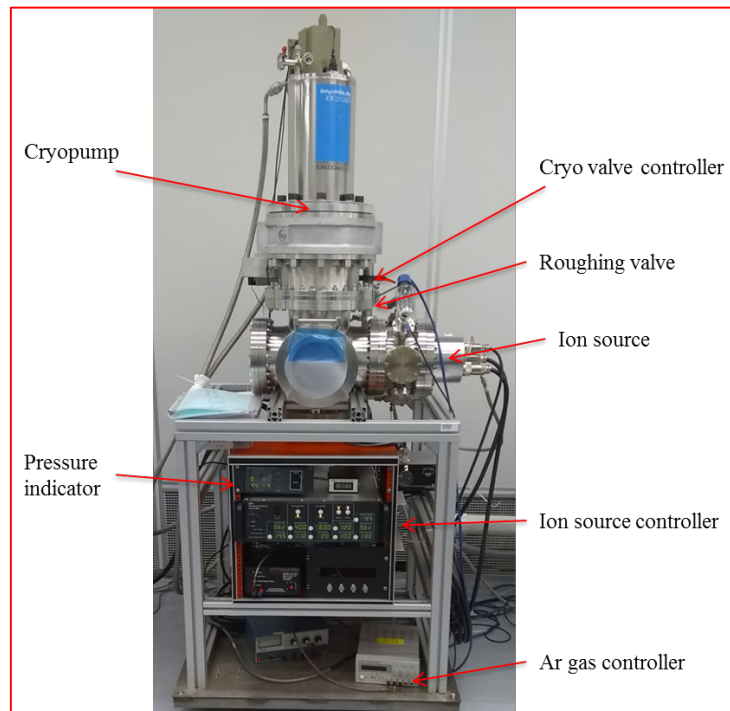


Figure 34 Ion beam milling instrument

Unload the sample. Close the cryopump valve and vent the chamber, then take the sample out from the chamber.

During the milling process, the sample stage is stable. The milling beam voltage is 600 V and the milling beam current is 120mA. The ruby or thin film sample (thickness is around 150nm) is prepared during 120min ion beam milling.

3.7 The Ellipsometry Measurement for the Refractive Index of the Ruby Thin Film

Approximately 150nm thick ruby film is grown on the silicon wafer by the ion beam sputtering process (shown in Figure 35). The refractive indices were measured by the Gaertner Ellipsometer (Gaertner Scientific Corporation) and analyzed using the Gaertner Ellipsometer Measurement program (Gaertner Scientific Corporation). Ellipsometric Ψ and Δ data was got at the wavelength of 632.8nm and incident angle 70° . The data was fitted by the thin oxide model to obtain the thin film thickness and refractive index. Since ruby thin film is transparent and has minimum absorption at this wavelength.

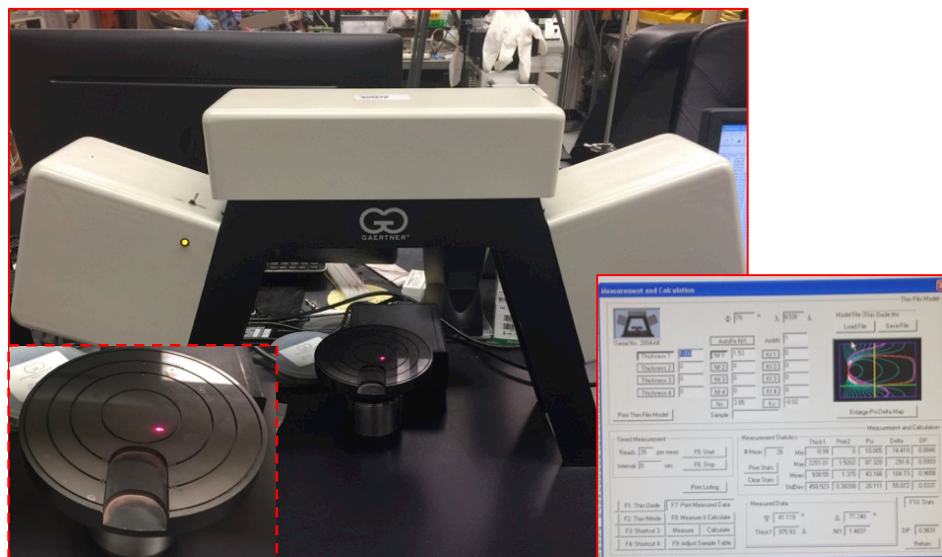


Figure 35 Gaertner Ellipsometer

3.8 The Stress Measurement for the Superconductor YBCO Thin Film

In this application study, Ni tape was chosen because it is a common substrate for YBCO thin film deposition. Firstly, ruby film (approximately 150nm thick) is coated on the bottom of Ni tape by ion beam sputtering process. Figure 36 (a) and (b) show the Ni tape's surface looking before and after ion beam sputtering ruby.

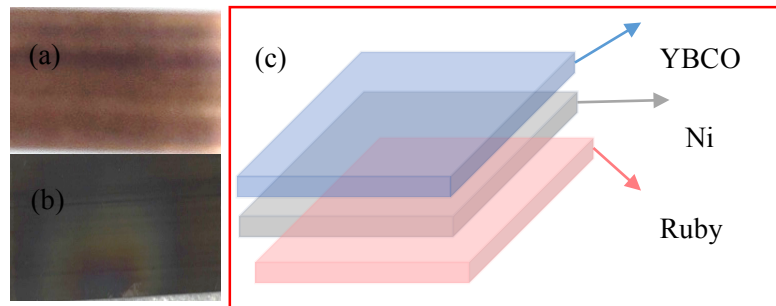


Figure 36 (a) Ni tape surface looking before ion beam sputtering ruby (b) Ni tape

Then the top of the tape is deposited YBCO by MOCVD, the whole Ni tape structure is shown in Figure 36 (c). Before and after the MOCVD, Raman spectroscopy was used to measure the tap's bottom ruby layer's R_1 and R_2 band peak; The Raman spectroscopy was conducted on a confocal micro-Raman microscope XploraTM Horiba JY (Figure 31 (c)). For excitation the used laser wavelength is 532nm, the residual stress of the YBCO was calculated by the Raman peak shift.

CHAPTER 4

RESULTS AND DISCUSSION

4.1 Mechanical Milling

4.1.1 Phase Transformation

4.1.1.1 PB Phase Disappearance and α -Al₂O₃ Phase Appearance

In order to study the phase transformation of PB during mechanical milling process, the XRD was used. Figure 37 shows the XRD patterns of the pseudoboehmite powders with different ball milling times. According to the XRD reference pattern (21-1307 JCPDS), the pseudoboehmite shows the following seven diffracting planes: (020), (120), (031), (200), (151), (002) and (251). Compared with the crystalline boehmite, (020) is slightly shifted toward lower angles due to the presence of interlayers of water [98-101]. During the whole milling process, there is no reflection from the milling medium's ingredients (the steel balls and steel vial). From raw pseudoboehmite to the 30hr milled sample, there is no significant change in the XRD pattern, just continuous peak broadening and a small peak position shift. It is obvious that 20hr and 30hr milled sample, (020) plane disappeared, (120), (031), (200), (151), (002) and (251) peaks clearly broaden. In the 50hr milled sample, the pseudoboehmite no longer exists, the χ -Al₂O₃ phase is the only phase observed (13-0373 JCPDS). Also after 10hr of ball milling, the planes (151) and (251) which belong to the typical pseudoboehmite reflections no longer present because of the transformation to χ -Al₂O₃. In previous studies, the χ -Al₂O₃ has been synthesized at temperatures between 300 and 500°C [102-104]. Mechanical milling is so unique phase transformation path that it can produce χ -Al₂O₃ phase at room temperature without other phases θ , γ , κ , and δ [105].

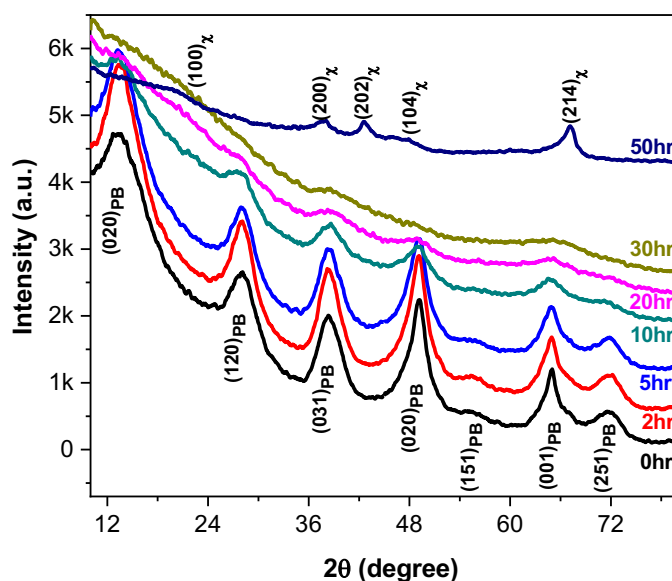


Figure 37 Diffraction patterns of the raw and milled PB. PB and χ -Al₂O₃ stand for pseudoboehmite and chi-alumina respectively.

Raman spectra are another way to show the crystalline change of PB with different milling time. Figure 38 shows the Raman spectroscopy data of PB with a 785nm laser excitation in the range of 200cm⁻¹ to 1100cm⁻¹.

It is observed that PB 0hr, 2hr, 5hr, and 10hr showed two significant active modes ~355cm⁻¹ and 983cm⁻¹. As the milling time increased, the vibrational modes became broader and its intensity decreased. It is because the mechanical milling affects the structure of pseudoboehmite, its crystal quality and grain size during the process. After 10hr milling, the PB 20hr, 30hr and 50hr lose the vibrational modes in this range. It indicates that after 10hr milling PB's crystalline starts to transform to other phases, which is consistent with Figure 37 XRD data.

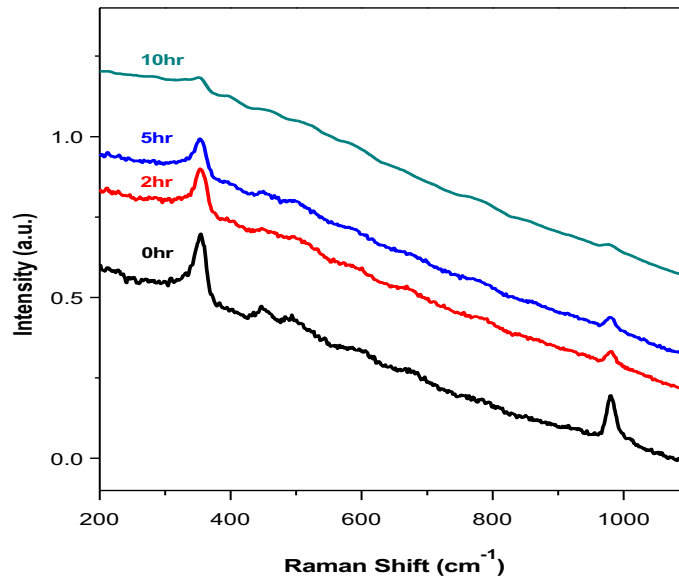


Figure 38 Raman spectra of raw and milled PB with an excitation line of 785 nm.

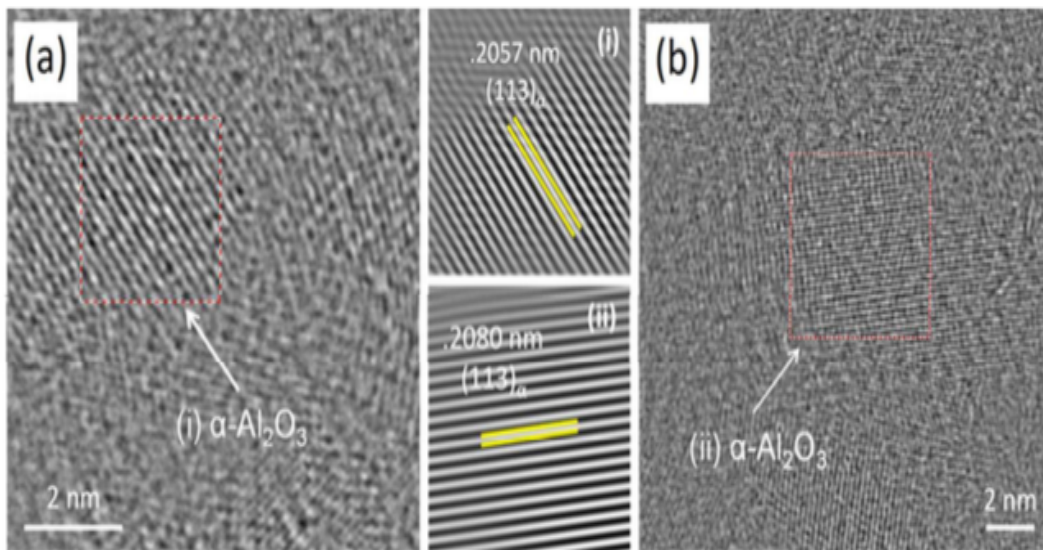


Figure 39 (a, b) HRTEM images and interplanar measurements for the PB 20hr and 30hr samples.

Since phase existing in PB 20hr and 30hr is not traceable by XRD and Raman measurement, HRTEM was employed to measure PB 20hr and 30hr (shown in Figure 39).

The analysis of interplanar measurements shows the existence of the crystalline α - Al_2O_3 in both samples.

4.1.1.2 Mechanism of the Phase Transformation

XRD and Raman data together show the phase transformation during mechanical milling process; additionally HRTEM shows the sapphire phase was successfully synthesized in the room temperature during 20hr or 30hr mechanical milling process. In order to find the mechanism of the phase change, Fourier Transform Infrared Spectroscopy (FTIR) over the range $4000\text{-}600\text{cm}^{-1}$ was employed to study the chemical bond changing during the milling process. Figure 38 shows the FTIR spectrum of pure pseudoboehmite with different milling time 0hr, 1hr, 2hr, 10hr, 20hr, and 30hr. In Figure 40 (a) from 0hr to 20hr the band belonging to bending vibration of Al-O-H was shifted from 1065 cm^{-1} to 1124cm^{-1} , the 744cm^{-1} OH torsional mode shown in PB 0hr disappeared after 2hr mechanical milling and the band at 855cm^{-1} which represents the $[\text{AlO}_4]$ stretching mode started to appear from 2hr milling [9]. The reason for this is PB exists as the type of $[\text{AlO}_6]$, mechanical milling destroys the PB's water layer, $[\text{AlO}_4]$ which has a shorter Al-O bond begins to appear after 2hr milling [99]. As the milling time increase, the amount of $[\text{AlO}_4]$ in milled samples is increased. Figure 40 (b) shows the broad band at around 3310cm^{-1} belonging to OH bonding stretching vibrations (the $\nu_{\text{as}}(\text{Al})\text{O-H}$ and $\nu_{\text{s}}(\text{Al})\text{O-H}$ stretching vibrations or OH stretching mode in PB H_2O structure) began shift to 3400cm^{-1} , also the shoulder peak (2939cm^{-1}) appears in sample PB 20hr and PB 30hr [106]. This is another proof that the water structure in PB is eliminated during milling. The band at 1638cm^{-1} assigned to the bending vibration of the hydroxyl bands in adsorbed water molecules is so weak (shown in Figure 40 (c)), it means that the water absorbed on the

PB's surface can be neglected [25, 107, 108]. On the other hand, it indicates the damaged water molecule is in PB's structure and not from the surface absorption.

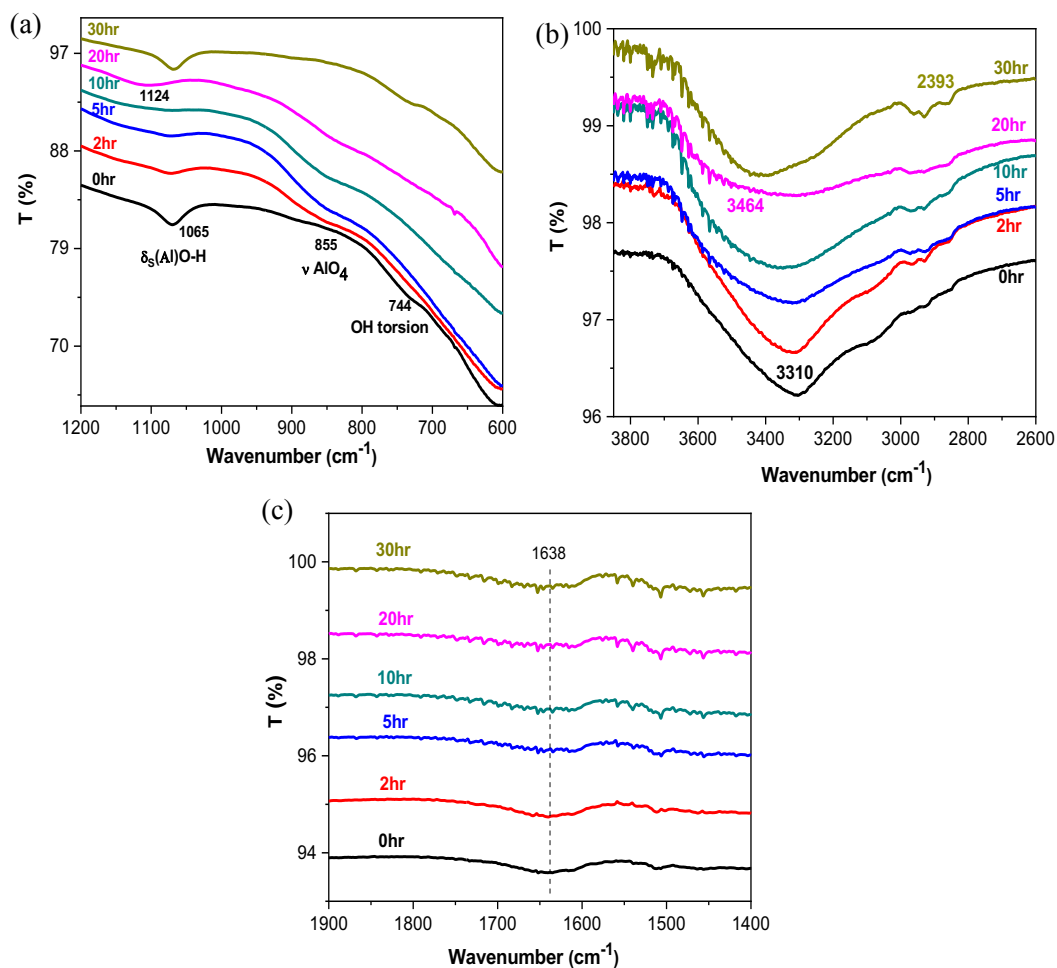


Figure 40 FTIR spectrum of pure pseudoboehmite with different milling time (a) OH stretching vibrations; (b) Al-O-H bending vibration; (c) the lack of bending vibration of the hydroxyl bands

FTIR data indicates that OH bonds between the PB layers structure (shown in Figure 41(a)) is firstly broken, because the hydrogen bonding in the PB layer is weaker than the ionic bond in the structure. The hydroxyl group diffused from the PB's structure, then formed water to finish the phase transformation (shown in Figure 41 (b)).

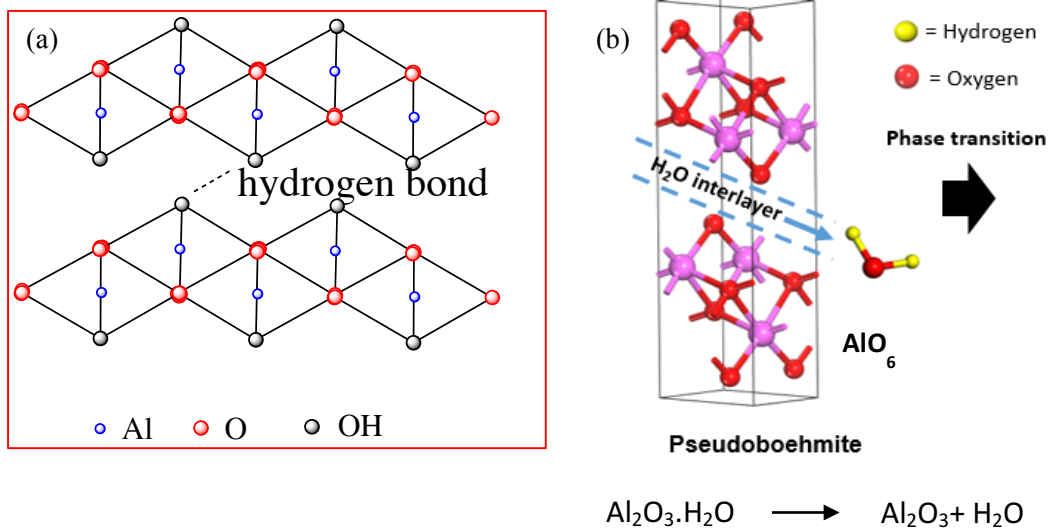


Figure 41 (a) PB crystalline structure and (b) mechanism of phase transformation

4.1.1.3 Novelty of Mechanical Milling on the Phase Transformation

In order to explore the critical point of mechanical milling for phase transformation from PB to $\alpha\text{-Al}_2\text{O}_3$, raw (PB 0hr) and milled 30hr sample (PB 30hr) were analyzed by DSC. Figure 42 shows the heat flow profile of the PB 0hr and 30hr. We can observe that PB 0hr has two endothermic reactions; one around 100°C is water removing and the one around 400°C associated to dehydroxylation. However for PB 30hr, there is only one endothermic reaction attributed to combination of dehydration and dehydroxylation. Base on the energy balance, the reduction in the energy requirements of 58% for the milled sample to transform into $\chi\text{-Al}_2\text{O}_3$. According to previous transformation research, we identified at higher temperatures the PB 0hr and PB 30hr have the presence of the following intermediate phases $\delta\text{-Al}_2\text{O}_3$ and $\kappa\text{-Al}_2\text{O}_3$ [109, 110]. In both cases the intermediate phases transform into $\alpha\text{-Al}_2\text{O}_3$ as the temperature increases.

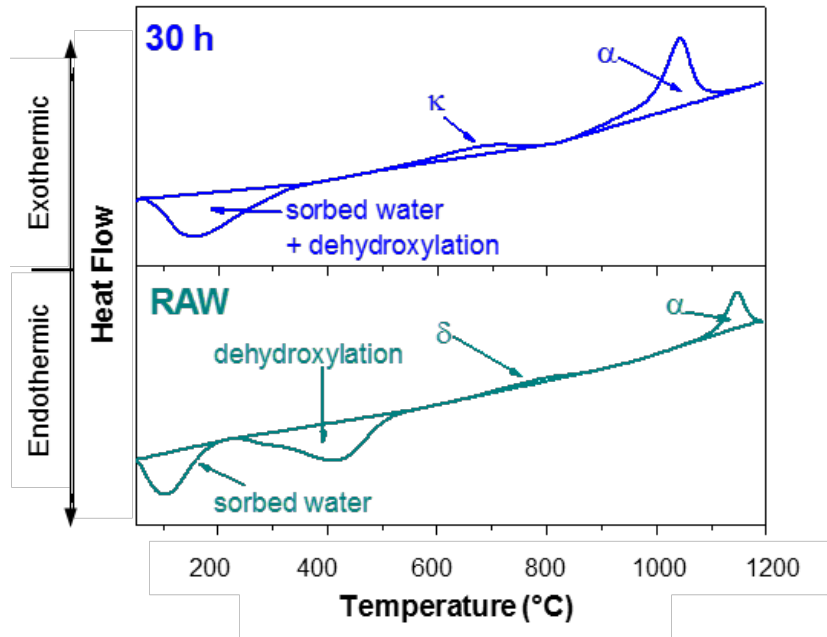


Figure 42 DSC analysis of raw and milled 30hr PB.

For the milled 30hr PB sample the phase transformation to α -Al₂O₃ initiates at around 867°C and ends at 1163°C. In the case of the raw sample the same reaction initiates at 1060°C and concludes at 1190°C. This represents a reduction in phase transformation temperature for the initial α -Al₂O₃ phase approximately 193°C, which is attributed to presence of α -Al₂O₃ “seeds” in the PB 30hr that are synthesized at room temperature by milling. The α -Al₂O₃ seeds are nano scale and serves as hetero-nuclei for the high temperature α -Al₂O₃. Another evidence for the effects of α -Al₂O₃ “seeds” is the increase in the heat released during the PB 30hr transformation to α -Al₂O₃ is 285 % larger than the PB 0hr transformation, which allowing a less demanding phase transformation process.

4.1.2 Grain Size Change

The XRD patterns of the samples at different milling times are shown in the Figure 40 (a). In order to evaluate the microstructure of the ball-milled powder, which is related to its

physical properties, the average particle sizes of PB particles was determined from the FWHM of the (120) reflection plane using the well-known Scherrer equation

$$d = \frac{0.9 \cdot \lambda}{B \cdot \cos \theta} \quad (30)$$

λ is the X-ray wavelength, θ is the angle of Bragg diffraction, B is the full width at half maximum of the XRD peak.

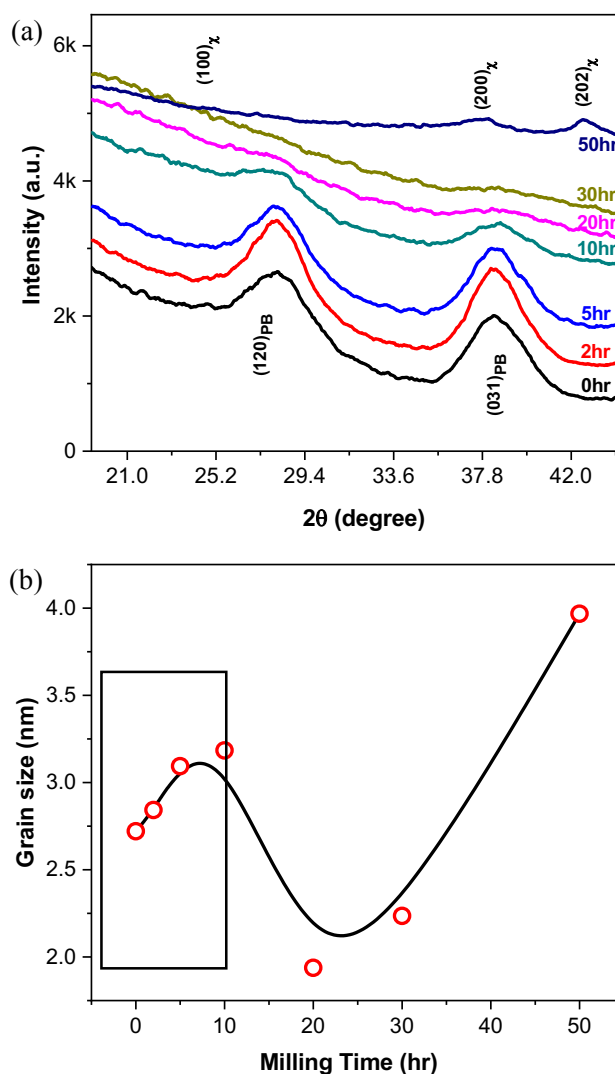


Figure 43 (a) XRD of PB at different milling time (b) variations in grain size of PB with increasing milling time (0-50hr)

The results are shown in the Figure 43 (b), the grain size values are between 2 and 4nm for the investigated samples (PB 0hr, 2hr, 5hr, 10hr, 20hr and 30hr), which is in a agreement with true atomic resolution TEM (Figure 39). And it is distinct that the average grain size increased with milling time from PB 0hr 2.72nm to PB 10hr 3.18 nm, however 20hr, 30hr and 50hr did not have same trend contributing to the phase transformation to χ -Al₂O₃. Even though the grain size calculated from Scherrer formula just provides a bulk assessment and Scherrer calculation does not account for residual stresses in the particles, the consistency of grain size got from XRD and TEM shows the validity of grain size got from XRD analysis.

The SEM (Figure 44) shows the morphology change of PB with various milling time. All milled samples have nano particle agglomerate as demonstrated by XRD and TEM [111]. The large particles are >5 μ m and smaller particles usually below 5 μ m to sub-micrometric. The subnanometric particles are most-likely debris due to the milling process.

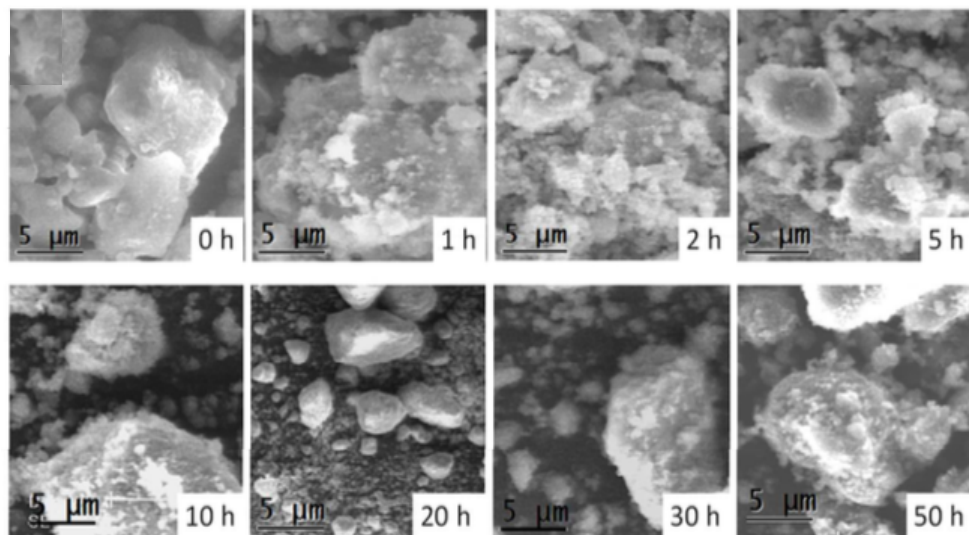


Figure 44 SEM microstructures of the raw and milled samples for up to 50hr.

4.1.3 Band Gap Change

Band gap plays a key role in determining the materials' optical property and application. Because pseudoboehmite is insulator, whose band gap equivalent to the energy exciting an electron from below the Fermi level to above it [112]. X-ray photoelectron spectroscopy (XPS) was used to measure the band gap of pseudoboehmite. Because oxygen 1s core level electron in pseudoboehmite has the largest primary photoelectron peak, O1s peak was chosen to calculate PB's band gap [113].

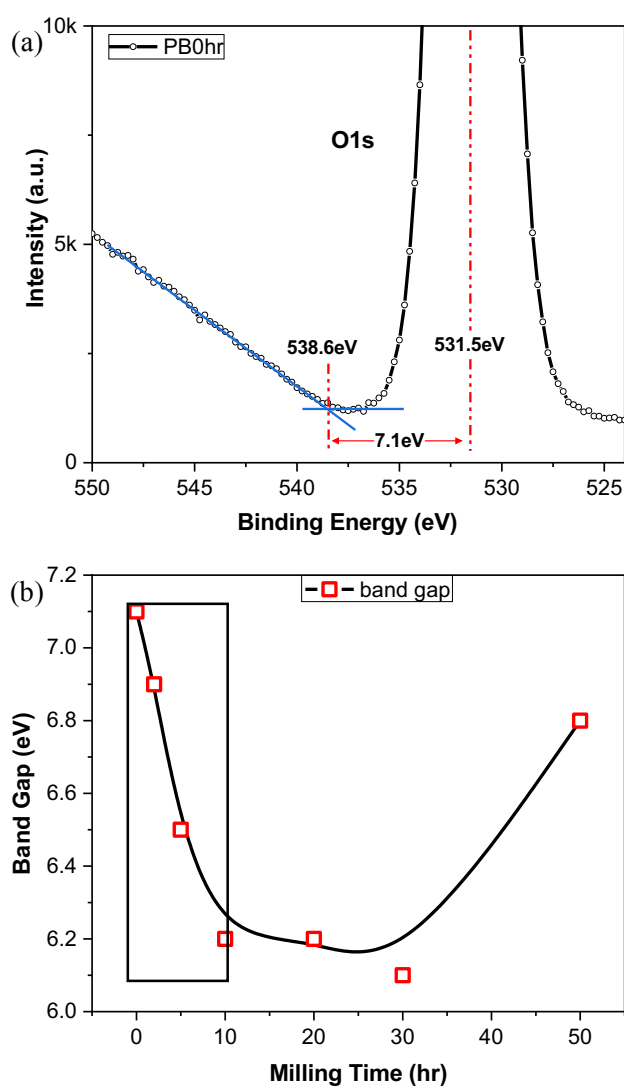


Figure 45 (a) High resolution scans of the O 1s peak the PB 0hr. (b) Band gap trend with the milling times

In Figure 45 (a) is presented an example of how the band gap is measured by means of XPS. The band gap results are given in Figure 45 (b). In order to get the band gap of PB, a linear fit is made to measure the energy difference between the core level peak and the onset of the inelastic loss (shown in the Figure 45 (a)). The results presented in Figure 45 (b) correspond to the band gaps of pseudoboehmite with different milling time.

The band gap determination by means of XPS is well known and demonstrated before [113, 114]. We used another technique that is capable of providing more discrete results. This method is EELS and is carried by the Losses of the electrons in the TEM while interacting with the sample. Figure 46 shows the measured energy loss of PB 10hr and PB 30hr with the zero loss peaks. Contrary to the XPS results, in EELS the band gap is determined by the rise-up position [115]. The EELS results show that the gap energy of 6.2eV for PB milled 10hr and 5.8eV for PB 30hr of milling. Comparing these results to the XPS ones, we conclude that both methods are in close agreement. This in general confirms the validity of our measurements.

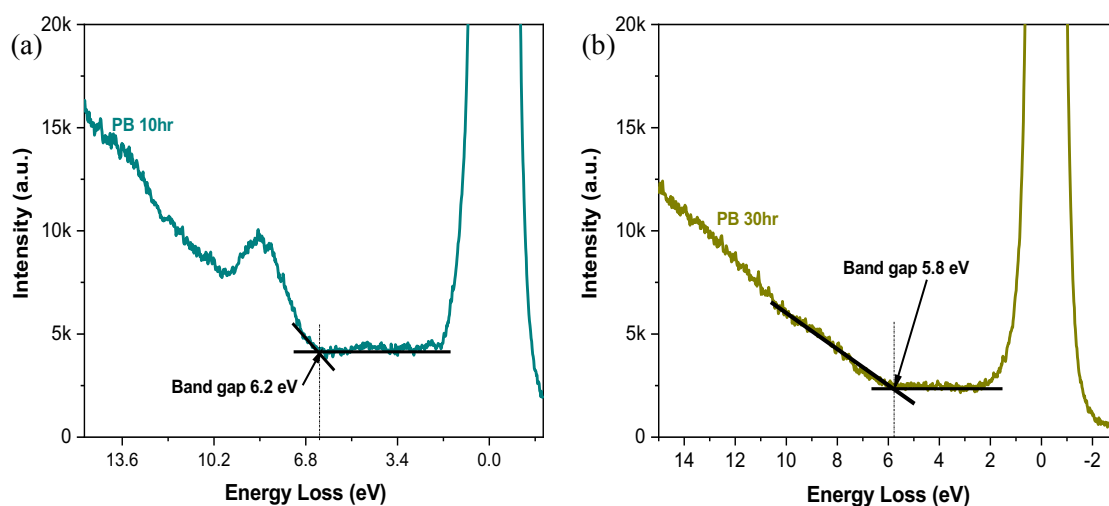


Figure 46 (a) EELS data of PB 10hr (b) EELS data of PB 30hr

4.1.3.1 Quantum Confinement

Since after 10hr mechanical milling the PB started the phase transformation process, it is hard to build the relationship between the grain size and band gap. Here we choose to narrow our analysis to PB sample between 0hr and 10hr to compare the grain size and the band gap trend, the result is shown in Figure 47 (a). It is observed that the band gap decreases with the increasing grain size, which suggests quantum confinement mechanism.

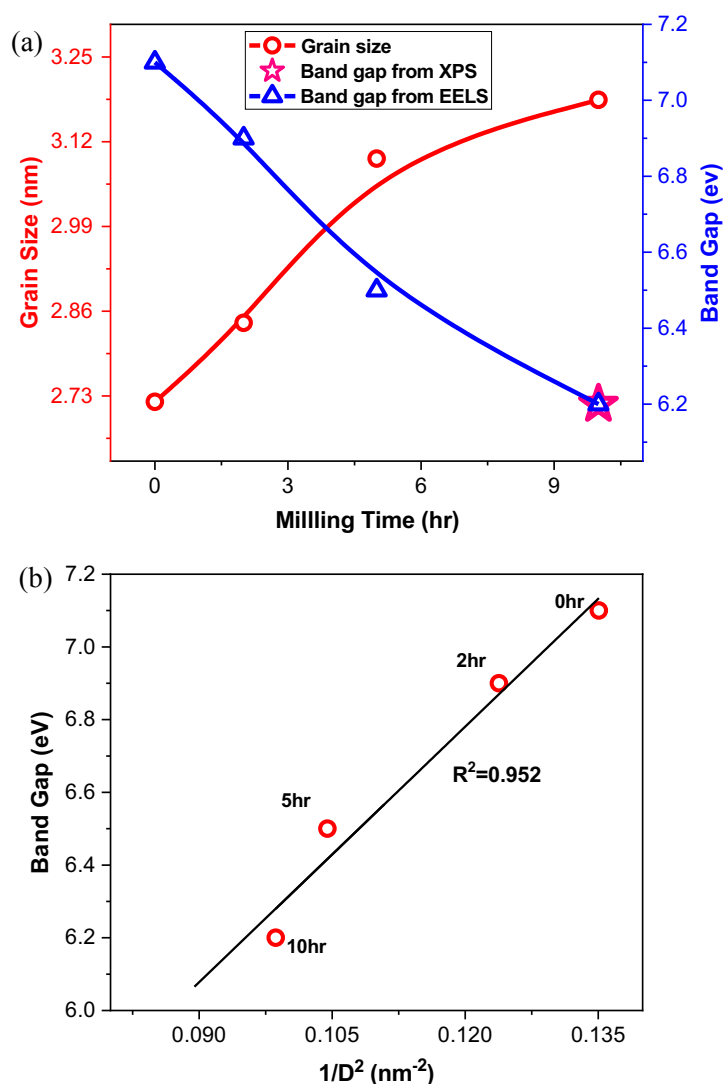


Figure 47 (a) Variation in grain size and the corresponding band gap with respect to different milling time. (b) The relationship between the band gap and $1/D^2$

So quantum confinement modeling is adopted to fit the data, then it is found that the band gap has linear relationship with the reverse of grain size square from 0 to 10hr milling (shown in the Figure 47 (b)). It means that particle size plays a key role in quantum effects of PB.

In order to confirm the increasing grain size trend during 0-10hr milling, a second batch samples were prepared. In this batch, we got one sample every one-hour of milling up to 10hr. Then XRD is used to measure the crystalline and grain size change. As the same way used for the grain size calculation of PB 0-50hr, the samples 'grain sizes were calculated by Scherrer equation (shown in Figure 48).

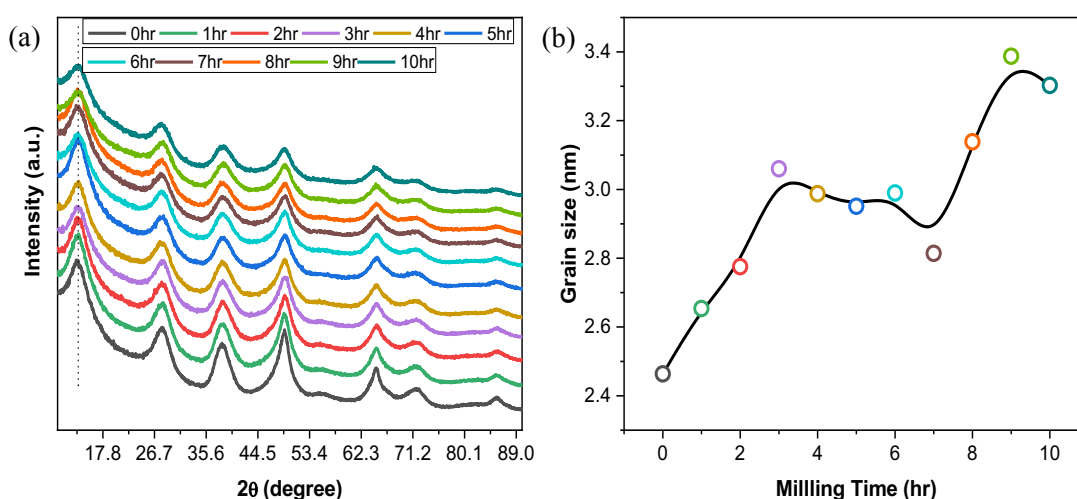


Figure 48 (a) XRD data for the samples milled 0-10hr (b) Grain size trend with the milling time

Overall the grain size increased, the increasing grain size is due to the cold welding process which is the dominating mechanism in the milled process used for up to 10hr [116]. Because pseudoboehmite is a poorly crystallized with “water layer” locates between the boehmite like layers, making pseudoboehmite mechanically soft [99]. As FTIR data (Figure 40)

mentioned during the mechanical milling process (0-10hr), the water layer is destroyed firstly, then the boehmite layers overlaps and form cold welds [117].

To further investigate the correlation between the grain size and band gap in this time range (0-10hr), second batch PB's band gap and grain size were fit in the Figure 49. For nanoparticles, if its particle size is comparable the Bohr excision radius, it shows the quantum confinement. Under this condition continue energy levels in bulk material are broken down to several separated energy states and thus increases the band gap. The resulting confined band gap can be expressed as [118, 119]

$$E_{bg}^{nanocrystal} = E_{bg}^{bulk} + \frac{A}{D^2}. \quad (31)$$

$E_{bg}^{nanocrystal}$ is the confined bang gap of a nano crystal with radius R, E_{bg}^{bulk} is the band gap of the bulk semiconductor, A is constant. After fitting Figure 46, we got $E_{bg}^{bulk} = 5.53\text{eV}$ which is consistent with the previous research ($E_{bg}^{bulk} = 5.1\text{eV}$) [114].

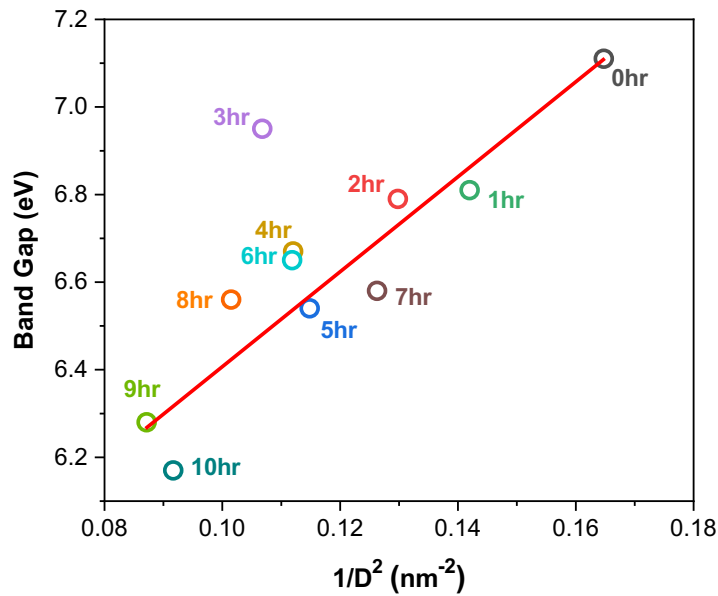


Figure 49 The relationship between the band gap and $1/D^2$

Also during 0-10hr milling process, the particle size range is between 2-4nm which is lower than the Bohr excision radius of Al_2O_3 ($R_e=20\text{nm}$) [120], the quantum size confinement should be observed.

4.1.4 Mechanical Milling Application

4.1.4.1 Preparing Sapphire Phase

Based on the study of mechanical milling effects on phase transformation, grain size and band gap change, we can find that 30hr mechanical milling can produce sapphire phase seeds in the PB sample in room temperature.

4.1.4.2 Preparing Ruby Phase

We already produce the sapphire phase by 30hr mechanical milling PB. Compared with sapphire, ruby is also $\alpha\text{-Al}_2\text{O}_3$ crystalline but partially doped with Cr^{3+} ; therefore we proposed to mechanical mill the mixture of PB and 0.2% wt Cr_2O_3 (PBCr). The XRD pattern of PBCr with various milling time is similar to the PB, there is untraceable XRD pattern of Cr_2O_3 due to the relatively low concentration of Cr_2O_3 . In order to understand if the mechanical milling is a useful method to generate Cr^{3+} (from Cr_2O_3) and substitute Al^{3+} in the host lattice of PB, Raman spectra was studied to see the luminescence change of $\alpha\text{-Cr:Al}_2\text{O}_3$ in the range of 4300 cm^{-1} to 4500 cm^{-1} .

Luminescence bands of ruby (the emitted R_1 and R_2) come from the optical emission that involves electron transitions between the states $^4\text{A}_2$ (ground state), $^4\text{T}_2$ (short lived state) and ^2E (metastable state). This can be explained by the crystal field theory, which indicates that Cr^{3+} substituting octahedral Al^{3+} can produce the maximum crystal field stabilization energy. Figure 50 shows that the intensity of the ruby phase bands increases with milling time up to 50

hours. This is associated to the increasing amount of transformed ruby. It is obvious that PB 5hr already has traceable ruby phase.

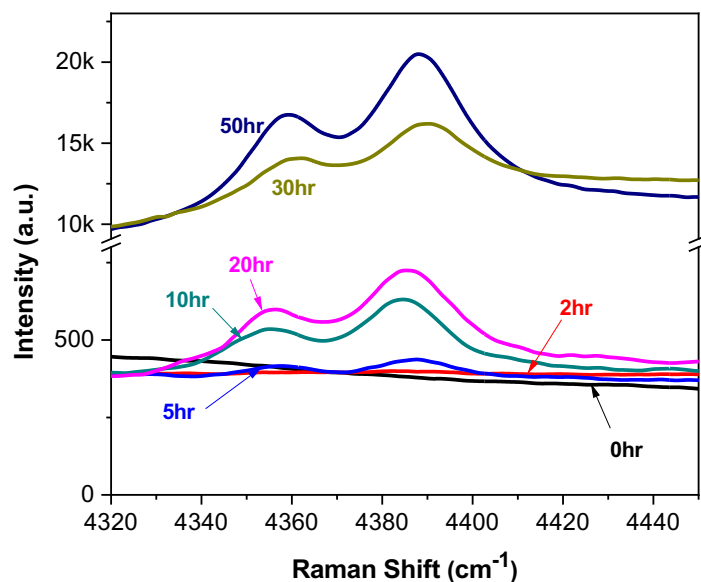


Figure 50 Raman spectra of raw and milled PBCr with an excitation line of 532 nm.

HRTEM is conducted to confirm the presence of α -Cr:Al₂O₃ in the PBCr 30hr.

Figure 51 presents a by-crystal framework of α -Cr:Al₂O₃ phases in the investigated sample.

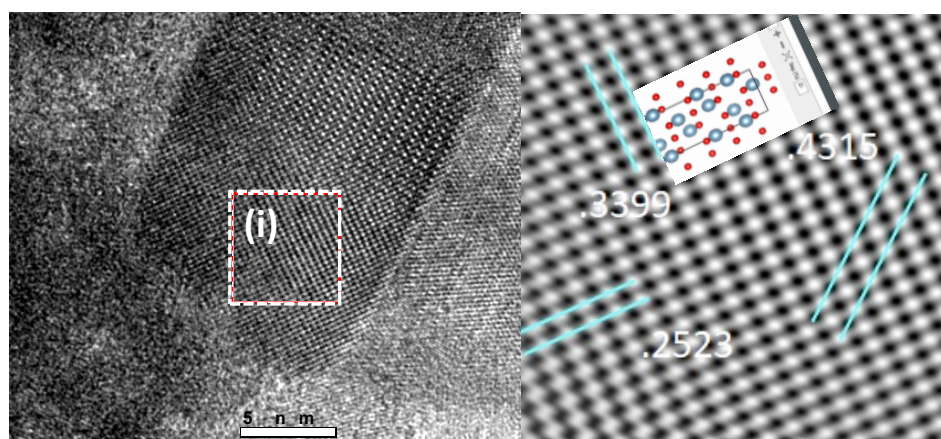


Figure 51 HRTEM images and interplanar measurements for α -Cr:Al₂O₃ showing the presence of ruby phase.

In addition, in HRTEM we did not observe pseudoboehmite, which is consistent with the XRD results. This result further confirms the successful synthesis of ruby seeds by room temperature milling. The HRTEM micrographs also shows the sample is nanostructured. The HRTEM image shows the particle that is analyzed by means of FFT to produce its respective diffraction patters. The FFT image (left one) is then converted into the IFFT (right one) to generate filtered and hence clearer images from the areas labeled (i). The analysis of area (i) matches with the characteristics of α -Cr:Al₂O₃. The inset in the IFFT image for (i) has a clear match with the simulated structure that is presented over the HRTEM image. We successfully produced ruby phase by mechanical milling the constituent of PB and Cr₂O₃ for 30hr in room temperature.

4.2 Thin Film Deposition

4.2.1 Preparation of Sapphire and Ruby Target Pellet

As discussed in section 4.1.4, we found 30hr mechanical milling PB or PBCr can produce sapphire or ruby phase in the structure. Therefore we plan to use PB 30hr or PBCr 30hr as the initial sample to continue the next step-ion beam milling. However the ion beam milling process has higher requirement for the chamber's pressure, it is necessary to transform the powder to the pellet. Then the furnace was used to transform PB 30hr pellet to α -Al₂O₃ pellet (the sapphire and ruby target). It is important to find the lowest temperature for the phase transform from PB 30hr to α -Al₂O₃. Therefore different transformation temperatures (900°C, 1000°C, 1100°C, 1200°C) were used, and then the pellets' XRD spectra were compared. As Figure 52 shows that the pellet successfully transformed to sapphire and ruby pellet after 3hr 1000°C heating. The sapphire and ruby pellets show the diffracting planes: (012), (104), (110), (113), (024), (116), (122), (214), (300) and (119) as shown in the XRD reference pattern

(X080007.9). Then the heating temperature was chosen to be 1000°C to get the sapphire or ruby pellet.

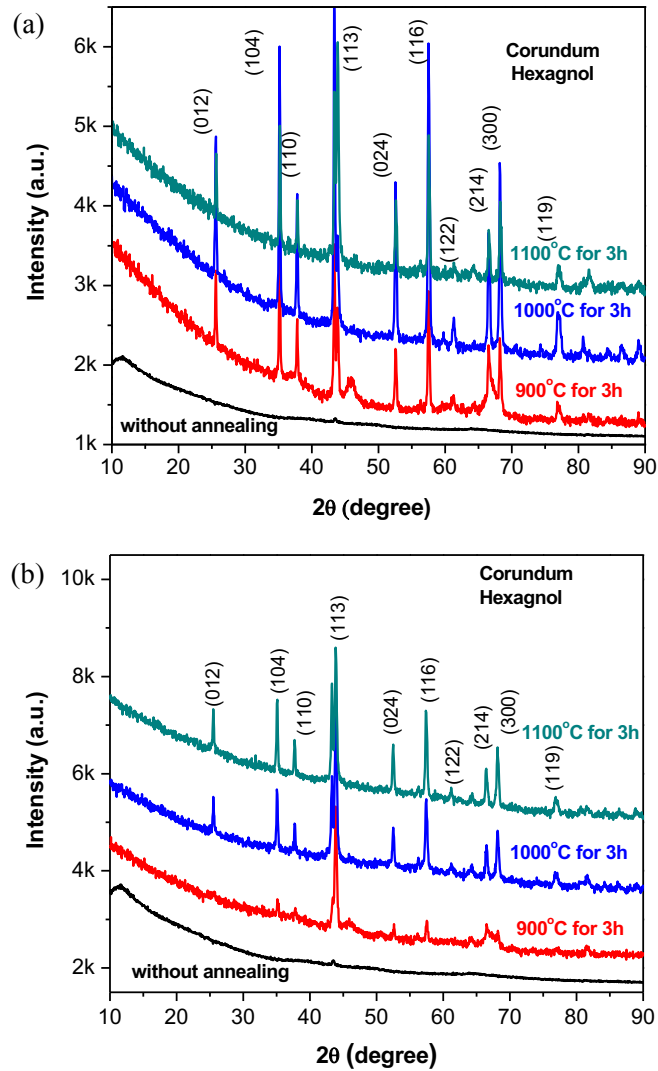


Figure 52 Diffraction patterns of the target pellet: (a) the sapphire (b) the ruby

4.2.2 Ion Beam Sputtering

In order to optimize the sputtering process, we firstly chose Ruby target to get ruby thin film. In the original chamber, ruby pellet serves as a target attached on the sample plate. Top cap made by aluminum foil to hold the substrate, then put the plate in the big chamber shown

in Figure 53 (a). We choose two different substrates: Au/Mica and silicon wafer, use 5min and 30min sputtering periods separately to show the sputtering time and substrate effects on the sputtering results.

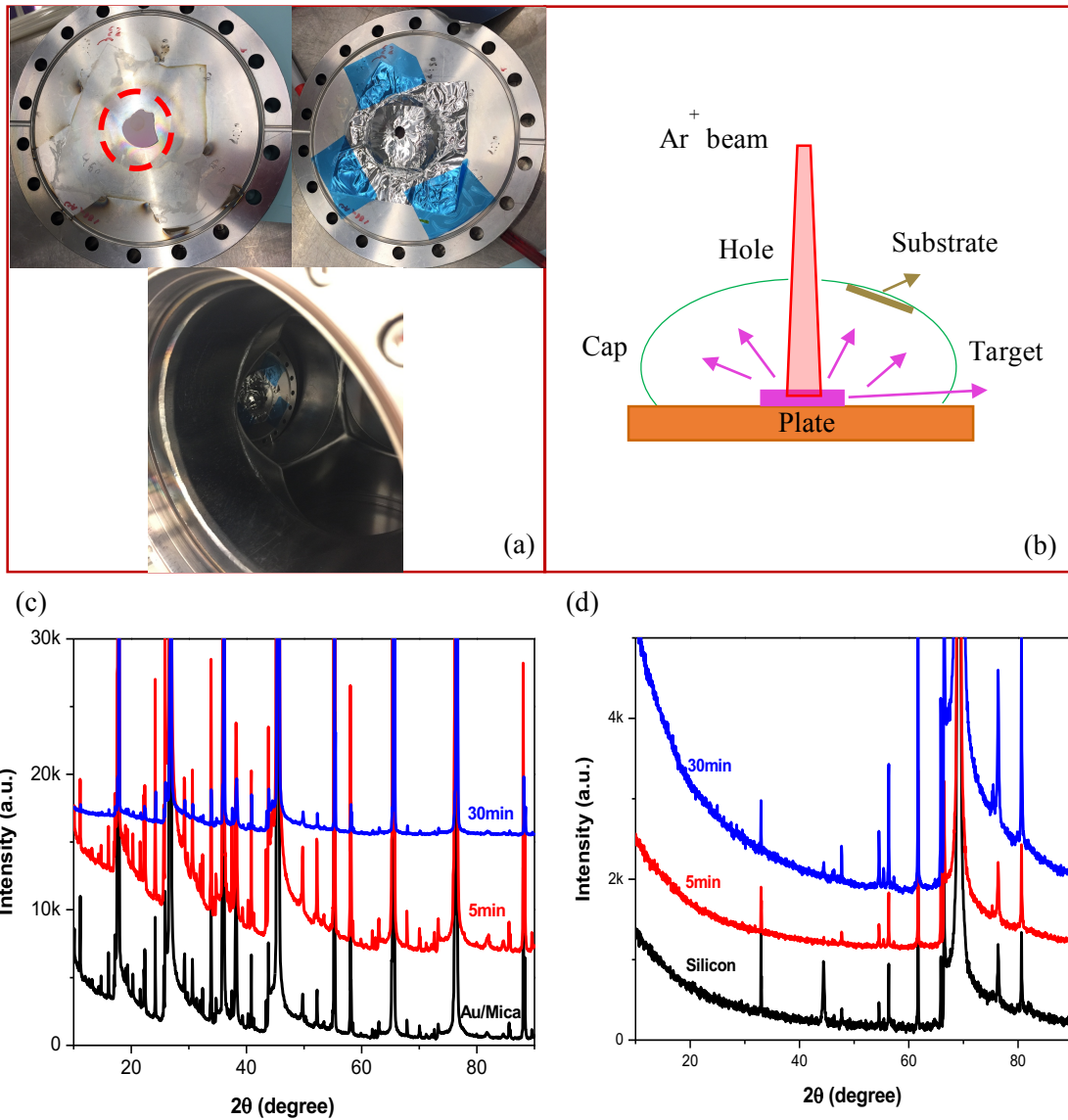


Figure 53 Original chamber: (a) photo of the chamber (b) configure of the chamber (c) sputtering ruby on Au/Mica substrate (d) sputtering ruby on Silicon wafer

The XRD spectra of the sputtered samples are displayed in Figure 53 (c) and (d). It indicates that there is no ruby deposition on both of the substrates and deposition time. The

reason can be seen from Figure 53 (b), the plasma go through the hole, which is on top of the cap. In this way, the bombarded ruby particles can be scattered in various direction that lower the sputtering efficiency.

We designed a smaller stainless steel chamber to fix the angle problem. Its photo and configure are shown in the Figure 54 (a) and (b), it is made from stainless steel and wrapped with aluminum foil. There is one hole in front of the triangle to allow the plasma go through it. And the sapphire or ruby pellet was placed in the chamber having a certain angle with the plasma beam; the substrate was on the bottom of the triangle. Then the chamber was attached on the ion-milling machine's plate. In order to test the sputtering efficiency of the new chamber, we choose Au/Mica as the substrate and fix the sputtering time to 30min. The sputtered sample's XRD and Raman spectra were shown in Figure 54 (c) and (d). As shown in Figure 54 (c) and (d), compared with the raw Au/Mica substrate the 30min sputtered sample has ruby (113) phase and ruby's Raman bands R1 and R2.

In conclusion, the sputtering chamber has optimized for Al_2O_3 in the form of ruby and sapphire with a time of 30min as ideal of the films over a wide range of substrate. The thickness is sufficient to generate the R1 and R2 bands. However, it is necessary to get sputtering rate to calculate the accurate thickness of film. So Profilometer was used to get the thickness of the thin film. The Profilometer result indicates the film thickness is 40nm after 30min sputtering process and the sputtering rate is 1.3nm/min.

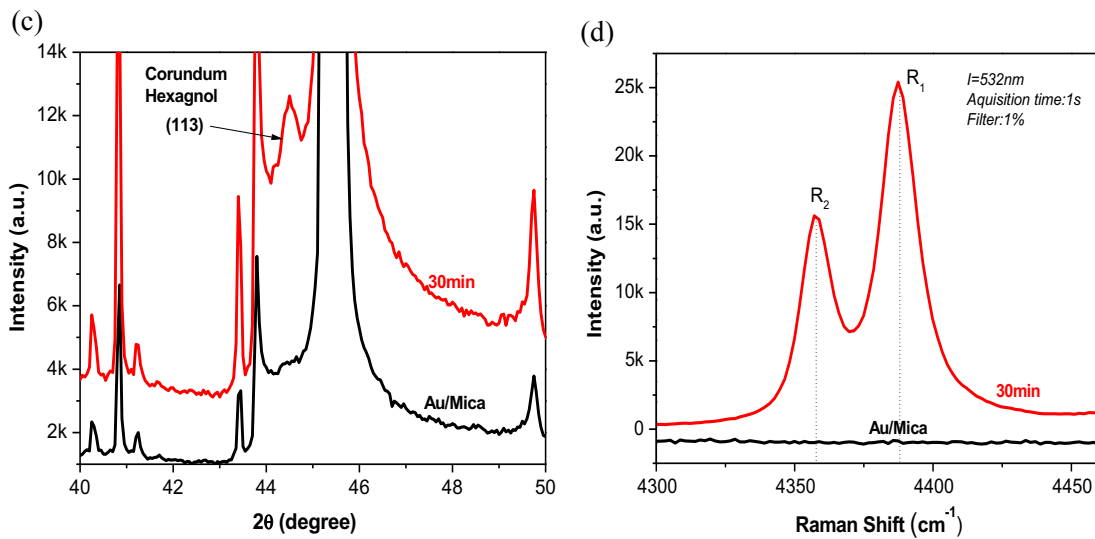
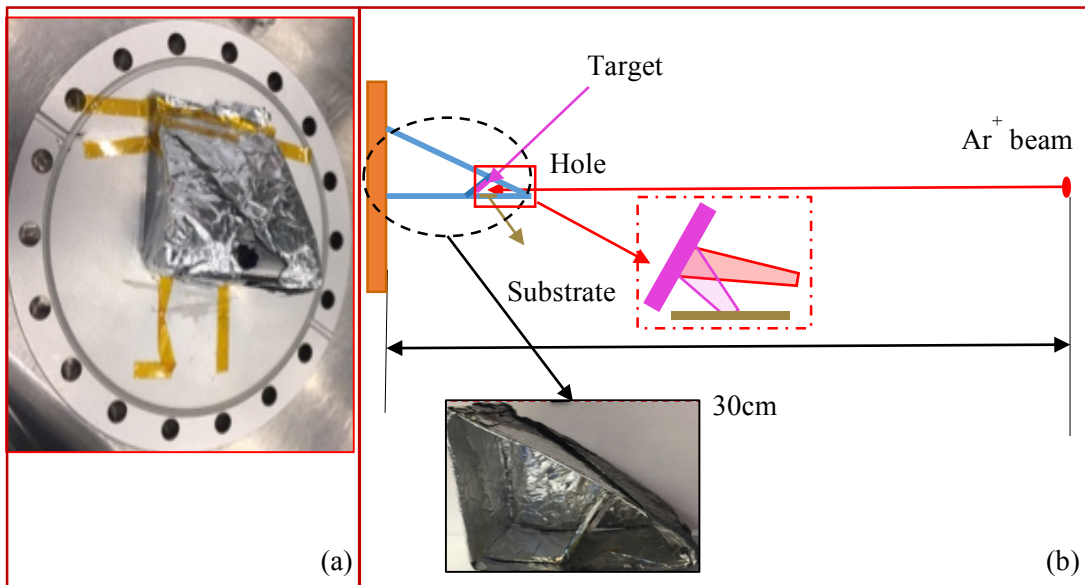


Figure 54 Designed new chamber: (a) photo of the chamber (b) configure of the chamber (c) XRD of raw and 30min sputtered Au/Mica sample (d) Raman spectra of raw and 30min sample.

4.3 Prepared Thin Films Application

4.3.1 The Sapphire Thin Film Application- High Refractive Index

Figure 55 shows sapphire phase (113) appears in the sample's structure after 120min ion beam milling of the sapphire pellet. It indicates that the sapphire thin film was successfully coated on the surface of the silicon wafer.

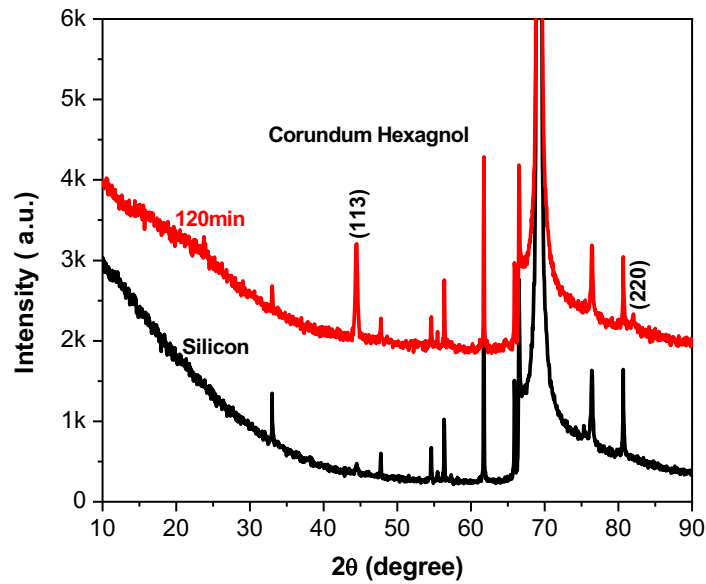


Figure 55 XRD of the 150nm sapphire thin film

The Table 2 shows the refractive index of ruby thin films from ellipsometry measurement. The result 1.73 is closer to the single crystal Sapphire's refractive index 1.76 [121, 122]. Compared with the silicon substrate refractive index 1.4, it does increase the substrate's refractive index. It is noticeable that sapphire thin film can be successfully coated on the substrate through French press, 1000°C annealing of the pellets and ion beam milling the sapphire or ruby pellet. Compared with traditional SPS sintering process, it is inexpensive and efficient to get high refractive index sapphire thin film.

Table 2 Ellipsometry results

Sample	RF
Sapphire coating spot 1	1.73
Sapphire coating spot 2	1.70
Sapphire (single crystal) [122]	1.76

4.3.2 The Ruby Thin Film Application-Pressure Sensing

The change of Ruby's Raman spectra peak is used as an indirect measurement of the superconductor thin film's stress. Firstly Ni tape was used as a substrate to coat ruby thin film on its bottom, then XRD was used to confirm if the ruby thin film appearance. Figure 56 (a) shows that after 120min ion beam sputtering process the Ni tape was successfully coated with ruby thin film and its crystalline phase is ruby (113). Then superconductor YBCO was deposited on the top of the Ni tape by MOCVD. After sputtering the YBCO, the tape is bent. The stresses attributed to the residual stress of the YBCO, therefore by measuring the ruby's Raman peak shift, we can get residual stress induced by YBCO. Before sputtering YBCO, the R_2 and R_1 bands of Ruby thin film were identified at 4360.71cm^{-1} and 4390.57cm^{-1} , respectively (shown in Figure 56 (b)). After sputtering YBCO, the YBCO's compressive stress leads to the blue shift of the Ruby's Raman spectra. For the R_1 band (higher intensity) [123] the blue shift (ΔR_1) for the sample is $= 4.83\text{cm}^{-1}$. Using equation (32) we calculated the respective compressive stresses

$$\Delta\nu = -2.46 \cdot P. \quad (32)$$

Where P is the residual stress in GPa, $\Delta\nu$ is the change of frequency in cm^{-1} , and -2.46 is the piezo-spectroscopic constant [124]. The calculated values are -2.0GPa, it means the residual compressive stress for the YBCO is 2.0GPa. It is well known that oxygen is crucial for

developing compressive stress in thin films. Excessive oxygen vacancies in the YBCO thin film lattice make the film under tensile stress [91].

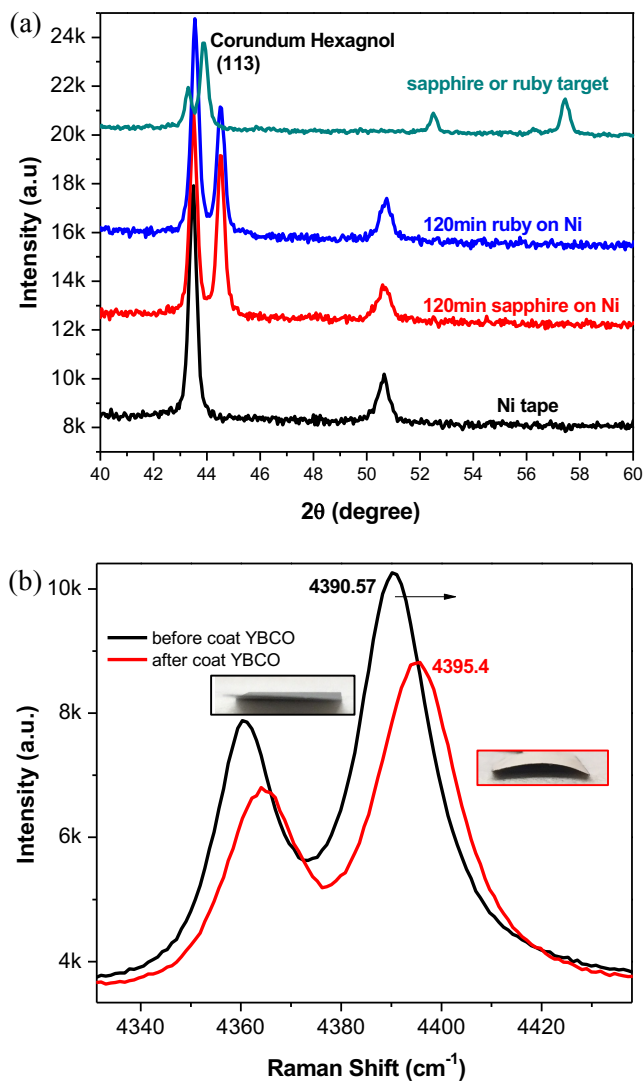


Figure 56 (a) XRD of raw Ni tape and Ni tape after 120min sputtering (b) Raman spectra of ruby thin film before and after sputtering the YBCO

CHAPTER 5

SUMMARY AND CONCLUSIONS

Mechanical milling is a high energy ball milling technique which can transfer energy to milled sample by collision between the trapped samples and the balls. PB consists of layers of AlOOH with hydrogen bond connecting the layers together. In the collision process, the trapped PB's weaker hydrogen bond were broken, hydroxyl bond diffused out from the structure and formed water. This leads to the phase transformation of PB during the mechanical milling process. FTIR data of PB 0hr to 30hr shows the stretching and bending OH vibration peak is shifting, also $[AlO_4]$ began to show up in the PB 2hr. It helped to explain the mechanism of mechanical milling effects on the phase transformation. Also the collision can change the particle size, produce defects and strain in the particle, and increase the local temperature, which restore energy in the particles. When the stored energy pass the Gibbs free energy of forming a new phase, phase transformation occurs. XRD shows PB starts to transform to χ - Al_2O_3 at times as short as 20hr of milling, also HRTEM confirms the PB 30hr already has sapphire (α - Al_2O_3) "seed" in the structure and lose the PB structure. Consequently 30hr mechanical milling reduces the transformation temperature (around 193°C) from the PB to the initial transformation temperature of sapphire, which is suggested by Thermal analysis.

During the mechanical milling process, there are two main process (fracture and cold welding) deciding the particles size change. Because of the collision some particles form cracks and break into smaller particles. While cold welding which is attributed to the plastic deformation of the particles can increase the grain size. PB is soft material with "water" layer in the structure, so cold welding is more likely to lead to the grain size change. The grain size

is calculated by XRD, the PB's grain size range is 2-4nm in diameter and has an increasing grain size trend during 0-10hr mechanical milling.

The mechanical milling effects on the band gap was studied, the band gaps of the PB 10hr and PB 30hr were measured by XPS and EELS, for these two samples band gap got from XPS consists with the one from EELS. It suggests the reliability of band gap measurement by XPS and EELS. The band gap dependence on the grain size was investigated. The linear relationship between the band gap and reverse of the grain size square indicates the application of quantum size effects on band gap. We build a scientific way to study the mechanism of quantum confinement during the mechanical milling.

By employing mechanical milling 30hr, sapphire and ruby phase can be successfully produced in room temperature. In order to synthesize high quality, flexible size and real-industrial use of the prepared sapphire and ruby, we decide to coat the sapphire and ruby thin film on the substrate by ion beam sputtering. However the ion beam sputtering chamber has requirement for the vacuum, the milled powder has to be pressed to form a pellet. Also low temperature (1000°C) was used to anneal the pellet to get more sapphire or ruby phase. The XRD and Raman spectroscopy results showed sapphire and ruby thin film was successfully deposited on the substrate by ion beam sputtering technique.

This research investigated these thin film's applications:

- 1) Application of sapphire thin film. In Ellipsometry, a model has already been built to measure the thin film's refractive index by coating it on silicon substrate. In order to measure sapphire thin film's refractive index, 150nm sapphire was coated on the silicon substrate. The result shows the refractive index of the sapphire thin film is 1.73, which is close to the single

crystal sapphire's refractive index 1.76. It implies that the synthesized sapphire film has high quality and densely packed on the substrate. This is because in the sputtering process the ion momentum were transferred to the bombarded sapphire atoms, which helps the atoms grow preferred orientation on the substrate with low void density.

2) Application of ruby thin film. In the range of 4300cm^{-1} to 4500cm^{-1} ruby luminescence bands R1 and R2 can have red or blue Raman shift due to their highly sensitivity to temperature and pressure. So in this research we proposed to use ruby thin film as a pressure sensor, to indicate the amount of pressure existing in the film. Here three layers film structure is designed, Ni tape is used as the original substrate, its bottom is coated with ruby by ion beam sputtering process, and then its top is deposited with YBCO by MOCVD. Raman spectroscopy is used to measure the R1 and R2 bands of ruby thin film before and after depositing YBCO, the Raman peak shift of R1 band (high intensity) is used to calculate the ruby's compressive stress (2.0GPa).

CHAPTER 6

FUTURE WORK

Further studies on improving the uniformity of the thin film is desirable, it requires more understanding of the mechanism involved in the sapphire or ruby thin film formation, the target consumption and the modeling of the interaction between plasma and target. In order to understand the thin film formation, thin film growth modeling should be built to show the effects from the growth parameters like diffusion, absorption, and kinetic reaction. For the sapphire or ruby target consumption, a molecular dynamic model can be applied to model the shape changes and gas absorption of the Argon gases during the deposition. The interaction between the plasma and the target can be modeled for the energy transfer from the plasma to the target while moving across its surface.

For the optical application of sapphire or ruby thin film, it can also be applied as an anti-reflection thin film in solar cell device. A photovoltaic device is a device converting the incident photons to charging carriers to produce solar energy. So it is important to capture the incident photons with less reflectance loss of light. High refractive index material like sapphire or ruby thin film can be coated on top of the photovoltaic device to improve the solar cells' efficiency by reducing the reflectance loss of light. Also sapphire and ruby thin film is scratch resistant, thus it can protect the device from scratching. Different experiments can be designed to find the optimistic method to get sapphire and ruby thin film.

As its application as a stress sensor, we just show the tensile stress of YBCO film can be characterized by the ruby's Raman peak shift. Later we can investigate the stress

measurement with various thicknesses of YBCO films. Through the residual stress comparison, we can find the optimistic thickness of YBCO.

Besides the optical and stress measurement application of sapphire or ruby thin film, it can also be applied to increase the hardness of the substrate. Different type of substrate could be used to coat sapphire or ruby thin film. Then the samples' hardness can be measured. By comparing the hardness difference between before and after deposition, we can display if the hardness is increase or not.

REFERENCES

- [1] J. Metson, Production of alumina, in: Fundamentals of Aluminium Metallurgy, *Woodhead Publishing*, 2011, pp. 23-48.
- [2] K.J.D. MacKenzie, Oxides of Aluminum Other Than Al₂O₃[alumina], *Journal of the British Ceramic Society*, 5 (1968) 363-367.
- [3] S.K. Das, W. Yin, The worldwide aluminum economy: The current state of the industry, *JOM*, 59 (2007) 57-63.
- [4] Chapter 2 Economic Importance of Bauxite Deposits, in: I. Valetton (Ed.) *Developments in Soil Science*, Elsevier, 1972, pp. 3-14.
- [5] U.S.G.S. (USGS), *Mineral Commodity Summaries*, (2009).
- [6] T. Sparks, Alumina: Filtration in the alumina production process, *Filtration & Separation*, 47 (2010) 20-23.
- [7] A.M. Donoghue, N. Frisch, D. Olney, Bauxite Mining and Alumina Refining: Process Description and Occupational Health Risks, *Journal of Occupational and Environmental Medicine*, 56 (2014) S12-S17.
- [8] S. Kumar, K. Kang, G. Bae, V. Selvarajan, C. Lee, Synthesis and characterization of alumina nano-powders by oxidation of molten aluminium in a thermal plasma reactor: Comparison with theoretical estimation, *Materials Chemistry and Physics*, 112 (2008) 436-441.
- [9] A. Boumaza, L. Favaro, J. Lédion, G. Sattonnay, J.B. Brubach, P. Berthet, A.M. Huntz, P. Roy, R. Tétot, Transition alumina phases induced by heat treatment of boehmite: An X-ray diffraction and infrared spectroscopy study, *Journal of Solid State Chemistry*, 182 (2009) 1171-1176.
- [10] Z.a.P.i. odziana, Dynamical stability of the α and θ phases of alumina, *Phys. Rev. B*, 67 (2003) 7.

- [11] J.K.M.F. Daguano, C. Santos, R.C. Souza, R.M. Balestra, K. Strecker, C.N. Elias, Properties of ZrO₂-Al₂O₃ composite as a function of isothermal holding time, *International Journal of Refractory Metals and Hard Materials*, 25 (2007) 374-379.
- [12] T. yan, X. Guo, X. Zhang, Z. Wang, J. Shi, Low temperature synthesis of nano alpha-alumina powder by two-step hydrolysis, *Materials Research Bulletin*, 73 (2016) 21-28.
- [13] G. Paglia, C.E. Buckley, A.L. Rohl, R.D. Hart, K. Winter, A.J. Studer, B.A. Hunter, J.V. Hanna, Boehmite Derived γ -Alumina System. 1. Structural Evolution with Temperature, with the Identification and Structural Determination of a New Transition Phase, γ' -Alumina, *Chemistry of Materials*, 16 (2004) 220-236.
- [14] G. Busca, The surface of transitional aluminas: A critical review, *Catalysis Today*, 226 (2014) 2-13.
- [15] S. Liu, L. Zhang, L. An, W. Fei, H. Heinrich, Phase Transformation of Mechanically Milled Nano-Sized γ -Alumina, *Journal of the American Ceramic Society*, 88 (2005) 2559-2563.
- [16] C. Chou Ting, G. Nieh Tai, Nucleation and Concurrent Anomalous Grain Growth of α -Al₂O₃ During γ - α Phase Transformation, *Journal of the American Ceramic Society*, 74 (1991) 2270-2279.
- [17] G. Toledo-Chávez, J.-C. Paniagua-Rodríguez, J. Zárate-Medina, R. Maya-Yescas, Reactions analysis during the synthesis of pseudo-boehmite as precursor of gamma-alumina, *Catalysis Today*, 271 (2016) 207-212.
- [18] P.d.S. Santos, A.C.V. Coelho, H.d.S. Santos, P.K. Kiyohara, Hydrothermal synthesis of well-crystallised boehmite crystals of various shapes, *Materials Research*, 12 (2009) 437-445.
- [19] L. Pach, R. Roy, S. Komarneni, Nucleation of alpha alumina in boehmite gel, *Journal of Materials Research*, 5 (2011) 278-285.
- [20] L.M.S. Christensen A N, Convert P, Deuteration of crystalline hydroxides, *Acta Chemica Scandinavica A* 36 (1982) 303-308.

- [21] K. Gan Bee, C. Madsen Ian, G. Hockridge James, In situ X-ray diffraction of the transformation of gibbsite to α -alumina through calcination: effect of particle size and heating rate, *Journal of Applied Crystallography*, 42 (2009) 697-705.
- [22] C.M. Karl Wefers, Oxides and Hydroxides of Aluminum Alcoa Technical Paper *Aluminium Company of America Pittsburgh, PA*, (1987).
- [23] J.M. McHale, A. Auroux, A.J. Perrotta, A. Navrotsky, Surface Energies and Thermodynamic Phase Stability in Nanocrystalline Aluminas, *Science*, 277 (1997) 788.
- [24] J.M. McHale, Auroux, A., Perrotta, A. J., & Navrotsky, A., Surface energies and thermodynamic phase stability in nanocrystalline aluminas, *Science*, 277 (1997) 788-791.
- [25] X.Z. Jiaguo Yu, Jimmy C. Yu, Guirong Zhong, Jianjun Han, Qingnan Zhao, The grain size and surface hydroxyl content of super-hydrophilic TiO₂/SiO₂ composite nanometer thin films, *journal of Materials Science Letters*, 20 (2001) 3.
- [26] B.C.a.D.B. Lippens, J. H., Study of phase transformations during calcination of aluminum hydroxides by selected area electron diffraction, *Acta Crystallographica*, 17 (1964) 1312–1321.
- [27] R. Lafficher, M. Digne, F. Salvatori, M. Boualleg, D. Colson, F. Puel, Development of new alumina precipitation routes for catalysis applications, *Journal of Crystal Growth*.
- [28] S. Lamouri, M. Hamidouche, N. Bouaouadja, H. Belhouchet, V. Garnier, G. Fantozzi, J.F. Trelkat, Control of the γ -alumina to α -alumina phase transformation for an optimized alumina densification, *Boletín de la Sociedad Española de Cerámica y Vidrio*, 56 (2017) 47-54.
- [29] W.Y.a.O. Ching, Lizhi and Rulis, Paul and Yao, Hongzhi, Ab initio study of the physical properties of γ -Al₂O₃: Lattice dynamics, bulk properties, electronic structure, bonding, optical properties, and ELNES/XANES spectra, *Phys. Rev. B*, 78 (2008) 014106.
- [30] M.A.T. Trueba, S. P., γ -Alumina as a Support for Catalysts: A Review of Fundamental Aspects, *Eur. J. Inorg. Chem.*, (2005) 3393–3403.
- [31] R. Chen, Y. Li, Y. Zhao, S. Li, R. Xiang, N. Xu, F. Liu, Effect of inorganic acid on the phase transformation of alumina, *Journal of Alloys and Compounds*, 699 (2017) 170-175.

- [32] H.-L. Wen, Y.-Y. Chen, F.-S. Yen, C.-Y. Huang, Size characterization of θ - and α -Al₂O₃ crystallites during phase transformation, *Nanostructured Materials*, 11 (1999) 89-101.
- [33] R.Y. Husson E, Structural studies of transition aluminas. Theta alumina, *Journal of Solid State and Inorganic Chemistry*, 33 (1996) 1223-1231.
- [34] T.M. French, G.A. Somorjai, Composition and surface structure of the (0001) face of .alpha.-alumina by low-energy electron diffraction, *The Journal of Physical Chemistry*, 74 (1970) 2489-2495.
- [35] U. Juncomma, S. Intarasiri, D. Bootkul, U. Tippawan, Ion beam analysis of rubies and their simulants, *Nuclear Instruments and Methods in Physics Research Section B: Beam Interactions with Materials and Atoms*, 331 (2014) 102-107.
- [36] A. Arrieta, L. Escobar-Alarcón, E. Camps, P.R. González, Thermoluminescent response of aluminium oxide thin films subject to gamma irradiation, *Radiation Effects and Defects in Solids*, 162 (2007) 745-749.
- [37] S. Rупpi, Deposition, microstructure and properties of texture-controlled CVD α -Al₂O₃ coatings, *International Journal of Refractory Metals and Hard Materials*, 23 (2005) 306-316.
- [38] P. Kathirvel, J. Chandrasekaran, D. Manoharan, S. Kumar, Deposition and characterization of alpha alumina thin films prepared by chemical bath deposition, *Optik - International Journal for Light and Electron Optics*, 126 (2015) 2177-2179.
- [39] C. Cibert, H. Hidalgo, C. Champeaux, P. Tristant, C. Tixier, J. Desmaison, A. Catherinot, Properties of aluminum oxide thin films deposited by pulsed laser deposition and plasma enhanced chemical vapor deposition, *Thin Solid Films*, 516 (2008) 1290-1296.
- [40] R.C.R. Santos, E. Longhinotti, V.N. Freire, R.B. Reimberg, E.W.S. Caetano, Elucidating the high-k insulator α -Al₂O₃ direct/indirect energy band gap type through density functional theory computations, *Chemical Physics Letters*, 637 (2015) 172-176.
- [41] X. Li, Q. Chen, L. Sang, L. Yang, Z. Liu, Z. Wang, Atomic Layer Deposition Al₂O₃ Thin Films in Magnetized Radio Frequency Plasma Source, *Physics Procedia*, 18 (2011) 100-106.

- [42] S.D. Lewis J, Flack H D, Electric field gradients and charge density in corundum alpha-Al₂O₃, *Acta Crystallographica A*, 38 (1982) 733-739.
- [43] J. Stone-Sundberg, Sapphire Series Part 1: Introduction to Sapphire and Synthetic Sapphire, *GIA*, (2013).
- [44] M.S. Akselrod, F.J. Bruni, Modern trends in crystal growth and new applications of sapphire, *Journal of Crystal Growth*, 360 (2012) 134-145.
- [45] H.S. Bal, Characterization of Sapphire: for Its Material Properties at High Temperatures, *Florida State University Libraries*, (2015).
- [46] R.A. Vlasova M., Stetsenko V., Kakazey M., Aguilar Marquez P.A., Timofeeva I., Tomila T., Arellano Juarez E.A., The layer by layer selective laser synthesis of ruby, *Science of Sintering* 42 (2010) 3-13.
- [47] R. Apetz, P.B. Bruggen Michel, Transparent Alumina: A Light-Scattering Model, *Journal of the American Ceramic Society*, 86 (2004) 480-486.
- [48] C. Wang, Z. Zhao, Transparent polycrystalline ruby ceramic by spark plasma sintering, *Materials Research Bulletin*, 45 (2010) 1127-1131.
- [49] Z. Yan-Lin, L. Shuai, Z. Xiao-Kun, X. Yong, Effects of Cr³⁺ concentration on the crystallinity and optical properties of Cr-doped Al₂O₃ powders by solid-state reaction method, *IOP Conference Series: Materials Science and Engineering*, 382 (2018) 022037.
- [50] I.J. Kim, H.S. Kim, M.Y. Seo, L.J. Gauckler, Advanced ceramics in wire bonding capillaries for semiconductor package technology, *Materials Science and Engineering: A*, 498 (2008) 129-134.
- [51] H. French Roger, H. Müllejans, J. Jones David, Optical Properties of Aluminum Oxide: Determined from Vacuum Ultraviolet and Electron Energy-Loss Spectroscopies, *Journal of the American Ceramic Society*, 81 (2005) 2549-2557.
- [52] D.D. Ragan, R. Gustavsen, D. Schiferl, Calibration of the ruby R1 and R2 fluorescence shifts as a function of temperature from 0 to 600 K, *Journal of Applied Physics*, 72 (1992) 5539-5544.

- [53] D.-p. Ma, Y. Liu, N. Ma, J. Chen, Theoretical calculations of thermal shifts and thermal broadenings of sharp lines and zero-field splitting for ruby. Part I. Thermal shifts of R1 and R2 lines, *Journal of Physics and Chemistry of Solids*, 61 (2000) 799-808.
- [54] F.D. Cortes-Vega, W. Yang, J. Zarate-Medina, S.R. Brankovic, J.M. Herrera Ramírez, F.C. Robles Hernandez, Room-temperature synthesis of χ -Al₂O₃ and ruby (α -Cr:Al₂O₃), *CrystEngComm*, 20 (2018) 3505-3511.
- [55] P. Loiko, N. Ismail, J.D.B. Bradley, M. Götelid, M. Pollnau, Refractive-index variation with rare-earth incorporation in amorphous Al₂O₃ thin films, *Journal of Non-Crystalline Solids*, 476 (2017) 95-99.
- [56] S. Kumari, A. Khare, Optical and structural characterization of pulsed laser deposited ruby thin films for temperature sensing application, *Applied Surface Science*, 265 (2013) 180-186.
- [57] A.L. Ortiz, E. Ciudad, T.N. Baymukhametov, O. Borrero-López, A.L. Vasiliev, M. Nygren, Improving the sliding wear resistance of SiC nanoceramics fabricated by spark plasma sintering via gentle post-sintering annealing, *Scripta Materialia*, 77 (2014) 9-12.
- [58] S.H. Lee, H.C. Oh, B.H. An, H.D. Kim, Ultra-low temperature synthesis of Al₄SiC₄ powder using spark plasma sintering, *Scripta Materialia*, 69 (2013) 135-138.
- [59] X. Li, G. Chen, Z. Le, X. Li, P. Nie, X. Liu, P. Xu, H.B. Wu, Z. Liu, Y. Lu, Well-dispersed phosphorus nanocrystals within carbon via high-energy mechanical milling for high performance lithium storage, *Nano Energy*, 59 (2019) 464-471.
- [60] G. Gorrasi, A. Sorrentino, Mechanical milling as a technology to produce structural and functional bio-nanocomposites, *Green Chemistry*, 17 (2015) 2610-2625.
- [61] C. Suryanarayana, Mechanical alloying and milling, *Progress in Materials Science*, 46 (2001) 1-184.
- [62] Z.S. Pereira, E.Z. da Silva, Cold Welding of Gold and Silver Nanowires: A Molecular Dynamics Study, *The Journal of Physical Chemistry C*, 115 (2011) 22870-22876.
- [63] W. Zhang, N. Bay, A Numerical Model for Cold Welding of Metals, *CIRP Annals*, 45 (1996) 215-220.

- [64] W.O. Akande, Y. Cao, N. Yao, W. Soboyejo, Adhesion and the cold welding of gold-silver thin films, *Journal of Applied Physics*, 107 (2010) 043519.
- [65] B. NN., Bay NN. Cold Pressure Welding—The Mechanisms Governing Bonding, *ASME. J. Eng. Ind.*, 101 (1979) 121-127.
- [66] W. Zhang, Bay, N, Cold Welding - Fractographic Investigation of the Weld Formation, *Welding Journal*, 76 (1997) 361-366.
- [67] C.C. Koch, THE SYNTHESIS AND STRUCTURE OF NANOCRYSTALLINE MATERIALS PRODUCED BY MECHANICAL ATTRITION: A REVIEW, *Nanostructured Materials*, 2 (1993) 109-129.
- [68] Y.O. Rosenberg, V. Metz, Y. Oren, Y. Volkman, J. Ganor, Co-precipitation of radium in high ionic strength systems: 2. Kinetic and ionic strength effects, *Geochimica et Cosmochimica Acta*, 75 (2011) 5403-5422.
- [69] P. Gill, T.T. Moghadam, B. Ranjbar, Differential Scanning Calorimetry Techniques: Applications in Biology and Nanoscience, *Journal of Biomolecular Techniques : JBT*, 21 (2010) 167-193.
- [70] A.S. Kodre KV, Yendhe PR, Patil RY, and Barge VU, Differential Scanning Calorimetry: A Review., Research and Reviews: *Journal of Pharmaceutical Analysis*, 3 (2014) 11.
- [71] A. Skallberg, C. Brommesson, K. Uvdal, Imaging XPS and photoemission electron microscopy; surface chemical mapping and blood cell visualization, *Biointerphases*, 12 (2017) 02C408.
- [72] E.B. Desimoni, Barbara, X-Ray Photoelectron Spectroscopic Characterization of Chemically Modified Electrodes Used as Chemical Sensors and Biosensors: A Review, *Chemosensors*, 3 (2015) 48.
- [73] R.F. Egerton, Electron energy-loss spectroscopy in the TEM, *Reports on Progress in Physics*, 72 (2008) 016502.

- [74] V. Teixeira, J. Carneiro, P. Carvalho, E. Silva, S. Azevedo, C. Batista, 11 - High barrier plastics using nanoscale inorganic films, in: J.-M. Lagarón (Ed.) *Multifunctional and Nanoreinforced Polymers for Food Packaging*, Woodhead Publishing, 2011, pp. 285-315.
- [75] P.M. Martin, *Handbook of Deposition Technologies for Films and Coatings*, Elsevier, (2010).
- [76] M. Kim, K.-M. Kang, Y. Wang, H.-H. Park, N-doped Al₂O₃ thin films deposited by atomic layer deposition, *Thin Solid Films*, (2018).
- [77] R. Boidin, T. Halenkovič, V. Nazabal, L. Beneš, P. Němec, Pulsed laser deposited alumina thin films, *Ceramics International*, 42 (2016) 1177-1182.
- [78] T. Ishitani, T. Yaguchi, Cross-sectional sample preparation by focused ion beam: A review of ion-sample interaction, *Microscopy Research and Technique*, 35 (1996) 320-333.
- [79] K.A. Unocic, M.J. Mills, G.S. Daehn, Effect of gallium focused ion beam milling on preparation of aluminium thin foils, *Journal of Microscopy*, 240 (2010) 227-238.
- [80] Q. Wang, S. Kishimoto, Y. Tanaka, K. Naito, Fabrication of nanoscale speckle using broad ion beam milling on polymers for deformation analysis, *Theoretical and Applied Mechanics Letters*, 6 (2016) 157-161.
- [81] H.R. Kaufman, R.S. Robinson, Broad-beam ion source technology and applications, *Vacuum*, 39 (1989) 1175-1180.
- [82] M. Oubaha, S. Elmaghrum, R. Copperwhite, B. Corcoran, C. McDonagh, A. Gorin, Optical properties of high refractive index thin films processed at low-temperature, *Optical Materials*, 34 (2012) 1366-1370.
- [83] T. Naganori, K. Isamu, N. Shinji, Refractive Index Measurement of Silicon Thin Films Using Slab Optical Waveguides, *Japanese Journal of Applied Physics*, 36 (1997) 920.
- [84] F. Koohyar, Refractive Index and Its Applications, *Journal of Thermodynamics & Catalysis*, 4 (2013).

- [85] V. Kolchinskiy, C.-H. Shih, I. Lo, R. Romashko, Refractive Index Measurement Using the Laser Profiler, *Physics Procedia*, 86 (2017) 176-180.
- [86] J.L.H. Chau, Y.-M. Lin, A.-K. Li, W.-F. Su, K.-S. Chang, S.L.-C. Hsu, T.-L. Li, Transparent high refractive index nanocomposite thin films, *Materials Letters*, 61 (2007) 2908-2910.
- [87] C. Richard, A. Renaudin, V. Aimez, P.G. Charette, An integrated hybrid interference and absorption filter for fluorescence detection in lab-on-a-chip devices, *Lab on a Chip*, 9 (2009) 1371-1376.
- [88] G.G.L. G. N. Vishnyakov, S. V. Kornysheva, G. N. Zyuzev, M. B. Lyudomirskii, P. A. Pavlov, and Yu. V. Filatov, Measuring the refractive index on a goniometer in the dynamic regime, *J. Opt. Technol*, 72 (2005) 4.
- [89] C. Guan, C.-L. Lü, Y.-F. Liu, B. Yang, Preparation and characterization of high refractive index thin films of TiO₂/epoxy resin nanocomposites, *Journal of Applied Polymer Science*, 102 (2006) 1631-1636.
- [90] J. Jung, Ellipsometry, *Aalborg University*, (2004).
- [91] J. Xiong, W. Qin, X. Cui, B. Tao, J. Tang, Y. Li, High-resolution XRD study of stress-modulated YBCO films with various thicknesses, *Journal of Crystal Growth*, 300 (2007) 364-367.
- [92] S. Li, W. Li, G. Li, W. Li, B. Zhang, P. Chou, Morphology and superconducting properties of photo-assisted MOCVD processed YBCO film by variation of sublimation temperature of the Cu-based precursor, *Physica C: Superconductivity*, 478 (2012) 60-66.
- [93] C.Y. Xu, P.X. Zhang, L. Yan, Blue shift of Raman peak from coated TiO₂ nanoparticles, *Journal of Raman Spectroscopy*, 32 (2001) 862-865.
- [94] F. Wang, I.A. Kinloch, D. Wolverson, R. Tenne, A. Zak, E. O'Connell, U. Bangert, R.J. Young, Strain-induced phonon shifts in tungsten disulfide nanoplatelets and nanotubes, *2D Materials*, 4 (2016) 015007.

- [95] L.H. Wong, C.C. Wong, J.P. Liu, D.K. Sohn, L. Chan, L.C. Hsia, H. Zang, Z.H. Ni, Z.X. Shen, Determination of Raman Phonon Strain Shift Coefficient of Strained Silicon and Strained SiGe, *Japanese Journal of Applied Physics*, 44 (2005) 7922-7924.
- [96] T. Etzelstorfer, A. Wyss, M.J. Süess, F.F. Schlich, R. Geiger, J. Frigerio, J. Stangl, Determining the directional strain shift coefficients for tensile Ge: a combined x-ray diffraction and Raman spectroscopy study, *Measurement Science and Technology*, 28 (2017) 025501.
- [97] H.M. Zhou Qingjiang, Jing Yang, Le Wang, Synthesis of Nanosized Pseudoboehmite and γ -Al₂O₃ by Control Precipitation Method, *Advanced Materials Research*, 684 (2013) 6.
- [98] W.N. Martens, R.L. Frost, J. Bartlett, J.T. Kloprogge, The ageing of alumina hydrolysates synthesized from sec-butoxyaluminium(iii), *Journal of Materials Chemistry*, 11 (2001) 1681-1686.
- [99] B.R. Baker, R.M. Pearson, Water content of pseudoboehmite: A new model for its structure, *Journal of Catalysis*, 33 (1974) 265-278.
- [100] R. Tettenhorst, D.A. Hofmann, Crystal chemistry of boehmite, *Clays and Clay Minerals*, 28 (1980) 373-380.
- [101] F.D. Cortes-Vega, W. Yang, J. Zarate-Medina, S.R. Brankovic, H.A. Calderon, F.C. Robles Hernandez, Mechanochemical synthesis of α -Al₂O₃-Cr³⁺ (Ruby) and χ -Al₂O₃, *Journal of the American Ceramic Society*, 102 (2019) 976-980.
- [102] Y. Geng, T. Ablekim, P. Mukherjee, M. Weber, K. Lynn, J.E. Shield, High-energy mechanical milling-induced crystallization in Fe₃₂Ni₅₂Zr₃B₁₃, *Journal of Non-Crystalline Solids*, 404 (2014) 140-144.
- [103] A.K. Giri, Nanocrystalline materials prepared through crystallization by ball milling, *Adv Mater*, 9 (1997) 163-166.
- [104] F.Q. Guo, K. Lu, Ball-milling-induced crystallization and ball-milling effect on thermal crystallization kinetics in an amorphous FeMoSiB alloy, *Metallurgical and Materials Transactions A*, 28 (1997) 1123-1131.

- [105] T. Kozawa, M. Naito, Mechanically induced formation of metastable χ - and κ -Al₂O₃ from boehmite, *Advanced Powder Technology*, 27 (2016) 935-939.
- [106] Growth and electrical properties of AlO_x grown by mist chemical vapor deposition, *AIP Advances*, 3 (2013) 032135.
- [107] Y.-X. Zhang, Y. Jia, Z. Jin, X.-Y. Yu, W.-H. Xu, T. Luo, B.-J. Zhu, J.-H. Liu, X.-J. Huang, Self-assembled, monodispersed, flower-like [gamma]-AlOOH hierarchical superstructures for efficient and fast removal of heavy metal ions from water, *CrystEngComm*, 14 (2012) 3005-3007.
- [108] N.A. HAGHNAZARI, Mozaffar y JAHANI, Farahnaz., The Effect of NaOH and KOH on the Characterization of Mesoporous AlOOH Nanostructures in the Hydrothermal Route., *J. Mex. Chem. Soc* 58 (2014) 95-98.
- [109] P.S. Santos, H.S. Santos, S.P. Toledo, Standard transition aluminas. Electron microscopy studies, *Materials Research*, 3 (2000) 104-114.
- [110] G.W. Brindley, The reaction series gibbsite-chi alumina-kappa alumina-corundum, *The American Mineralogist* 46 (1961) 14.
- [111] F.D. Cortes-Vega, W. Yang, J. Zarate-Medina, S.R. Brankovic, H.A. Calderon, F.C. Robles Hernandez, Mechanochemical synthesis of α -Al₂O₃-Cr³⁺ (Ruby) and χ -Al₂O₃, *Journal of the American Ceramic Society*, 0 (2018).
- [112] W.L. M. T. Nichols, D. Pei, G. A. Antonelli, Q. Lin, S. Banna, Y. Nishi, and J. L. Shohet¹, Measurement of bandgap energies in low-k organosilicates, *JOURNAL OF APPLIED PHYSICS*, 115 (2014).
- [113] M.T. Nichols, W. Li, D. Pei, G.A. Antonelli, Q. Lin, S. Banna, Y. Nishi, J.L. Shohet, Measurement of bandgap energies in low-k organosilicates, *Journal of Applied Physics*, 115 (2014) 094105.
- [114] E.O. Filatova, A.S. Konashuk, Interpretation of the Changing the Band Gap of Al₂O₃ Depending on Its Crystalline Form: Connection with Different Local Symmetries, *The Journal of Physical Chemistry C*, 119 (2015) 20755-20761.

- [115] H. Hirai, M. Terauchi, M. Tanaka, K. Kondo, Estimating band gap of amorphous diamond and nanocrystalline diamond powder by electron energy loss spectroscopy, *Diamond and Related Materials*, 8 (1999) 1703-1706.
- [116] M. Toozandehjani, Matori, A. Khamirul, Ostovan, Farhad, Abdul Aziz, Sidek, Mamat, S. Md, Effect of Milling Time on the Microstructure, Physical and Mechanical Properties of Al-Al₂O₃ Nanocomposite Synthesized by Ball Milling and Powder Metallurgy, *Materials*, 10 (2017).
- [117] M. Ramezani, Neitzert, Thomas, Mechanical milling of aluminum powder using planetary ball milling process, *Journal of Achievements in Materials and Manufacturing Engineering*, 55 (2012).
- [118] M.O.a.T.H. E. Chukwuocha, Theoretical Studies on the Effect of Confinement on Quantum Dots Using the Brus Equation, *World Journal of Condensed Matter Physics*, 2 (2012) 4.
- [119] K.K. Nanda, S.N. Sahu, One-Dimensional Quantum Confinement in Electrodeposited PbS Nanocrystalline Semiconductors, *Advanced Materials*, 13 (2001) 280-283.
- [120] K.R. Nemade, S.A. Waghuley, Low temperature synthesis of semiconducting α -Al₂O₃ quantum dots, *Ceramics International*, 40 (2014) 6109-6113.
- [121] X. Xiang, X.T. Zu, S. Zhu, C.F. Zhang, L.M. Wang, Optical absorption of metallic Zn nanoparticles in Zn ion implanted sapphire, *Nuclear Instruments and Methods in Physics Research Section B: Beam Interactions with Materials and Atoms*, 250 (2006) 192-195.
- [122] I.H.M.a.M.J. Dodge., Refractive Index and Birefringence of Synthetic Sapphire, *Journal of the Optical Society of America*, 62 (1972) 1336.
- [123] G.K. Banini, M.M. Chaudhri, T. Smith, I.P. Hayward, Measurement of residual stresses around Vickers indentations in a ruby crystal using a Raman luminescence microscope, *Journal of Physics D: Applied Physics*, 34 (2001) L122.
- [124] Q. Wen, D. R. Clarke, Ning Yu and M. Nastasi, Epitaxial regrowth of ruby on sapphire for an integrated thin film stress sensor. *Appl. Phys. Lett.* **66** (1995) 293.